Quantitative evaluation of key properties of dry and wet metal oxides and metal hydroxides as well as of their potential determining cations in aqueous solutions

Rosenholm, Jarl B.

Published in:
Advances in Colloid and Interface Science

DOI:
10.1016/j.cis.2021.102592

Published: 01/03/2022

Document Version
Final published version

Document License
CC BY

Advances in Colloid and Interface Science 301 (2022) 102592

Contents lists available at ScienceDirect

Advances in Colloid and Interface Science

journal homepage: www.elsevier.com/locate/cis

Historical Perspective

Quantitative evaluation of key properties of dry and wet metal oxides and metal hydroxides as well as of their potential determining cations in aqueous solutions

Jarl B. Rosenholm

Laboratory of Physical Chemistry, Åbo Akademi University, Aurum, Henriksgatan 2, FI-20500 Åbo (Turku), Finland

ARTICLE INFO

Keywords:
Cohesion of ionic and covalent metal oxides and metal hydroxides
Lattice, electrovalent bond, Born type electrostatic and dipolar energies
Atomization, single bond and covalent bond energies
Solubility and dissolution products
Proton association MUSIC model and cation adsorption DLVO double-layer model
Hydrolysis, hydroxyl complexation, acid protolysis and PCM model

ABSTRACT

When potential determining cations are dissolved from solids, it is a reversed process to precipitation of solids from their electrolyte solutions. In both cases there is a transport of substance and charges across the solid-liquid interface. It is obvious that a comprehensive understanding of the process involves characterization of the (dry) solid, of the solid-liquid interface and of the potential determining cation electrolyte. The aim of this review is to quantitatively evaluate the most important properties of metal oxides and metal hydroxides, of their constituent cation electrolytes and of their interactions at the solid-liquid interface. In this way the relations between commonly used key parameters frequently reported in text-books and listed in tables can be established. No external additive, other than protons/ hydroxyls (*pH*) are introduced to the system. Moreover, the most successful semi-quantitative models for solids cohesion and dissolution, for cation release from their native solids and for cation interaction with water are reviewed. In order to secure credibility 148 samples ($1 < z_M < 8$) were selected for this quantitative evaluation. The key properties are listed in 22 Tables, 8 extensive Appendices and mutually correlated in 37 Figs. For mutual comparison energies are scaled as kJ/mol.

1. Introduction

Metal oxides and metal hydroxides are perhaps the most common solids used in a range of applications. However, when discussing molecular properties of solids, much simpler model substances are used. For ionic solids, alkali halogenides are common reference substances. The reason is that they are truly ionic in character and readily soluble in water. For covalent molecules, simple hydrocarbons (methane and ethane) are selected as model compounds. This is not satisfactory, since metal oxides are characterized by both electrovalent and covalent cohesive properties and are only sparingly soluble in water. The present aim is to quantify the key cohesion properties of (dry) metal hydroxides and metal oxides. The following properties are reviewed:

- Covalent cohesion of metal (hydr)oxides is quantified by Paulings single bond energy and by Jolivets average multiple bond energy. Electronegativities receive a particular attention.
- Electrovalent cohesion is quantified by lattice energy, Kapustinskiis crystal energy, electrovalent bond energy and by Born type electrostatic and charge-dipole energies.
- Semimetals and semiconductors are quantified by electron gap and redox energies.
- Non-polar solids are characterized by van der Waals cohesion and by electron gap energy.

Most metal (hydr)oxides are precipitated from concentrated aqueous solutions. Thermodyna-mically saturated solutions are counterparts to solids. Therefore the solid-liquid exchange of constituent, potential determining cations is a part of a comprehensive understanding of metal (hydr)oxide properties. Due to cation dissolution the surface charging as a function of *pH* and of potential determining cations in water becomes an important part of this review. In order to focus on metal (hydr)oxide properties, no additives (electrolytes) other than protons and dissolved constituent cations are considered. The cation release and interaction with their parent solids are characterized by the following properties:

- Reduced van der Waals energy in the presence of water is quantified by reduced electron gap, Hamaker constant and van der Waals energies.

; DLVO =, Deyagin-Landau-Veerwey-Overbeek; MUSIC =, Multisite Complexation; PCM =, Partial Charge Model.

E-mail address: jarl.rosenholm@abo.fi.

https://doi.org/10.1016/j.cis.2021.102592
Received in revised form 17 December 2021;
Available online 28 December 2021

- Cation release to water is quantified by solubility product and solids dissolution product energies. This is the opposite process to cation precipitation to solids.
- Surface hydration and proton exchange is quantified by surface charge density and surface coverage of hydroxyl groups. Surface site densities are also quantified by Langmuir isotherms. Surface potential is related to point of zero charge (pH_{PZC}) and to acidity constants. Multisite complexation (MUSIC) model, including Parks´ and Yoon's modifications are engaged to quantify proton association energy to metal (hydr)oxide surface sites.
- Dissolution of constituent potential determining cations from metal (hydr)oxides is related to absolute and relative (contemporary) standard reduction, cation solution and cation hydration energies. Born's and Marcus´ absolute hydration, dipole, quadrupole and polarization energies provide a theoretical reference.
- Deryagin-Landau-Verwey-Overbeek (DLVO) model quantifies thermally induced diffuse cation distribution near charged surfaces in terms of surface potentials and charge densities as well as by surface coverages of hydroxyl groups. Schulze-Hardy approach is used to quantify critical interlayer distance and electrolyte concentration limits for the balance between attraction and repulsion forces (energies). The critical electrolyte concentration is related to solubility product. DLVO model based total, van der Waals attraction and repulsive interaction energies are simulated for two blocks in 1:1 electrolyte solutions.
- The particular conditions near solid-liquid interface are quantified for fluctuating hydrophobic and hydrophilic structural (solvation) forces, for potential drop due to dipole layering and for specific cation adsorption. The overall interfacial region is characterized by two (double layer) or three (triple layer) parallel condensers coupled in series. Their properties are determined by surface potentials, surface charge densities and by interlayer distance.

The interaction of cations with solid surfaces, is quantified by DLVO model where ions are considered as point charges in (water) continuum. This is an oversimplification, in particular at short distances from solid surfaces. In reality, treatment of cations as point charges is abandoned. Therefore, the multidimensional interactions by cations with water as a function of acidity (pH) is reviewed:

- Cation reactions with water are quantified by equilibrium constants (energies) for hydrolysis, hydroxyl ligand complexation and by protolysis (acidity). Aluminium (Al^{3+}) cation equilibria serve as references.
- Multisite complexation (MUSIC) model is used to relate proton association energy to cation hydrolysis. Partial charge (PCM) model is used to quantify the extent of protolysis from water coordinated to cations (aquo complexes). The limiting formation condition of hydroxyl (aquo-hydroxo) and oxide (aquo-hydroxo-oxo) complexes in acidic- to neutral solutions or of hydroxo-oxo complexes in alkaline (basic) solutions are quantified. The semi-quantitative models are evaluated against experimental aluminium olation and oxolation reactions.

In order to evaluate these models and to correlate different properties 42 metal hydroxides and 106 metal oxides are selected as model solids. The denotation of metal in metal (hydr)oxides is generalized to represent any relevant element bound to oxygen. In most cases their most important properties (atomization and/or lattice energy) had been experimentally determined [1–3]. The data is complemented by calculation procedures discussed below. The most important properties are mutually correlated in 37 Figs. In extensive 22 Tables and 8 Appendices metal (hydr)oxides are arranged according to the valence (charge number) of metals ($1 < z_M < 8$) within each of a four block periodic table suggested by Jensen [4]. Each block contain elements, which are using a minimum of successively filled and/or empty orbitals in their bonds: Elements in S-block (H and He) use only filled and/or empty *s*-orbitals in their bonds. Elements in P-block use filled and/or empty *s*- and *p*-orbitals in their bonds. Elements in D-block use filled and/or empty *s*-, *p*- and *d*-orbitals in their bonds. Elements in F-block use filled and/or empty *s*-, *p*-, *d*- and *f*-orbitals in their bonds. The organization of periodic table is illustrated in Appendix 2, where G/P symbols in upper left corner of each block represent group and periodicity, respectively.

2. Cohesion of metal oxides and metal hydroxides

Cohesion energy of solids depends on the type and structure of its bonds. Thermodynamically the energy of solids are divided into chemical and electrostatic bonds:

$$\Delta_{bo}D_m^{\theta} = \Delta_{bo}^{che}D_m^{\theta} + \Delta_{bo}^{el}D_m^{\theta} \quad (1)$$

where $D = H$, Gdenotes standard enthalpy or Gibbs(free) energy. The standard of all elements is their state at 298.15 K and 1 bar. However, standard reactions between elements and molecules occur in dilute gases (vacuum) in order to minimize secondary interaction between them. These standard states are inter-related through Hess-Born-Haber (HBH) thermodynamic cycle, which secures preservation of energy. The negative energy of formation of metal oxides represent decomposition of metal oxides to solid metal and gaseous oxygen at 298.15 K and 1 bar. The formation of gaseous metal corresponds to sublimation $\Delta_{fo}D_m{}^{\theta}(M^0,g) = \Delta_{sub}D_m(M^0,s)$ and formation of gaseous oxygen represent dissociation of oxygen gas, $\Delta_{fo}D_m{}^{\theta}(O^0,g) = \Delta_{dis}D_m(O_2,g)/2$. A significant part of metal oxide cohesion is covalent in nature. Fig. 1 illustrates the key processes characterizing cohesion of solids and hydration/solution of cations.

The key cohesion (average bond) energies ($\Delta_{bo}{}^{ave}D_m$) for metal oxides are related to atomization enthalpy ($\Delta_{bo}{}^{ave}D_m = \Delta_{ato}{}^{eq}H_m{}^{\theta} = \Delta_{ato}H_m{}^{\theta}/N_e$, N_e = number of transferred electrons) of metal oxides in dilute gaseous state of its elements. The key electrovalent (bond) energies ($\Delta_{bo}{}^{elv}D_m$) for metal oxides are related to lattice energy ($\Delta_{bo}{}^{elv}D_m = \Delta_{lat}{}^{eq}D_m = \Delta_{lat}D_m/N_e$) of gaseous ions of those elements.

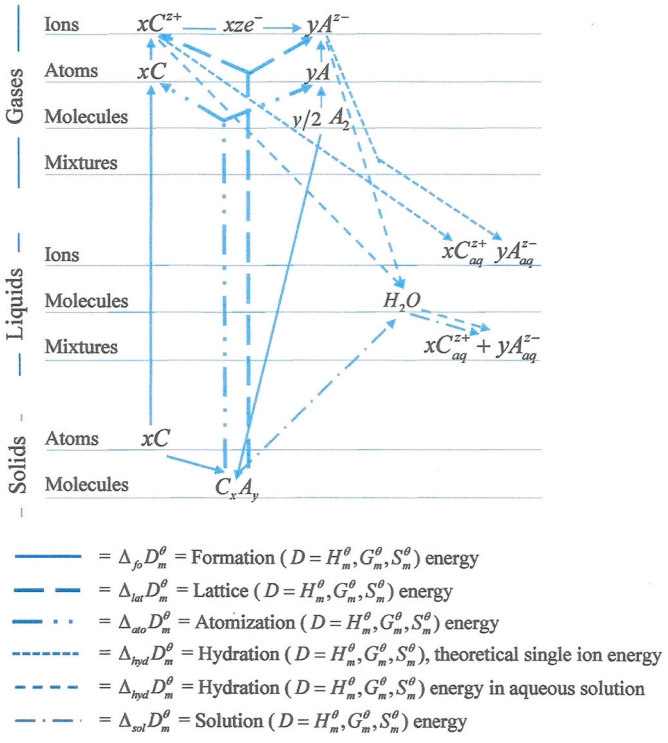

Fig. 1. Hess – Born – Haber (HBH) cycle for multiple atomic and molecular processes of cation-anion (C_xA_y) elements in solid, liquid and gas medium [5].

2.1. Covalent bond energies

Covalent bond energies can be expressed for single and multiple bonds. In this section single metal (hydr)oxide (M-O, M-OH) bond energies are compared to average multiple bond covalent energies of metal (hydr)oxides (M_xO_y, $M(OH)_z$).

2.1.1. Single bond energy – Paulings model

Molar internal bond dissociation energy (bond energy, bond strength, bond disruption energy) of isolated single bonds (diatomic molecules) is defined as the standard internal energy change during dissociation, $A-B \leftrightarrow A+B$ in gas phase. The excess energy due to dipolar interaction of *A–B* bonds may be defined arithmetically averaged [5–8] as:

$$\Delta_{bo}^{dip}D_m(A-B) = \Delta_{dis}^{gas}D_m(A-B) - \left[\Delta_{dis}^{gas}D_m(A-A) + \Delta_{dis}^{gas}D_m(B-B)\right]/2 \tag{2a}$$

or geometrically as:

$$\Delta_{bo}^{dip}D_m(A-B) = \Delta_{dis}^{gas}D_m(A-B) - \sqrt{\Delta_{dis}^{gas}D_m(A-A)\Delta_{dis}^{gas}D_m(B-B)} \tag{2b}$$

Gas phase reactions are usually characterized by spectrometry or mass spectrometry [8]. Since the conversion, measured as thermodynamic properties varies, the molar energy is denoted D_m. The bond energies (enthalpies) are expressed as eV or as kJ/mol [7–10]. The arithmeticcally or geometrically averaged symmetric single bond energy contributions (second r.h.t. in Eq. (2a) and (2b)) are considered purely covalent ($\Delta_{bo}{}^{pc}D_m(A-B)$). Polar *A–B* bonds in heteronuclear molecules are, however stronger than purely covalent symmetric bonds due to bond length differences appearing as a result of enhanced dipolar interaction [1,2]. For multiple bonds, geometric or arithmetic averaging of single bonds produce rough approximations, which should be avoided in favor of average bond energies.

Pauling suggested the use of empirical electronegativity difference $\Delta\chi^P$) of atoms such as *M* and *O* to account for dipolar interactions [5–10] as:

$$\sqrt{\Delta_{bo}^{dip}D_m(A-B)} = k_\chi\left|\chi_M^P - \chi_O^P\right| \quad \Leftrightarrow \quad \left|\chi_M^P - \chi_O^P\right| = k_\chi^{-1}\sqrt{\Delta_{bo}^{dip}D_m(A-B)} \tag{3}$$

Electronegativities are unitless, but when used to characterize dipolar interaction energy expressed as eV or kJ/mol, a constant k_χ has to be added to represent the conversion to corresponding energy scale. Since IUPAC defines unit Joule as J = CV, the conversion from electronvolt to Joule becomes: eV = $1.6021^{x}10^{-19}$ J. Multiplied by Avogadros number the constant is: $k_\chi = \sqrt{eV} = 9.8228\sqrt{kJ/mol}$ or $k_\chi^{-1} = 0.10188\sqrt{mol/kJ}$. This rather straightforward conversion has caused considerable controversy in textbooks where: $k_\chi{}^{-1} = 0.102$, dimensionless [7], $k_\chi{}^{-1} = 0.1$ 1/J [9] and $k_\chi{}^{-1} = 0.102\sqrt{mol/kJ}$ [10]. Common to all sources is that electronegativity difference relates to $\sqrt{eV}$or to $\sqrt{kJ/mol}$. Inserting Eq. (3) into Eq. (2a) and (2b) the asymmetric single bond energy can be expressed [5–10] as:

$$\Delta_{bo}^{sie}D_m(M-O) = \left[\Delta_{dis}D_m(M-M) + \Delta_{dis}D_m(O-O)\right]\Big/2 + k_\chi^2\left(\chi_M^P - \chi_O^P\right)^2 \tag{4a}$$

or as:

$$\Delta_{bo}^{sie}D_m(M-O) = \sqrt{\Delta_{dis}D_m(M-M)\,\Delta_{dis}D_m(O-O)} + k_\chi^2\left(\chi_M^P - \chi_O^P\right)^2 \tag{4b}$$

where $\Delta_{bo}{}^{sie}D_m(M-O) = \Delta_{dis}{}^{gas}D_m(M-O)$ and $k_\chi{}^2 = eV$ or $k_\chi{}^2 = 96.487kJ/mol$. The squared $\Delta\chi^P$ ensures that the polarity of the bond remains positive. A few samples of metal-metal ($\Delta_{dis}{}^{gas}D_m(M-M)$) and metal-oxygen ($\Delta_{dis}{}^{gas}D_m(M-O)$) dissociation energies [8] were selected based on their metal oxides valences ($1 < z_M < 8$, Table 1). Purely covalent single bond energies ($\Delta_{bo}{}^{pc}D_m$, Eq. (2b)), thermodynamic ($\Delta_{bo}{}^{dip}D_m$, Eq. (2b)) and Paulings ($k_\chi{}^2\ (\chi_M{}^P - \chi_O{}^P)^2$, Eq. (3)) dipolar excess energies are also listed in Table 1 for comparison.

The bond formation enthalpy can be calculated from $\Delta_{bo}{}^{sie}D_m(M-O) = \Delta_{dis}{}^{gas}D_m(M-O)$ [8] as:

$$\Delta_{fo}^{gas}H_m^\theta(M-O) = \Delta_{fo}^{gas}H_m^\theta(M^o) + \Delta_{fo}^{gas}H_m^\theta(O^o) - \Delta_{dis}^{gas}D_m(M-O) \tag{5}$$

Such bond formation enthalpies (kJ/mol) are also reported in Table 1. As shown the agreement between thermodynamic and calculated excess dipolar interaction energy is only accidental, which shows that Eq. (4a) and (4b) are only very rough approximations. Moreover, some formation enthalpy of metal-oxide bonds are negative.

The dipolar interaction can be quantified by dipole moments of *A–B* bonds as:

$$p_{M-O}^P \approx 3.33564\cdot10^{-30}\left|\chi_M^P - \chi_O^P\right| \tag{6}$$

when converted from Debye to Cm units [6,9]. The selection of samples in Table 1 is not ideal for comparison between Pauling and experimental dipole moments. Therefore, an additional selection of available samples [8] are: $p_{M-O}{}^P\cdot10^{29}/p_{M-O}{}^{exp}\cdot10^{29}$=0.41/0.55 (H-O), 0.71/2.07 (Mg-O), 0.83/2.97 (Sr-O), 0.48/1.09 (Ge-O), 0.49/1.44 (Sn-O), 0.74/1.51 (Y-O), 0.63/0.99 (Ti-O) and 0.70/0.85 (Zr-O). The agreement ranges from fair to ten times too small (Sn-O) predicted dipole moments (Eq. (6)).

Electronegativity is also a measure of ionic resonance. For fully ionic bonds the dipole moment equals the product of unit charge and equilibrium distance between heteroatoms [9], $p_{A-B}{}^{ion} = e\,l_{A-B}$ with the unit Cm. The degree of bond ionicity per cent can be estimate [9] as:

$$I_{A-B} \approx 100\left(\frac{p_{A-B}^{dip}}{p_{A-B}^{ion}}\right) \tag{7}$$

In Fig. 2 single metal-oxide bond energies ($\Delta_{bo}{}^{sie}D_m(M-O)$, kJ/mol, Eq. (4b) [8]) and covalent multiple bond energies ($\Delta_{bo}{}^{cov}D_m(M_xO_y)$ kJ/mol, Eq. (11a)) of 92 samples are plotted as a function of average bond (equivalent atomization) enthalpy ($\Delta_{bo}{}^{ave}H_m{}^\theta(M_xO_y)$ Eq. (9)).

The data shown in Fig. 2 are extracted from Appendix 1. No data on metal hydroxides are included, since their atomization energies were not available. As shown, the covalent bond energy (Eq. (11a)) remain on a nearly constant level $1000 < \Delta_{bo}{}^{cov}D_m(M_xO_y)/(kJ/mol) < 1200$, except for some mono-oxides. Single bond energies ($\Delta_{bo}{}^{sie}D_m(M-O)$, [8]) are barely linearly dependent on both covalent and average bond energy. Note that Paulings single bond energies are based on electronegativity differences, while covalent bond energies are merely an arithmetic or geometric electronegativity average (see below). The scatter is considerable and the spread increases when plotted against total atomization energy (not shown).

2.1.2. Average multiple bond energy – Jolivets model

The basic expression for average bond energy is derived from enthalpy of atomization, which is related to full decomposition of metal (hydr)oxides (Fig. 1) and it is defined as:

$$\Delta_{ato}H_m^\theta(M_xO_y) = -\Delta_{fo}H_m^\theta(M_xO_y,s) + x\,\Delta_{sub}H_m^\theta(M^0,s) + y\,\Delta_{dis}H_m^\theta(O^0,g)/2 \tag{8}$$

where $\Delta_{fo}{}^{gas}H_m{}^\theta(M^o) = \Delta_{sub}H_m{}^\theta(M^o,s)$ and $\Delta_{fo}{}^{gas}H_m{}^\theta(O^o) = \Delta_{dis}H_m{}^\theta(O_2,g)/2$. Divided by the number of exchanged electrons $x|z+| = N_e = y|z-|$ the equivalent atomization energy corresponds to average bond enthalpy of solids [3] as:

$$\Delta_{bo}^{ave}H_m^\theta(M_xO_y) = \Delta_{ato}^{eq}H_m^\theta(M_xO_y) = \Delta_{ato}H_m^\theta/N_e \tag{9}$$

Average bond enthalpies listed in Appendix 1 have been extracted from [1–3,8]. Since equivalent atomization energy represents an average of multiple M-O bond energies, Jolivet [11] suggested that the charge distribution along bonds should be considered. They developed an electronic partial charge (PCM) model [11,12] to predict the average electronegativity of a given metal (hydr)oxide complex as a sum of

Table 1
Metal-Metal (Δ_{dis}(M-M) = $\Delta_{dis}{}^{sie}D_m$(M-M)) and Metal-Oxygen ($\Delta_{bo}{}^{s}$(M-O) = $\Delta_{dis}{}^{sie}D_m$(M-O)) single bond dissociation energies [8] selected based on metal valence in metal oxides, $1 < z_M < 8$. Purely covalent bond energies (Δ_{pc}(M-O) = $\Delta_{bo}{}^{pc}D_m$(M-O), second r.h.t. in Eq. (2b)). Thermodynamic ($\Delta_{bo}{}^{d}$(M-O) = $\Delta_{bo}{}^{dip}D_m$(M-O), Eq. (2b)) and calculated $k_\chi{}^2\Delta_\chi{}^2 = 96.5(\chi_M - \chi_O)^2$, Eq. (3)) excess dipolar interaction energies. Calculated M-O bond formation enthalpies (Δ_{fo}(M-O) = $\Delta_{fo}H_m$(M-O), Eq. (5)). All energies are expressed as kJ/mol. References: $\Delta_{dis}D_m$(O-O) = 498.36 kJ/mol and $\Delta_{fo}H_m$(O-O) = 249.18 kj/mol [8]. Calculated ($p_{MO}{}^{P} = 3.33564^{x}10^{-30}\,|\chi_M - \chi_O|$, Eq. (6)) and experimental [8] dipole moments ($p_{MO}{}^{exp}$) expressed as 10^{-29} Cm.

	Δ_{dis}(M-M)	Δ_{pc}(M-O)	$\Delta_{bo}{}^{s}$(M-O)	$\Delta_{bo}{}^{d}$(M-O)	$k_\chi{}^2\Delta_\chi{}^2$	Δ_{fo}(M)	Δ_{fo}(M-O)	$p_{MO}{}^{P}$	$p_{MO}{}^{exp}$
Li-O	105	229	341	112	584	159	68.0	0.82	2.28
Cs-O	252	354	790	436	678	76.5	-464	0.88	
Ca-O	16.5	90.7	383	293	574	178	43.7	0.81	
Ba-O	NA	NA	562	NA	627	179	-134	0.85	2.65
Al-O	133	257	502	245	323	331	78.2	0.61	
Tl-O	59.4	172	213	41.0	292	182	218	0.58	
Si-O	310	124	800	675	229	450	-100	0.51	
Pb-O	86.6	208	374	166	250	195	70.4	0.54	1.55
As-O	359	423	484	61.1	153	303	67.7	0.42	
Sb-O	302	388	434	46.2	186	264	79.6	0.46	
Se-O	331	406	430	23.9	76.4	227	46.7	0.30	
V-O	269	366	637	271	316	516	128	0.60	
Nb-O	513	506	727	221	327	733	256	0.61	
Cr-O	152	275	461	186	306	397	186	0.59	1.29
Mo-O	61.6	175	502	327	158	659	406	0.43	
W-O	666	576	720	144	292	851	380	0.58	
Re-O	432	464	627	163	229	774	396	0.51	
Ru-O	193	310	528	218	148	651	372	0.41	
Os-O	415	455	575	120	148	787	461	0.41	
Ir-O	361	424	414	-10.2	148	669	504	0.41	
Au-O	226	336	223	-113	92.7	368	394	0.33	
Ce-O	252	354	790	436	519	420	-121	0.77	

electronegativities of all individual atoms in terms of Mulliken-type electronegativities of neutral metal atoms on Allred-Roshow scale (χ_M^*, Appendix 2) [4,8,11] as:

$$\chi^J = \chi^*(M_xO_y) = \frac{x\sqrt{\chi_M^*} + y\sqrt{\chi_O^*}}{x/\sqrt{\chi_M^*} + y/\sqrt{\chi_O^*}} \approx \sqrt[x+y]{(\chi_M^*)^x(\chi_O^*)^y} \quad (10a)$$

$$\chi^J = \chi^*(M(OH)_z) = \frac{\sqrt{\chi_M^*} + z\sqrt{\chi_O^*} + z\sqrt{\chi_H^*}}{1/\sqrt{\chi_M^*} + z/\sqrt{\chi_O^*} + z/\sqrt{\chi_H^*}} \quad (10b)$$

The electronegativity of metal oxides can also be calculated as geometric (or arithmetric average), but Jolivet procedure allows calculation of both metal oxides (Eq. (10a)) and metal hydroxides (Eq. (10b)). Moreover, their model allows calculation of average electronega-tivities of charged complexes (shown later) [6,11]. Allred-Rochow electronegativity is based on the interaction between electrons and nucleus. The sum of normalized atomization energy and average electronegativities (kJ/mol) is denoted covalent bond energy of metal (hydr)oxides:

$$\Delta_{bo}^{cov}D_m(M_xO_y) = \Delta_{bo}^{ave}H_m^{\theta}(M_xO_y) + k_\chi^2\chi^*(M_xO_y)^2 \quad (11a)$$

$$\Delta_{bo}^{cov}D_m(M(OH)_z) = \Delta_{bo}^{ave}H_m^{\theta}(M(OH)_z) + k_\chi^2\chi^*(M(OH)_z)^2 \quad (11b)$$

In accordance with Eq. (4) squared electronegativity corresponds to molar bond energies including factor $k_\chi{}^2 = 96.487 kJ/mol$. Covalent bond energies of nearly hundred metal oxides extracted from Appendix 1 are plotted as a function of corresponding bond energy in Fig. 2. Covalent bond energies (Eq. (11a)) of metal oxides ranging from z_M =1 to $z_M = 8$. remain on a relatively constant level $1000 < \Delta_{bo}{}^{ave}D_m{}^{\theta}(M_xO_y)/$ (kJ/mol) < 1200, except for some mono-oxides.

2.1.3. Electronegativities

Electronegativity is considered a constant which represents the isolated atom, irrespective of the combination in which it is involved. Although there are numerous definitions of electro-negativities the most common referred to, are those of Pauling and Mulliken. Electronegativity defines the negative rate at which energy of species change with a change in its electron population [4,13]. According to Mulliken the electronegativity is the arithmetic average energy required to remove an electron from a neutral atom and that released by the gain of one electron to the neutral atom [12,14]. This equals the negative chemical potential of electrons. The arithmetic average of first step ionization (oxidation) energy ($\Delta_{ion}{}^{1st}D(M^o,g) = I_e{}^{1st}$) and electron affinity (reduction) energy ($\Delta_{aff}{}^{1st}D(M^o,g) = A_e{}^{1st}$) of each metal (valence-conduction band electron exchange) has been suggested [7,8,13] as operational definition of Mulliken electronegativities (eV):

$$\chi_{ro}^M \approx \left(\Delta_{ion}^{1st}D_m(M,g) + \Delta_{aff}^{1st}D_m\left(M,g\right)\right)\Big/2 = \left(I_e^{1st} + A_e^{1st}\right)\Big/2 \approx -\mu_e \quad (12a)$$

Since electronegativity is equal to negative chemical potential of electrons, it deserves to be called absolute electronegativity. It represents the resistance of chemical potential to changes in number of electrons. It is a global property in the sense that it characterizes species as a whole. Eq. (12a) reveals confusion relating to unit of electronegativity. Both ionization and electron affinities are given as either eV [8] or kJ/mol [7], which suggests that the unit associated to Mulliken electronegativity is equally eV or kJ/mol. This contradicts previous definitions and Eq. (12a) must be redefined as:

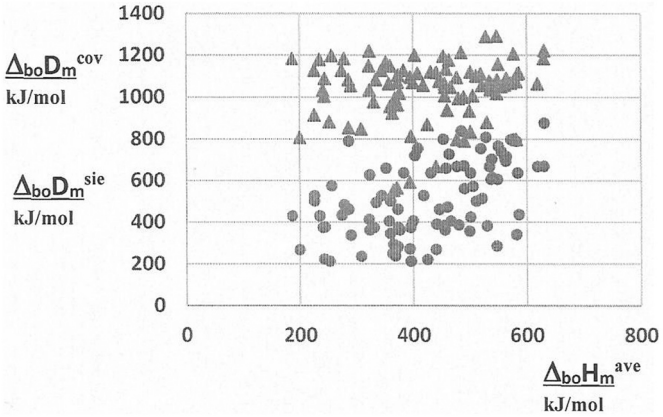

Fig. 2. Single metal-oxide bond (circles kJ/mol, [8], Eq. (4b)) and covalent bond (triangles kJ/mol, (Eq. (11a)) energies for a range of metal oxides ($1 < z_M < 8$) plotted as a function of average bond enthalpies (Eq. (9)).

$$\left(\chi_{ro}^{M}\right)^2 \approx \left(\Delta_{ion}^{1st}D_m\left(M,g\right) + \Delta_{aff}^{1st}D_m\left(M,g\right)\right)\Big/2 \quad \Leftrightarrow \quad \chi_{ro}^{1st} \approx \sqrt{\left(\Delta_{ion}^{1st}D_m + \Delta_{aff}^{1st}D_m\right)\Big/2} \tag{12b}$$

The latter expression is in agreement with Eq. (3). Instead, a scale factor (0.357) has been used to make coincident values with Pauling electronegativities [7,9]:

$$\left(\chi_{cor}^{M}\right)^2 \approx \left(\Delta_{ion}^{1st}D_m^{\theta} + \Delta_{aff}^{1st}D_m^{\theta}\right)\Big/5.6 = 0.357\left(\chi_{ro}^{M}\right)^2 \tag{13}$$

Jolivet has related Mulliken electronegativities to Paulings electronegativity [6,11] as:

$$\chi_1^M = 0.615 + 2.985\chi^P \tag{14a}$$

Obviously, both electronegativities must have coincident energy units. This linear combination between two quantities of different dimensions stems from the uncertainties in the calculation of electron affinities. The exact contribution of valence states allows a precise evaluation of the ionization potential, electron affinity and hybridization which leads [6,7,11] to:

$$\sqrt{\chi_2^M} = 1.015 + 0.741\chi^P \tag{14b}$$

In Table 2 these electronegativities are compared mutually for neutral metal atoms of oxides with increasing valences, $1 < z_M < 8$.

Paulings and Allred-Rochows electronegativities ae listed in Appendix 2. Despite sound theoretical background, the models for conversion from Paulings to Mullikens electronegativities [7,11] are not successful. As shown, only χ_{ro}^{1st} values agree with reference Mullikens electronegativities. In Appendix 3, Paulings electronegativity for single M-O bonds, Jolivets average electronegativity for metal (hydr)oxides are listed together with Paulings, Allred-Rochow, 1st redox and Mulliken type electronegativities for metals defined in Eqs. (12a), (12b), (13), (14a) and (14b).

In Fig. 3 Paulings electronegativity differences for 42 single metal–hydroxide (M-OH) and 106 metal–oxide (M-O) bonds (Eq. (3)) are plotted as a function of Jolivets average electro-negativity for metal oxides (Eq. (10a)) and metal hydroxides (Eq. (10b)). Moreover, Paulings (Appendix 2), 1st-redox (Eq. (12b)) , Mulliken-1 (Eq.14a)) and Mulliken-2 (Eq. (14b)) electronegativities for corresponding metals are plotted as a function of Allred-Rochow electronegativity (Appendix 2) in Fig. 3.

Paulings single (M-O) bond electronegativity differences decrease roughly linearly with increasing Jolivet average metal oxide electronegativity, although the scatter is quite large. The electronegativity differences of (M-OH) bonds remain localized around $\chi^* = 2.5$. Paulings electronegativity for single metals (Appendix 2) agree roughly with published Mulliken values [6,9] and with 1st redox $\chi^{1st}{}_{ro}$ (Eq. (12b)) values. They increase linearily with Allred-Rochow electronegativities ([8], Appendix 2). Mulliken-1 (Eq. (14a)) and Mulliken-2 (Eq. (14b)), which are converted from Paulings data agree mutually. Both have a fourfold slope as compared to Paulings electronegativity, which indicates that conversion models should be corrected. As suggested [13], Paulings electronegativity should be considered a minimum value and the others as average values.

Table 2
Paulings (χ^P), Allred-Rochows (χ^*), redox ($(\chi_{ro}{}^M)^2$, Eq. (12b)), first ($\chi_{ro}{}^{1st}$, Eq. (12b)), corrected($(\chi_{cor}{}^M)^2$, Eq. (13)), and Mullikens ($\chi_1{}^M$, Eq. (14a), $\chi_2{}^M$, Eq. (14b),) electronegativities of selected neutral metals based on their valence in metal oxides, $1 < z_M < 8$. Reference: Mullikens electronegativities [6,9,10,].

	χ^P	χ^*	$\chi^M{}_{ref}$	$(\chi^M{}_{ro})^2$	$\chi^{1st}{}_{ro}$	$(\chi^M{}_{cor})^2$	$\chi^M{}_1$	$\chi^M{}_2$
Li	0.98	0.97	1.28	3.01	1.73	1.07	3.54	3.03
Cs	0.79	0.87	0.79	2.18	1.48	0.78	2.97	2.56
Ca	1.00	1.04	1.30	3.07	1.75	1.10	3.60	3.08
Ba	0.89	0.89	0.89	2.68	1.64	0.96	3.27	2.80
Al	1.61	1.47	1.37	3.21	1.79	1.15	5.42	4.88
Tl	1.70	1.60	2.04	3.15	1.78	1.13	5.69	5.17
Si	1.90	1.74	2.03	4.77	2.18	1.70	6.29	5,87
Pb	1.83	1.92	2.33	3.89	1.97	1.39	6.08	5.62
As	2.18	2.20	2.26	5.30	2.30	1.89	7.12	6.92
Sb	2.05	1.98	2.06	4.83	2.20	1.72	6.73	6.42
Se	2.55	2.50	2.51	5.89	2.43	2.10	8.23	8.44
V	1.63	1.56		3.64	1.91	1.30	5.48	4.94
Nb	1.60	1.45		3.83	1.96	1.37	5.39	4.84
Cr	1.66	1.59		3.72	1.93	1.33	5.57	5.04
Mo	2.16	1.56		3.92	1.98	1.40	7.06	6.84
W	1.70	1.59		4.34	2.08	1.55	5.69	5.17
Re	1.90	1.88		3.99	2.00	1.43	6.29	5.87
Ru	2.20	1.78		4.21	2.05	1.50	7.18	7.00
Os	2.20	1.99		4.77	2.18	1.70	7.18	7.00
Ir	2.20	2.05		5.27	2.30	1.88	7.18	7.00
Au	2.46	2.02		5.77	2.40	2.06	7.96	8.05
Ce	1.12	1.17		3.25	1.80	1.16	3.96	3.40

2.1.4. Summary

The frequently quoted Paulings single bond model for estimation of excess dipolar interaction energies agrees only accidentally with experimental values. The electronegativity difference provides, however an interesting option to verify the dipole interaction contribution by comparison to experimentally determined dipole moments. Pauling model is found to underestimate dipole moments. A comparison of experimental (thermodynamic) single bond energies with single bond formation enthalpies reveals that there is considerable uncertainty in the reported values. The covalent bond energies of a large number of metal oxides seem to remain at a relatively constant level (independent of) average bond enthalpies. Paulings single (M-O) bond and Jolivetss multiple (M_xO_y) bond electronegativities are roughly linearly related, but multiple ($M(OH)_z$) bond electronegativities have a more complex relationship. There is a successful correlation between the 1st redox electronegativity with Paulings and published Mulliken electronegatvities. The suggested conversions from Paulings to Mullikens (or reverse) electronegativities are dramatically unsuccessful and must be changed.

2.2. Electrovalent bond energies

Lattice energy is defined as the energy needed to disintegrate a solid into gaseous ions (Fig.1, [1–3]):

$$\Delta_{lat}D_m\left(M_xO_y\right) = \Delta_{ato}H_m^{\theta}\left(M_xO_y\right) + \Delta_{ro}^{gas}D_m\left(xM^{z+},yO^{2-}\right) \tag{15a}$$

where lattice energy is usually set equal to lattice enthalpy ($\Delta_{lat}D_m(M_xO_y) = \Delta_{lat}H_m{}^{\theta}(M_xO_y)$). In order to make different metal oxides comparable the lattice energy must be expressed per electron transferred as electrovalent (equivalent lattice) bond energy [3] as:

$$\Delta_{bo}^{elv}D_m\left(M_xO_y\right) = \Delta_{lat}^{eq}D_m\left(M_xO_y\right) = \Delta_{lat}D_m\left(M_xO_y\right)/N_e \tag{15b}$$

Lattice and electrovalent bond energies are related to atomization energies in Fig. 4.

Atomization energy is only a fraction of lattice energy, but is of same magnitude as electrovalent bond energy. Atomization energy is, however poorly correlated to either of them. The reduction energy of $O^o(g)$ and oxidation energy of $M^o(g)$ in gas phase is measured by spectroscopy or mass spectrometry and occurs as:

$$\text{oxidation}\; xM^0 \rightarrow xM^{z+} + x|z+|e^- \quad \Leftrightarrow \quad x\,\Delta_{ion}D_m(M^o,g) = x\,I_M^{z+}$$

$$\text{reduction}\; yO^0 + y|2-|e^- \rightarrow yO^{2-} \quad \Leftrightarrow \quad y\,\Delta_{aff}D_m(O^o,g) = yA_O^{2-}$$

Note that different procedures are applied [7,8] to convert experimental data to thermodynamic quantities. For thermodynamic purposes the constant $k_\chi{}^2$ is used to convert eV to kJ/mol. Lattice and electrovalent bond energies are listed for 38 metal hydroxides and 98 metal oxides in Appendix 1.The total energy for exchange of electrons between

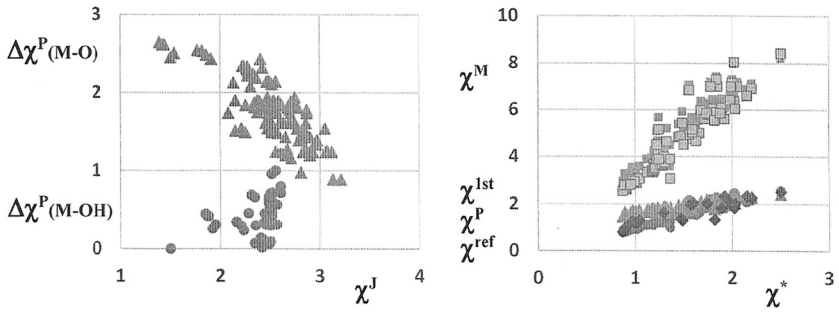

Fig. 3. Left diagram: Paulings single bond electronegativity difference (χ^P, Eq. (3)) of metal hydroxides (circles) and metal oxides (triangles) plotted as a function of Jolivets average electronegativity for metal oxides (χ^J, Eq. (10a)) and metal hydroxides (χ^J, Eq. (10b))). Right diagram, single metals: Paulings (circles, App.2), 1st-redox (χ_{ro}^{1st}, triangles, Eq. (12b)), Mulliken-1 (χ_1^M, filled squares, Eq. (14a)), Mulliken-2 (χ_2^M, squares with borders, Eq. (14b)) and reference (diamonds, Appendix 3) electronegativities plotted as a function of Allred-Rochow (χ^*, Appendix 2) electronegativies.

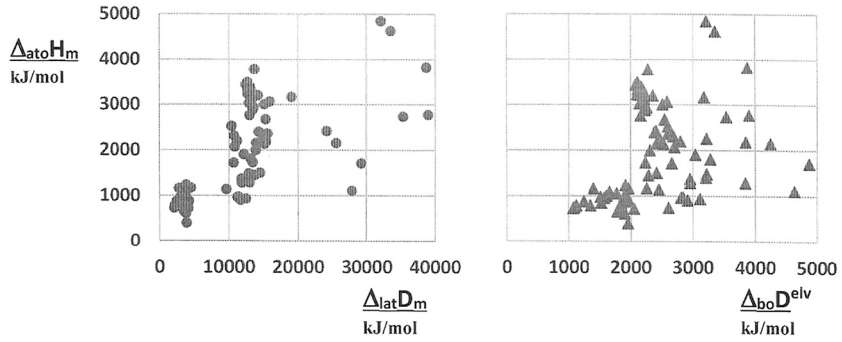

Fig. 4. Atomization energies plotted as a function of lattice (circles, left diagram) and of electrovalent bond (triangles, right diagram).

neutral gaseous elements is thus:

$$\Delta_{ro}^{gas} D_m\left(xM^{z+}, g, yO^{2-}\right) = x\,\Delta_{ion} D_m(M^o, g) - y\,\Delta_{aff} D_m(O^o, g) \tag{16}$$

Electroneutrality requires that $x|z+|e = N_e = y|2-|e$. The energy of oxidation (ionization, I_e^{z+}) and reduction (electron affinity, A_e^{z-}) are found in tables [8] for a range of electron transfers. Fig. 1 illustrated relationships between different processes between solid, liquid and gaseous states.

Ion interactions may be related to ion potential (z_M/r_M), ion (Coulomb) energy (z^2/r_M) and ion charge density (z_M/r^2). The present aim is therefore to find alternative expressions for electrovalent bond energy. Redox gas phase energy may be extracted from lattice energy and atomization enthalpy as:

$$\Delta_{ro}^{gas} D_m\left(xM^{z+}, yO^{2-}\right) = \Delta_{lat} D_m\left(M_xO_y\right) - \Delta_{ato} H_m^{\theta}\left(M_xO_y\right) \tag{17a}$$

In order to make different metal oxides comparable the redox gas phase energy must be expressed per electron transferred (equivalency, Eq. (15b)) as:

$$\Delta_{ro}^{eq} D_m\left(xM^{z+}, yO^{2-}\right) = \Delta_{ro}^{gas} D_m\left(M_xO_y\right)/N_e \tag{17b}$$

When solid cohesion is dominated by electrostatic interactions lattice (Eq. (15a)), electrovalent (Eq. (15b)) and (equivalent) redox (Eq. (17a),(17b)) energies (Eq. (15b)) may be used to characterize solid properties, since the contribution from atomization (Eq. (8)), average bond (Eq. (9)) and covalent (Eq. (11a),(11b)) energies are one decade smaller, but significant. Three models will be considered to evaluate electrovalent bond energies: Kapustinskiis model for crystal energy, Borns model for metal oxide formation in solids and charge-dipole model for metal hydroxides.

2.2.1. Crystal energy – Kapustinskiis model

When calculating lattice energies it is common to adopt Borns charging equation and adjust it for different model crystal structures utilizing Madelung constants for each structure. In practice, the exact crystal structure is usually unknown, which leads to laborious model calculations [15,16]. Taking the difference between Madelung expression and electrostatic repulsion term, Kapustinskii derived the internal crystal energy as:

$$\Delta_{Kap} D_m = \left(\frac{N_A e^2 k_M}{(4\pi\varepsilon_o)2}\right) \frac{\nu z_M z_{O(H)}}{r_M + r_{O(H)}} \left(1 - \frac{0.345}{r_M + r_{O(H)}}\right) \tag{18a}$$

where constant, $k_M = K_M/(\nu/2)$ may be related to Madelung constant K_M and ν to number of ions in metal oxide ($\nu = x + y$, M_xO_y) molecules. Since lattice energy represents disintegration of solids it is positive. Madelung constant is proportional to the number of ions ($\nu = x + y$) in metal oxides (M_xO_y), while k_M is independent of it. In Kapustinskiis model every crystal was assumed to possess NaCl structure and then k_M= 1.747565. All ions expressed in Ångstöm (10^{-10} m) relate to coordination number, $N_C = 6$ (r_O = 1.40Å, r_{OH} = 1.37Å). With these constarints Kapustinskiis equation becomes [15,16]:

$$\Delta_{Kap} D_m = 1214\,\frac{\nu z_M z_{O(H)}}{r_M + r_{O(H)}} \left(1 - \frac{0.345}{r_M + r_{O(H)}}\right) \tag{18b}$$

where crystal energy is given as kJ/mol. In Fig. 5 and Appendix 1 the crystal energies for each metal (hydr)oxide for metal oxides ranging from z_M =1 to $z_M = 8$ are compared to experimental lattice energy.

Kapustinskiis model is self-evidently an approximation, but it produces crystal energies which are almost equivalent to experimental lattice and redox energies. Obviously, metal (hydr)oxide cohesion is primarily dependent on lattice charging.

2.2.2. Solid formation energy – Borns model

Born charging equation may be used to determine the energy change when ions are transferred from dilute vapor to a solid matrix as:

$$\Delta_{Born}^{el} D_m = \left(\frac{N_A e^2}{(4\pi\varepsilon_o)2}\right) \frac{z_M z_O}{r_M + r_O} \left(1 - \frac{1}{\varepsilon_{M_xO_y}}\right) \tag{19a}$$

$$\Delta_{Born}^{el} D_m = 694.65\,\frac{z_M z_O}{r_M + r_O} \left(1 - \frac{1}{\varepsilon_{M_xO_y}}\right) \tag{19b}$$

Unfortunately, relative permittivities (dielectric constants) are

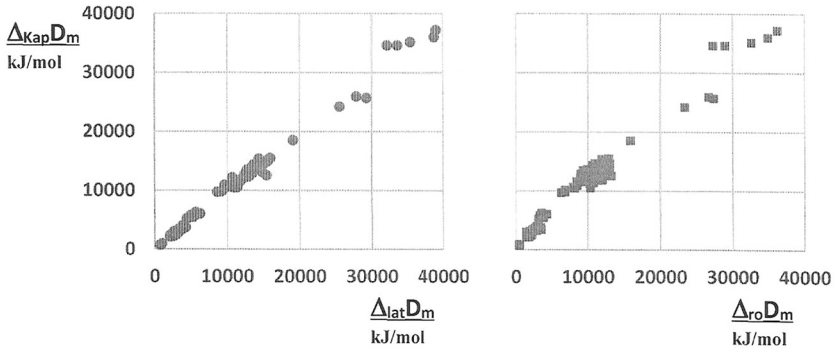

Fig. 5. Kapustinskii crystal energies (kJ/mol, Eq. (18b)) plotted as a function of lattice energies (kJ/mol, spheres, left diagram, Eq. (15a)) and redox energies (kJ/mol, squares, right diagram, Eq. (17a)) for metal (hydr)oxides ranging from $z_M = 1$ to $z_M = 8$ (Appendix 1).

available [8] only for a few metal oxides. Borns model does not correlate linearly to lattice or redox energies. However, as shown in Fig. 6, Borns "solid formation energy" is linearly dependent on electrovalent bond (equivalent lattice) (Eq. (15b)) and on equivalent redox (Eq. (17b)) energies. These energy expressions are, indeed of nearly same magnitude but displaced (different intercept and slope).

Since chemical contribution is neglected, deviations may be due to the omission of energy for cavity formation in the solid and of possible rearrangements due to ion transfer. Born`s equation needs obviously a modification, which is available from a linear fit to experimental points. Accurate relative permittivity values for a range of metal oxides is, however needed in order to investigate this relationship further.

2.2.3. Charge-dipole interaction energy

Cohesion of metal hydroxides may be related to ion-dipole interactions, which can be evaluated from the following modified Born type equation:

$$\Delta^{el}_{dip} D_m = \left(\frac{6 N_A e p_{OH}}{(4\pi\varepsilon_o)}\right) \frac{z_M}{(r_M + r_{OH})^2} \tag{20a}$$

$$\Delta^{el}_{dip} D_m = 2525 \frac{z_M}{(r_M + r_{OH})^2} \tag{20b}$$

where a general coordination number 6 has been assumed. The charge-dipole interaction did not correlate linearly to lattice or redox energies. However, as shown in Fig. 7 the charge-dipole energy is almost linearly dependent on electrovalent bond (equivalent lattice, Eq. (15b)) and equivalent redox (Eq. (17b)) energies.

There is a slight curvature from linearity. The electrostatic (Fig.6) and dipolar energy expressions are mutually of nearly same magnitude but displaced (different intercept and slope). The charge-dipole equation needs obviously a modification, which is available from a linear fit to experimental points.

2.2.4. Summary

Fig. 8 is extracted from Fig. 1 and relates formation, atomization, redox and lattice energy processes to each other.

Gas phase reactions are quantified by spectroscopy and mass spectrometry. Different procedures are used to to convert experimental data to thermodynamic quantities. Therefore the exchange of ΔD_m data to ΔH_m or ΔG_m data is not self-evident. Lattice energies exceed atomization energies and electrovalent bond energies exceed covalent bond energies for metal oxides by roughly one decade. Lattice and electrovalent bond energies are therefore frequently used alone to characterize ionic solids. The exceedingly simple Kapustinskiis model for crystal lattice energies is surprisingly successful in predicting lattice energies for metal for over hundred metal (hydr)oxides with $1 < z_M < 8$. Born type charging energies of metal oxides and charge-dipole interaction of metal hydroxides are of nearly same magnitude, linearly dependent on, but displaced from (different intercept and slope) electrovalent bond (equivalent lattice) and equivalent redox energies. Born type charging and dipole interaction energies clearly contribute to the overall lattice energy of ionic solids.

It may be argued that free energy quantities should be used instead of enthalpy. The uncertainty in conversion of gas phase data to thermodynamic quantities (enthalpy and Gibbs free energy) of condensed phases must be taken into account. For free energy of formation, entropy is however a small and almost constant fraction. Expressed per number of metal cations, the Gibbs (free) energy and enthalpy of metal (hydr) oxide formation are related as:

$$\Delta_{fo} G^{\theta}_m(M_x O_y)/x = 4,9 + 0.976\, \Delta_{fo} H^{\theta}_m(M_x O_y)/x \tag{21}$$

Due to the small difference and since gas reaction energies are undefined symbols may be generalized as D_m ($D = G, H$). Since enthalpy of formation data is much more extensive and reliable it is traditionally used in compilations of solid properties. When more data becomes

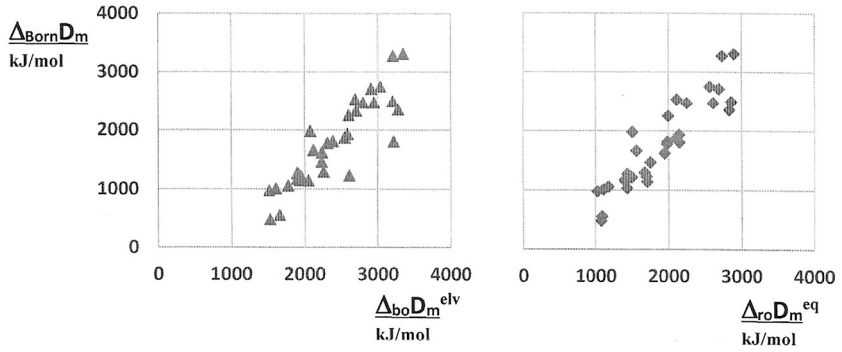

Fig. 6. Borns "solid formation energy" (Eq. (19b)) for a range of metal oxides ranging from $z_M = 1$ to $z_M = 4$ plotted as a function of electrovalent bond (equivalent lattice) energy (triangles, left diagram, Eq. (15b)) and of equivalent redox energy (diamonds, right diagram, Eq. (17b)). Data from Appendix 1.

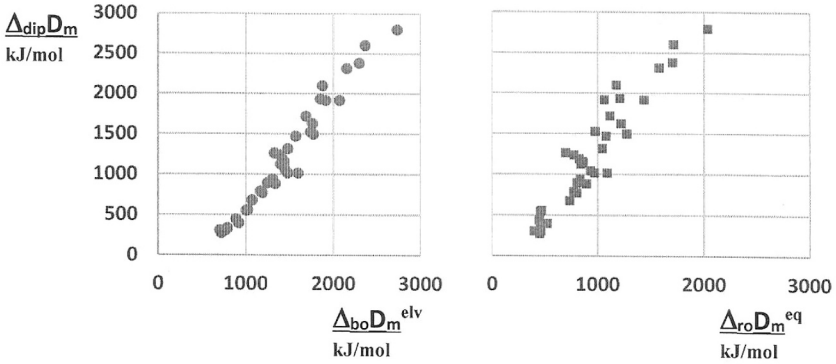

Fig. 7. Born type charge-dipole interaction energy Eq. (20b)) for a range of metal hydroxides ranging from $z_M = 1$ to $z_M = 4$ plotted as a function of electrovalent bond (equivalent lattice) energy (spheres, left diagram, Eq. (15b)) and of equivalent redox energy (squares, right diagram, Eq. (17b)).

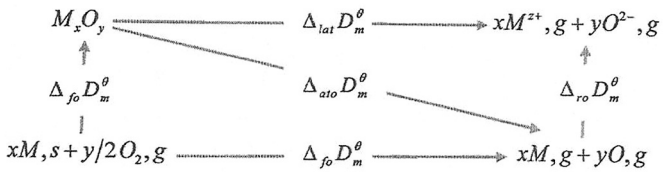

Fig. 8. Hess – Born – Haber (HBH) thermodynamic cycle for metal oxides, including formation atomization, redox and lattice energy processes [6].

available, the use of free energies are, of course recommended.

2.3. Semimetals and semicounductors – electron gap energy

One of the most important properties of materials is their electrical conductivity. For semimetals and semiconductors a small electron gap enables thermal and photon induced electron transport from valence band to conduction band. According to densityfunctional theory half of average electron gap is denoted absolute hardness [4,5,13] and it corresponds to Fermi energy level. It defines half the negative rate at which the electronegativity changes with a change in its electron population at constant potential due to the nuclei. The intrinsic electronic conductivity (κ_e) has been correlated to the electron gap [3,5] as:

$$\kappa_e = \kappa_o e^{-E_g/2kT} \tag{22}$$

where κ_e denotes limiting electron conductivity. It is found that $\ln\kappa_e$ is linearly dependent of $1/T$ for a range of metal oxides. Electron gap thence represents an Arrhenius type activation energy of this electron transport. Bulk metals with zero or low E_g signifies "softness". Metals have been classified as electronically amphoteric materials, which at contact become "soft" acids and "soft" bases [4,13]. Metals, semimetals and semiconductors are rather "soft" ($E_g^{ave} \approx E_g^o < 3$ eV or 580 kJ/mol). For intrinsic semiconductors, the electron band gap is twice the electrochemical potential of electrons and thereby twice Fermi energy of semiconducting metal oxides. Electron gap energy can be related to photonic energy of these oxides. In the following electron gap energy (kJ/mol) will be related to different solid state properties.

2.3.1. Thermodynamic considerations

It has been suggested that E_g (kJ/mol) of several inorganic substances is roughly between one-to-two times enthalpy of formation per mol [17]. For improved correlation the enthalpy of formation should be divided by the number of transferred ions [3,5] as:

$$E_g = -k_E\left(\frac{\Delta_{fo}H_m^\theta}{N_e}\right) = -k_E\Delta_{fo}^{eq}H_m^\theta \tag{23}$$

where $k_E \approx 2$ and $x|z+| = N_e = y|z-|$. In Fig. 9 average of published electron gap energies (Table 3) are plotted against standard equivalent molar enthalpy and standard molar equivalent molar Gibbs free energy of formation [8].

A fit was made to experimental points and they were averaged using:

$$E_g^o = -2.1\Delta_{fo}^{eq}H_m^\theta \tag{24a}$$

$$E_g^o = -2.4\Delta_{fo}^{eq}G_m^\theta \tag{24b}$$

Due to spread of experimental E_g points the fit is only reasonable. For a variety of solids it has been observed that the average bond (equivalent atomization) enthalpies (Appendix 1, Eq. (9) [1–3]) are related to electron gap enthalpies as:

$$E_g^o = -521 + 2\left(\frac{\Delta_{ato}H_m^\theta}{N_e}\right) = -521 + 2\Delta_{bo}^{ave}H_m^\theta \tag{25}$$

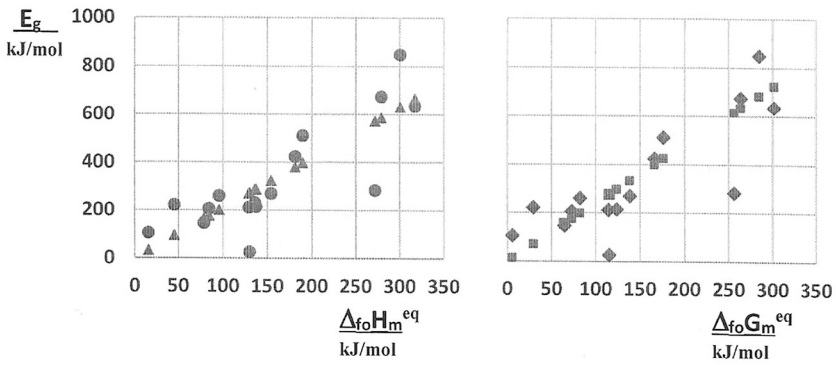

Fig. 9. Dependence of (average) published electron gap energies (Table 3) of metal oxides on equivalent molar formation enthalpy (circles, left diagram [8]) and on equivalent molar formation free energy (diamonds, right diagram [8]). Linear fits to data (triangles Eq. (24a), squares Eq. (24b)).

Table 3
Published electron gap energies (E_g^{ref}, kJ/mol) and E_g calculated from: $\Delta_{fo}H_m = H_{fo}$ Eq. (24a), $\Delta_{fo}G_m = G_{fo}$ Eq. (24b), $\Delta_{bo}{}^{ave}H_m = H_{bo}$ Eqs. (25), (9), $\Delta_{bo}{}^{elv}D_m = D_{elv}$ Eqs. (26a), (15b), $\Delta_{ro}{}^{eq}D_m = D_{ro}$, Eqs. (26b)(17b) and $\Delta_{red}{}^{abs}G_m = G_{red}$, Eq. (27a)). Corresponding metal (cation) electron gap energies (kJ/mol) calculated from: $\Delta_{red}{}^{abs}G_m = G_{red}$, and $\Delta_{red}{}^{abs}H_m = H_{red}$, (Eq. (27a), $\Delta_{red}{}^{eq}G_m = G_{eq}$, Eq. (27c)) compared to E_g calculated from a corrected model ($\Delta_{red}{}^{cor}G_m = G_{cor}$, Eq. (29)) and from first electron dissociation and electron affinity energies ($E_{ro}{}^{1st}$, Eq. (30). Upper index A = acidic and B = alkaline (basic) aqueous solutions.

M_xO_y	E_g^{ref}	H_{fo}	G_{fo}	H_{bo}	D_{elv}	D_{ro}	G_{red}	M	G_{red}	H_{red}	G_{eq}	G_{cor}	$E_{ro}{}^{1st}$
z = 1	$N_e = 2$												
Cu_2O	193-212	177	175	574	208	98,5	^{B}106	Cu	158	119	183	114	626
Ag_2O	106	32,8	13,4	329	191	95,5	^{B}114	Ag	137	87,2	116	70,8	605
z = 2	$N_e = 2$												
MgO	849	632	683	477	237	170		Mg	561	616	881	560	NS
CaO	637	667	724	539	222	119		Ca	637	686	1000	637	588
ZnO	289-325			205	257	240	^{B}158	Zn	315	327	493	194	NS
CdO	203-241	271	275	94,1	238	215	^{B}181	Cd	260	255	406	256	NS
HgO	222	95,3	70,3	-121	244	251	^{B}225	Hg	67,7	26,2	104	62,8	NS
SnO	405			314	231	172		Sn	177		342	173	601
PbO	222			138	223	177	^{B}191	Pb	217	186	339	214	681
FeO	232	286		410	237	177		Fe	266	267	417	263	703
NiO	241			391	244	192		Ni	237	235	371	234	626
CuO	116-164	165	156	223	326	238		Cu	146	125	226	141	626
z = 3	$N_e = 6$												
Al_2O_3	550-849	586	633	501	323	340		Al	579	675	710	451	536
Ga_2O_3	424	381	388	270	325	317		Ga	324	380	441	279	537
In_2O_3	270	324	332	198	303	298	^{B}292	In	276	282	390	246	529
As_2O_3	386						^{A}339	As					866
Sb_2O_3	338			147	289	302	^{A}336	Sb					730
Bi_2O_3	260	201	198	58,1	279	295	^{B}313	Bi	127		235	147	612
Ta_2O_3	434-444							Ta	336		454	287	687
Fe_2O_3	183-299	288	297	280	298	304		Fe	206	230	318	200	703
z = 4	$N_e = 4$												
SiO_2	778-878			385	410	497	^{A}525	Si					653
SnO_2	241-415			168	369	446	^{AB}388	Sn					601
TiO_2	251-453			434	380	435		Ti					651
ZrO_2	203-772			579	350	364	^{A}286	Zr	642		659	418	599
MnO_2	24	273	277	126	480	518		Mn					NS
CeO_2	284	572	615	51,2	307	335		Ce	597	681	624	396	442
z = 5	$N_e = 10$												
V_2O_5	231-260			245	484	649	^{A}536	V					600
Nb_2O_5	511	399	424	405	419	511	^{A}511	Nb					566
Ta_2O_5	424-444			448	401	474	^{A}504	Ta					697
z = 6	$N_e = 6$												
WO_3	251-270			286			^{A}647	W					680

In Fig. 10 average of published electron gap energies of metal oxides (Table 3) are plotted against average bond (equivalent atomization) energies (Eq. (9)).

The spread of averaged published electron gap energies is so large that the fit (Eq. (25)) is quite tentative. Despite many attempts, the theoretical basis of Eqs. (23) and (25) remain unclear. Since electron gap is indicative of electron conduction, electron gap energies were correlated to electrovalent bond enthalpy (Eq. (15b)) and to equivalent redox (Eq. (17b)) energies (Fig. 11).

The best fits made to the very scattered data point resulted in the following tentative relationships:

$$E_g = 0.125\,\Delta_{bo}^{elv}H_m = 0.125\,\Delta_{lat}^{eq}D_m \quad (26a)$$

$$E_g = -150.9 + 0.229\,\Delta_{ro}^{eq}D_m \quad (26b)$$

The extensive spread of averaged published electron gap data for "soft solids" shows that electrovalent bond energies and equivalent redox energy representing ionic solids are incompatible. In Table 3, the energy of formation and the average bond energy for a number of metal oxides are compared to some published E_g.

A critical evaluation of data in Table 3 is difficult, since published electron gap energies are in many cases rather uncertain. Agreements between different E_g values varies as metal cation valence (z_M) changes.

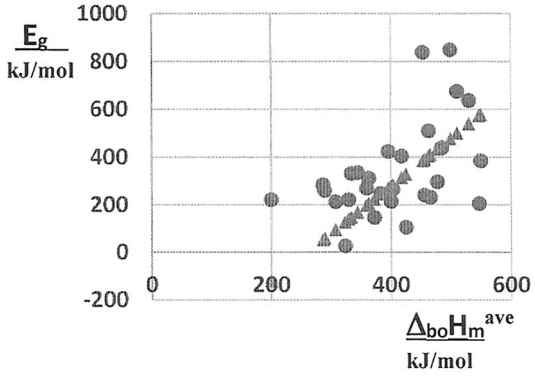

Fig. 10. Dependence of averaged published electron gap energies of metal oxides (circles, Table 3) on average bond (equivalent atomization) energies (circles, Eq. (9)). Linear fit to data (triangles, Eq. (25)).

2.3.2. *Redox potentials – electron transfer*

Metal oxides: Since electrode reactions are basically charge transfer processes, electron gap energy (E_g^o) is expected to correlate with standard reduction potentials (E_{red}^{θ}) for metals and metal oxides. Fig. 12 shows the best correlation between published electron gap energies and absolute reduction free energy.

The best fit to data points was found for absolute molar Gibbs free reduction energy as:

$$E_g^{abs} = -0.257zF\left(E_{red}^{\theta} + 4.44\right)E_{red}^{\theta} = 0.257\Delta_{red}^{abs}G_m^{\theta} \quad (27a)$$

where:

$$\Delta_{red}^{abs}G_m^{\theta} = -zF\left(E_{red}^{\theta} + 4.44\right) \quad (27b)$$

The relative molar free reduction energies were converted to

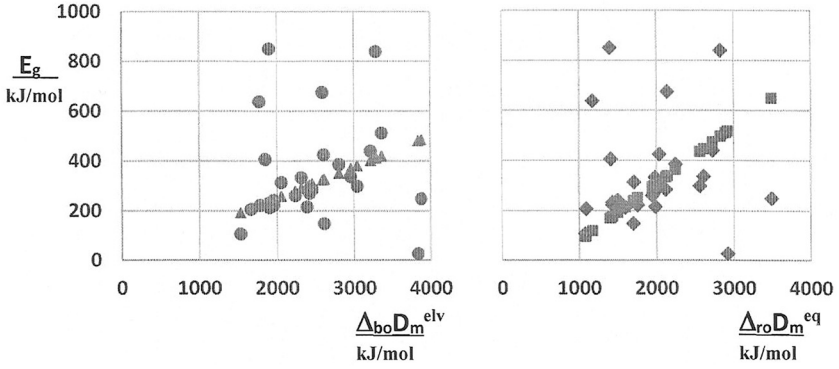

Fig. 11. Dependence of averaged published electron gap energies of metal oxides (circles, Table 3) on electrovalent bond enthalpies (Eq. (15b), left diagram) and on equivalent redox energies (Eq. (17b), right diagam). Linear fit to data: triangles, (Eq. (26a)) and squares, (Eq. (26b)),

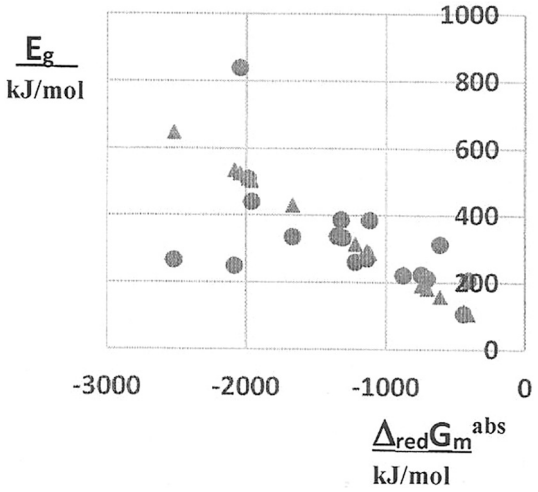

Fig. 12. Dependence of averaged published electron gap energies of metal oxides (circles, Table 3) on absolute molar free reduction energy (triangles, Eq. (27a)).

absolute values adding the absolute hydrogen potential 4.44 V (428.4 kJ/mol) [18] to standard relative reduction potential. This procedure is discussed later. A linear fit was suggested for equivalent molar reduction energy, expressed [3] as:

$$E_g^{eq} = 308.8 - 2.5FE_{red}^{\theta} = 308.8 + 2.5\Delta_{red}^{eq}G_m^{\theta} \quad (27c)$$

where:

$$\Delta_{red}^{eq}G_m^{\theta} = -FE_{red}^{\theta} \quad (27d)$$

The results are listed in Table 3. Note that some reduction potentials are measured in acidic and some other in alkaline (basic) solutions. Both result in dissolution of metal oxide (discussed later).

Metal cations: It is uncommon to report whether a reduction potential is given for a metal oxide or the corresponding metal cation, although the reduction potentials may be very different or even of opposite sign. Contrary to metal oxides (absolute values) the best fit of electron gap was made to relative molar reduction enthalpy and free energy (Fig. 13).

The best fits to data points resulted in:

$$E_g^{rel} = 184.7 + 0.923\Delta_{red}^{rel}H_m^{\theta} \quad (28a)$$

$$E_g^{rel} = 197.9 + 0.793\Delta_{red}^{rel}G_m^{\theta} \quad (28b)$$

where

$$\Delta_{red}^{rel}G_m^{\theta} = -zFE_{red}^{\theta} \quad (28c)$$

The result are listed in Table 3. Eq. (27c) has been suggested to relate electron gap energies to equivalent molar free reduction energies of metal oxide–metal standard reduction potentials [3]. A linear correlation of published electronegativity energies to E_g calculated from equivalent Gibbs reduction energies are presented in Fig. 14.

Since the suggested fit did not match data points, an improved fit was made, which resulted in the following relationship:

$$E_g^{cor} = 194.2 + 1.6\,\Delta_{red}^{eq}G_m^{\theta} = 194.2 + 1.6\,\Delta_{red}^{cor}G_m^{\theta} \quad (29)$$

These molar energies are inserted in Table 3 and Fig. 14. Computed E_g values agree mutually to some extent and therefore the claim of linear correlation is substantiated, but only to a fair degree. This is not

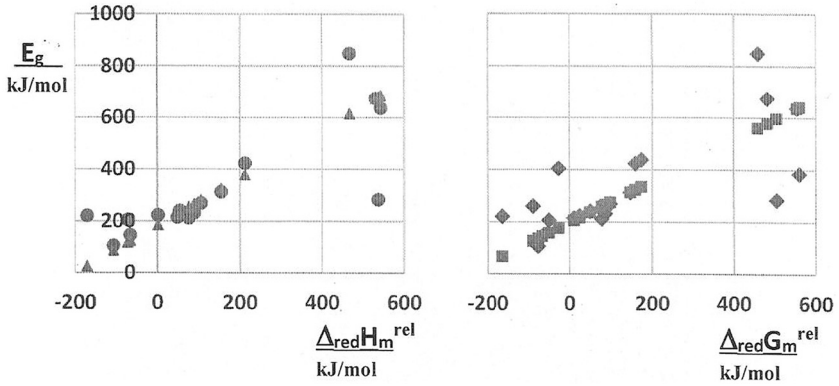

Fig. 13. Dependence of electron gap energies of metal cations (circles, Table 3) on relative molar reduction enthalpy (circles, left diagram) and on relative molar reduction free energy (diamonds, right diagram). Linear fits to data, triangles (Eq. (28a)) and squares (Eq. (28b)).

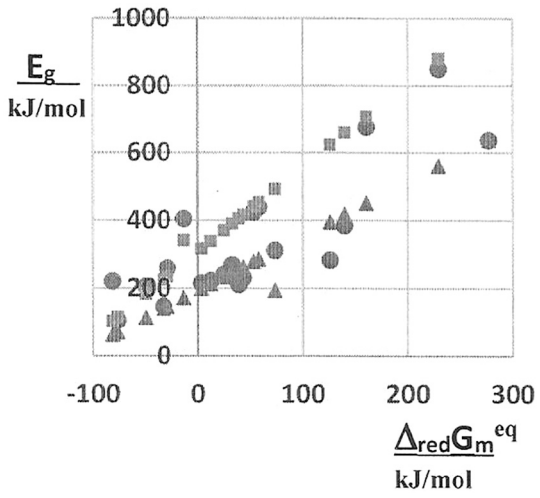

Fig. 14. Dependence of published electron gap energies of metals (circles, Table 3) on molar equivalent reduction energy. Linear fits to data: Suggested model, squares (Eq. (27c)), corrected fit, triangles (Eq. (29)).

surprising due to the very large spread of E_g values for some metal oxides.

Minimum electron gap energies (E_g^o) are generally reported in literature. Alternatively, an average electon gap energy (E_g^{1st}) may be defined as the difference in energy between the bottom of conduction band and the top of valence band. They can be determined from the first ionization energy and first electron affinity of metals (cations, kJ/mol) [13] as:

$$E_g^{1st} = -(E_v - E_c) \approx \Delta_{ion}^{1st} D_m^{\theta} - \Delta_{aff}^{1st} D_m^{\theta} = I_e^{1st} - A_e^{1st} \approx 2E_F \tag{30}$$

Bulk metals with zero or low E_g^{1st} signifies "softness", since $\Delta_{ion}{}^{1st}D_m{}^{\theta} \approx \Delta_{aff}{}^{1st}D_m{}^{\theta}$. According to hard-soft acid-base (HSAB) model [4], the degree of charge transfer between acidic and basic species is a function of the difference in their electronegativities and ceases when these become equal. Electronegativities of "soft" species are relatively insensitive to changes of electron population, which result in large charge transfers between acids and bases before equalization. Therefore metals ("soft" acids) interact readily with semiconductors ("soft" bases). Transition metals have typically $6 < E_g^o/\text{eV} < 8$ ($580 < E_g^o/(\text{kJ/mol}) < 770$) [13]. The soft-soft complexes are covalent in nature. For "hard" elements (diamond structure) $E_g^o < E_g^{ave}$. Electronegativities of "hard" species (large absolute hardness and electron gap) are very sensitive to changes in electron distribution and will rapidly equalize with only a small charge transfer [4]. The stability of the resulting hard acid – hard base HSAB complex will depend, for the most part, on the initial net charges and/or dipoles present on the interacting acid and base. The interaction is largely electrostatic in nature. Note that protons, which would be expected to be a "hard" species, are in reality quite anomalous. In contrast to "hard" alkali elements it must be placed in the "soft" category. Electron gaps of over hundred metal (hydr)oxides and corresponding metals are listed in Appendix 3. The effective number of electrons displaced in a polarized A-B bond may be estimated [13] from:

$$\Delta N_e \approx \frac{\chi_A^M - \chi_B^M}{E_{g,A}^{1st} + E_{g,B}^{1st}} = \frac{\Delta\chi^M}{\Delta E_g^{1st}} \tag{31}$$

Choosing redox reference Pt(H_2) as $\chi_B{}^M$, $E_{g,\,B}{}^*$ reference $N_e < 0$ when electrons flow to Pt at standard hydrogen electrode (SHE).

2.3.3. Summary

Electron band gap energies are of same magnitude as Paulings single bond and covalent bond energies, but roughly one-fourth of electovalent bond and Born type electrostatic and dipolar energies. E_g may be considered as an Arrhenius type activation energy for thermally induced electron transport. It is therefore not surprising that absolute, relative and equilibrium reduction energies correlated reasonably well with electron gap energies. The data in Table 3 and Appendix 3 suggest that nearly all metal (hydr)oxides are more or less "soft". Contrary to previous statements on dominating electrostatic bond energies, this observation supports the view that semimetal (hydr)oxides are more covalent than electrovalent. It seems that ionic bond energies, covalent bond energies and electron gap energies represent different level and type of incompatible ineractions, Electron gap energy, representing thermal electron transfers, is still about a decade larger that van der Waals energies, representing optical polarization.

2.4. Non-polar solids – van der Waals bond energy

Many subtle contributions, such as charge-quadrupole interactions and charge-induced dipole interactions may influence the overall energy balance, but they have so far not been considered in the evaluation of solid state properties. The collective van der Waals, Keesom (dipole-dipole), Debye (dipole-induced dipole) and London (induced dipole-induced dipole) interaction energies warrant attention. They are considered to be pairwise a electronic interactionexpanded to represent macroscopic non-polar condensed (liquid and solid) phases. Experimentally they are determined by dielectric constant (permittivity) measurements at zero frequency and by refractive index measurements at variable frequencies as Hamaker constants. Refractive indices provides an opportunity to relate Hamaker and van der Waals energies to electron gap energies.

2.4.1. Non-polar cohesion energy – Hamaker constant

The electronic interaction of metal oxides with light is weak. For a range of metal oxides the electron gap energy has been found to be related to refractive index (n_S) [5,19,20] as:

$$E_g \approx k_n\left[1 - \left(\frac{R_m}{V_m}\right)\right]^2 = k_n\left[1 - \left(\frac{n_S^2 - 1}{n_S^2 + 2}\right)\right]^2 = k_n\left(\frac{3}{n_S^2 + 2}\right)^2 \tag{32}$$

where R_m is Lorenz-Lorentz molar refraction and V_m is molar volume of the solid [5]. Originally $k_n = 20$ (assumed eV), but considering expression kJ/mol it is replaced by $k_n = k_\chi^2 = 96.487$, which is the same correction constant as was used previously (Eq. (3)). Average refactive indices [8,21] and calculated electron gap energies for samples with known Hamaker constants are listed in Table 4 and plotted as a function of molar Hamaker energy in Fig. 15.

Unfortunately, very few reliable refractive indices and Hamaker constants for solids are available. However, considering that they are average values the trends in Fig. 14 are convincing. Molar electron gap energy and molar Hamaker energies are nearly of same magnitude, but the greater molar Hamaker energies are, the smaller electron gap energies become. The dependence of electron gap on Hamaker energies of alkali halides agree roughly with those of metal oxides.

Israelachvili [21] has developed a dielectric model for the non-retarded Hamaker constant characterizing symmetric interaction of liquids and solids interacting across vacuum (assumed equal to dilute gas). The Hamaker framework is based on experimentally measurable and documented spectroscopic properties. The contributions from London (induced dipole – induced dipole), Debye (permanent dipole – induced dipole) and Keesom (permanent dipole – permanent dipole) interactions to the overall van der Waals energy are all represented in the following expression for the Hamaker constant [5,6,21]:

$$A_{SGS} = A_{\nu=0} + A_{\nu>0} \approx \frac{3kT}{4}\left(\frac{\varepsilon_S - 1}{\varepsilon_S + 1}\right)^2 + \left(\frac{3h\nu_e}{16\sqrt{2}}\right)\frac{(n_S^2 - 1)^2}{(n_S^2 + 1)^{3/2}} \tag{33}$$

where $\varepsilon_i = \varepsilon_i(0)$ are static dielectric constants and n_S are relative refractive indices of solids. The characteristic frequency (ν_e) represents the main electronic absorption frequency ($\nu_e \approx 3{*}10^{15}$/s) and $h =$

Table 4
Average published (A_{SGS}, [21,22]) and dispersive ($A_{SG}{}^{d}$, Eq. (34a)) Hamaker constants (zJ = 10^{-21} J), molar ($A_{SGm} = N_A{}^{x}A_{SGS}$) and dispersive ($A_{SGm}{}^{d} = N_A{}^{x}A_{SGS}{}^{d}$) Hamaker energies (kJ/mol). Average surface ($-\Delta_{vdW}D^{s}$, Eq(35)) and corrected surface ($-\Delta_{vdW}D^{s}_{cor}$, Eq(35)) van der Waals energies (mJ/m^2) based on equilibrium (l_{eq}) and corrected (l_{cor}) intermolecular distances (nm) for a selection of two solid blocks (water included as reference) [21,22]. Molar electron gap energies calculated from refraction indices ($E_g(k_E$ =20, eV) and $E_g{}^{std}(k_E$ =96.5, kJ/mol), Eq. (32) [5]. f-SiO_2= fused quartz, c-SiO_2= crystalline quartz, r-TiO_2= rutile.

Subst.	A_{SGS}	$A_{SG}{}^{d}$	A_{SGm}	$A_{SGm}{}^{d}$	l_{eq}	$\Delta_W D^s$	l_{cor}	$\Delta_W D^s_{cor}$	n_S	E_g	$E_g{}^{std}$
Water	53.3	34.4	32.1	20.7	0.386	9.48	0.154	59.6	1.333	12.6	60.8
BeO	146	130	87.9	78.3	0.185	113	0.074	707	1.726	7.26	35.0
MgO	115	133	69.3	79.9	0.212	67.9	0.085	424	1.735	7.17	34.6
ZnO	93	216	56.0	130	0.214	53.9	0.086	337	2.013	11.2	53.9
Al_2O_3	140	137	84.3	82.5	0.194	98.7	0.078	617	1.750	7.03	33.9
Fe_3O_4	210	346	126	209	0.197	143	0.079	897	2.420	2.92	14.1
f-SiO_2	65.5	67.4	39.5	40.6	0.180	53.6	0.072	335	1.488	10.1	48.9
c-SiO_2	89	73.9	53.6	44.5	0.180	72.9	0.072	455	1.515	9.76	47.1
r-TiO_2	249	150	92.8	265	0.201	163	0.080	1032	2.710	2.06	9.95
ZrO_2	236	263	142	158	0.212	139	0.085	866	2.160	4.05	19.5
Ti	253		152		0.323	64.3	0.129	402			
Au	473		285		0.319	123	0.128	771			
LiF	64	46.0	38.5	27.7	0.209	38.9	0.084	243	1.392	11.6	56.1
NaF	41	33.3	24.7	20.0	0.235	19.7	0.094	123	1.327	12.7	61.4
NaCl	65	81.1	39.2	48.8	0.283	21.5	0.113	135	1.544	9.37	45.2
KCl	59	67.9	35.5	40.9	0.319	15.4	0.128	96.1	1.490	10.1	48.8
KBr	62	84.9	37.3	51.1	0.334	14.7	0.134	92.1	1.559	9.17	44.2
CsI	81	148	48.8	89.1	0.387	14.4	0.155	89.7	1.788	6.67	32.2
MgF_2	59	43.1	35.5	26.0	0.205	37.2	0.082	233	1.378	11.8	57.1
CaF_2	70	55.0	42.2	33.1	0.233	34.2	0.093	214	1.434	10.9	52.8

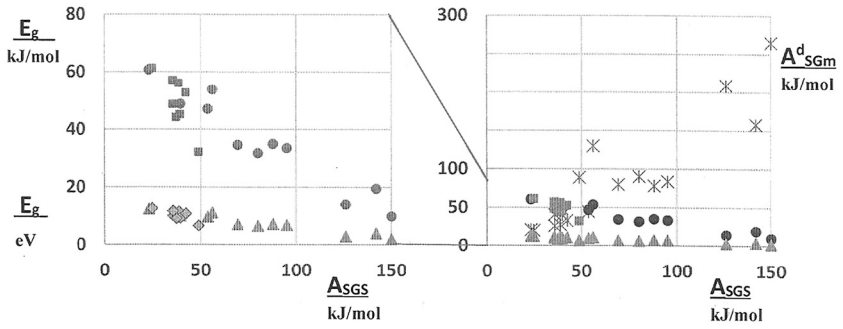

Fig. 15. Left diagram: Electron gap energies expressed as eV (Eq. (32)) ($k_{n=}$ 20 (eV), metal oxides (triangles), alkali halides (diamonds)) and expressed as kJ/mol ($k_{n=}$ 96.5, metal oxides (circles), alkali halides (squares)) plotted as a function of molar Hamaker energies, $A_{SGm} = A_{SGS}{}^{x} N_A$ (kJ/mol, N_A = Avogadros number, Table 4) Right diagram: Expanded scale to encompass dispersive molar Hamaker energies (asterisk, Eq. (34a)).

Planck's constant. Eq. (33) applies for macroscopic geometries. The first term gives the zero-frequency contribution and includes the Debye and Keesom dipolar contributions. The second term gives the dispersion energy and represents London interaction contribution. We may thus identify the two contributions [5,6] as:

$$A^{d}_{SGS} = A_{\nu>0} \approx \left(\frac{3h\nu_e}{16\sqrt{2}}\right)\frac{\left(n_S^2-1\right)^2}{\left(n_S^2+1\right)^{3/2}} \tag{34a}$$

$$A^{p}_{SGS} = A_{\nu=0} \approx \frac{3kT}{4}\left(\frac{\varepsilon_S-1}{\varepsilon_S+1}\right)^2 \tag{34b}$$

Thus:

$$A_{SGS} = A_{\nu>0} + A_{\nu=0} = A^{d}_{SGS} + A^{p}_{SGS} \tag{34c}$$

Since the optical energy ($h\nu$) exceeds the thermal energy (kT) about 500 folds, the dispersion force ($\nu > 0$) contribution is greater than the dipolar ($\nu = 0$) contribution. Therefore, $A_i^{d}\rangle\rangle A_i^{p}$. Since Hamaker constants for metal oxides are very rare, calculated dispersive and polar contribution to total Hamaker constant for other solids (M_xO_y, A_xB_y, A = Li, Na, K, Cs, Mg, Ca and B = F, Cl, Br, I) are also listed for comparison in Table 4. The energy unit zepto-Joule is introduced (zJ = 10^{-21} J) to comply with the numeric value of electron volt (1 eV = 1.6021$*10^{-19}$ J = 160.21 zJ).

Note that Hamaker constant of water has been changed from previously quoted 37.0 zJ to 53.3 zJ. The molar Hamaker energy (kJ/mol) is calculated as $A_{SGm} = A_{SGS}{}^{x} N_A$ (N_A = Avogadros number). The cohesive (vdW bond) strength is determined through a process when solids are cleaved to two planes which remain at their equilibrium distance (equilibrium bond length). The attraction (negative) energy per unit surface (J/m^2) is then [5,6,12,21–23]:

$$\Delta_{vdW}D^{s} = -\frac{A_{SGS}}{12\pi l_{eq}^2} = -\frac{A_{SGS}}{12\pi\left(r_M + r_A\right)^2} \quad \Leftrightarrow \quad \Delta_{cor}D^{s} \approx -\frac{A_{SGS}}{12\pi\left(l_{eq}/2.5\right)^2} \tag{35}$$

where $l_{eq} = r_M + r_A$ (N_C = 6, A = O, F, Cl, Br, I) or $l_{eq} = 2r_C$ (C= H_2O, Ti, Au). The van der Waals surface energy for smoothened surfaces (Eq. (35)) does, however not apply for solid surfaces which are rough on atomic scale. The number of nearest-neighbors change at surfaces which influence the average equilibrium distance by $l_{cor} \approx l_{eq}/2.5$. As shown in Table 4 and in Fig. 15 the dispersion component exceeds in some cases the total published Hamaker constant. Obviously, permittivities and refractive indices differ for some metal oxides. This is not surprising since permittivities and refractive indices are given for multiple crystal planes [8]. It is found that the polar component is of the order 1-4 zJ which should be subtracted from the total Hamaker constant to obtain comparable dispersive components. In recent compilations permittivities and refractive indices for non-isotropic metal (hydr)oxides are

characterized by three components representing different crystal planes. Water is introduced as a reference into Table 4. Without correction, van der Waals cohesive surface energy of water would be only 9.48 mJ/m^2, but considering correction of plane spacing, it raises to 56.9 mJ/m^2. Since non-polar surface tension of water is considered to be half of cohesion energy, the corrected value becomes 29.8 mJ/m^2 (25°C), which is close to experimental 21.8 mJ/m^2 at 20°C. For hydrocarbons and non-polar polymers, an average "cut-off" distance 0.165 nm (reliable to within 10-20 %) is recommended [5,21]. Unfortunately, published Hamaker constants for different solids are sparse and uncertain. The total surface tension of water at 20°C is 72.0 mJ/m^2, which may be divided into a non-polar, 21.8 mJ/m^2 (non-polar cohesive 43.6 mJ/m^2) and a polar, 51.0 mJ/m^2 (polar cohesive 102 mJ/m^2) energy part (Eq. (29)). Obviously, van der Waals non-polar cohesive surface energy for polar solids is only a fraction of the total interaction energy [5,6,21,22]. The strong adhesion between pure metal surfaces is believed to be due to short-range ($l_{eq} < 0.5$ nm) non-additive electron exchange interactions (metallic bonds). The calculated cohesive energies ($400 < \Delta_{vdW}D_{cor}{}^{s}/(kJ/m^2) < < 800$) are therefore an order of magnitude lower than typical measured vales for metals ($800 < \Delta_{vdW}D_{cor}{}^{s}/(kJ/m^2) < 8000$) [21].

2.4.2. Summary

Each type of metal (hydr)oxide energies differ by roughly one decade in the sequence, $\Delta_{lat}D_m{}^{\theta} > \Delta_{ato}D_m{}^{\theta} > E_g > \Delta_{vdW}D_m$. They represent electrovalent bond, covalent bond, thermal "bond" and polarization (optical) "bond" energies or classes of cohesive solid energies. From correlations between these properties it seems that they are not easily related to each other. Molar electron gap energies and molar Hamaker energies are of same magnitude, but $E_g(n_S) \ll E_g{}^{ref}$(Tables 3 and 4). However, the greater Hamaker constant is, the smaller electron gap energy becomes. The dependence of alkali halides on Hamaker energies agree roughly with the dependence of metal oxides.

3. Reactions of solids with water

The focus of this section is directed on change of solid properties when are brought in contact with water in absence of external additives (cations and anions).

3.1. Non-polar solids – van der Waals interaction energy

When brought into contact with water the interaction between solids is dramatically reduced. The Hamaker constant for solid-water-solid interaction may be calculated from a modified Eq. (33) [5,6,21,23] as:

$$A_{SWS}^{\exp} = A_{\nu=0} + A_{\nu>0} \approx \frac{3kT}{4}\left(\frac{\varepsilon_S - \varepsilon_W}{\varepsilon_S + \varepsilon_W}\right)^2 + \left(\frac{3h\nu_e}{16\sqrt{2}}\right)\frac{\left(n_S^2 - n_W^2\right)^2}{\left(n_S^2 + n_W^2\right)^{3/2}} \quad (36)$$

When no experimental A_{SWS} data is available, but A_{SGS} data is known, it can be estimated [5,6,21,23] as:

$$A_{SWS}^{calc} = A_{SGS} + A_{WGW} - 2A_{SW} = \left(\sqrt{A_{SGS}} - \sqrt{A_{WGW}}\right)^2 \quad (37)$$

The corresponding molar Hamaker energies are determined as $A_{SXm} = N_A \cdot A_{SXS}$. The data in Table 4 is recalculated and expanded with alternative published Hamaker constants of metal oxides in Table5.

Note that Hamaker constant of water has been changed from previously quoted 37.0 zJ to 53.3 zJ. Immersed in water the attractive van der Waals energies are reduced by almost a decade. The high solubility of alkali halides is shown as almost zero solid-solid attraction in water. The calculated Hamaker constants are further reduced from experimental values. This becomes apparent in Fig. 16, where both experimental and calculated molar Hamaker constants (kJ/mol) are plotted as a function of Hamaker energies.

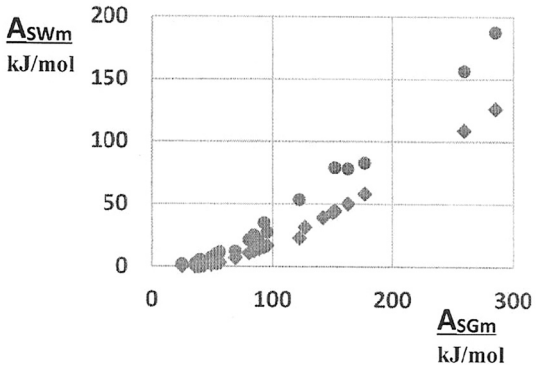

Fig. 16. Dependence of experimental (circles) and calculated (diamonds) molar solid-water-solid Hamaker energies (kJ/mol) on experimental molar solid-gas-solid Hamaker energies (kJ/mol). Data from Table 5.

3.1.1. Summary

Hamaker costant and energy is reduced when the simulated two blocks are immersed in water. Except for published very high Hamaker constants for rutile (TiO_2) and ZrO_2 [21] the interaction energy between solids in water is halved. The averaging model (Eq. (37)) underestimates A_{SWm} considerably.

3.2. Stability of metal oxides and metal hydroxides – solubility and dissolution

Metal oxides and metal hydroxides have so far been treated as dry solids. However, in contact with water the surface is hydrated. The adsorbed water reacts with metal oxides forming a sheet of hydroxyl groups. The protons exchanged at hydroxyl surface sites of metal hydroxides are denoted primary and of adsorbed water to metal oxides are denoted secondary potential determining ions. When heated the hydroxyl groups are successively removed from the surface changing the acidity (reactivity) [24]. It is not usual that temperature dependence can be subdivided into a number of (nearly) linear segments. Strongly hydrogen bound and part of the weakly bonded (germinal) hydroxyl groups are removed before 500°C. When the lateral interaction between the groups ceases a slower removal of single bonded hydroxyle groups sets in until the surface is more or less dehydoxylated at 1000°C [24]. Obviously the balance between Brϕnsted and Lewis type of surface sites can be adjusted in this way. Long heat treatment (anhilation) may, moreover redistribute surface sites. Dry metal oxide surface is rather non-polar and non-reactive. For rehydroxylation of a fully dried surface an acid treatment is usually required to enhance reactivity with water.

3.2.1. Solubility product

Solids are in most cases precipitated from aqueous solutions. Therefore, the equilibrium constant for sparingly soluble solids provides an excellent criterion for their stability in aqueous environment [25,26]. When reaction is completed at saturation we find that:

$$M_xO_y \leftrightarrow xM^{z+} + yO^{2-} \quad \Leftrightarrow \quad K_{sp} = \frac{\left[M_{aq}^{z+}\right]^x\left[O_{aq}^{2-}\right]^y}{\left[M_xO_y(s)\right]} \approx \left[M_{aq}^{z+}\right]^x\left[O_{aq}^{2-}\right]^y \quad (38)$$

where [] denotes activities and $[M_xO_y(s)] = 1$. Thermodynamically, Gibbs solubility product free energy is defined as:

$$\Delta_{sp}G_m^{\theta} = x\Delta_{fo}G_m^{\theta}\left(M_{aq}^{z+}\right) + y\Delta_{fo}G_m^{\theta}\left(O_{aq}^{2-}\right) - \Delta_{fo}G_m^{\theta}\left(M_xO_y, s\right) \quad (39a)$$

where:

$$\Delta_{sp}G_m^{\theta} = -2.3RTlogK_{sp} = 2.3RTpK_{sp} \quad (39b)$$

where 2.3 = ln10. Only a few molar Gibbs free formation energies of

metal (hydr)oxides are published and no data on hydrated oxygen is available. However, the solubility products of more than 50 samples [25,26] are listed in Appendix 4. The relationship between molar solubility product free energy, molar lattice energy and molar electrovalent bond (equivalent lattice) energy is presented in Fig. 17.

A reasonably linear correlation is found only between electrovalent bond (equivalent lattice) energy and solubility product energy.

3.2.2. Dissolution product

Another way to determine solid stability is to dissolve them in acidic aqueous solutions to release metal cations [12,25,27]:

$$M(OH)_z(s) + zH^+ \leftrightarrow M^{z+} + zH_2O$$

$$K^A_{dp} = \frac{\left[M^{z+}_{aq}\right][H_2O]^z}{\left[M(OH)_z(s)\right][H^+]^z} \approx \frac{\left[M^{z+}_{aq}\right]}{[H^+]^z} \tag{40a}$$

where [] denotes activities, $[H_2O]=1$, $[M(OH)_z(s)] =1$ and:

$$\Delta^A_{dp}G^\theta_m = -2.3RTlogK^A_{dp} = 2.3RTpK^A_{dp} \tag{40b}$$

where 2.3 = ln10. Note that reactions are not necessarily completed to saturation. In Fig. 18 dissolution product free energy is plotted as a function of solubility product energy.

Except for $Au(OH)_3$ all $M(OH)_z$ of equal z are linearly correlated. Unfortunately, there are only a limited number of data for metal hydroxides in Appendix 4. However, for each increase of valence (z_M) the correlation line is shifted to higher $\Delta_{sp}G_m{}^\theta$ values and the slope seems to be slightly reduced. The dependence of corresponding lattice and electrovalent (equivalent lattice) energies on acidic dissolution energy is shown in Fig. 19.

A linear correlation is found only between electrovalent bond (equivalent lattice) energy and acidic dissolution product energy. The dissolution of metal hydroxide, oxohydroxide or metal oxides to metal cation in alkaline solutions may be considered a reversed chelation process [25] as:

$$M(OH)_z(s) \leftrightarrow M^{z+} + zOH^- \quad \Leftrightarrow \quad K^B_{dp} \approx \left[M^{z+}_{aq}\right][OH^-]^z \tag{41a}$$

$$MO(OH)(s) + H_2O \leftrightarrow M^{z+} + 3\,OH^- \quad \Leftrightarrow$$

$$K^B_{dp} = \frac{\left[M^{z+}_{aq}\right][OH]^3}{\left[MO(OH)_2(s)\right][H_2O]} \approx \left[M^{z+}_{aq}\right][OH^-]^3 \tag{41b}$$

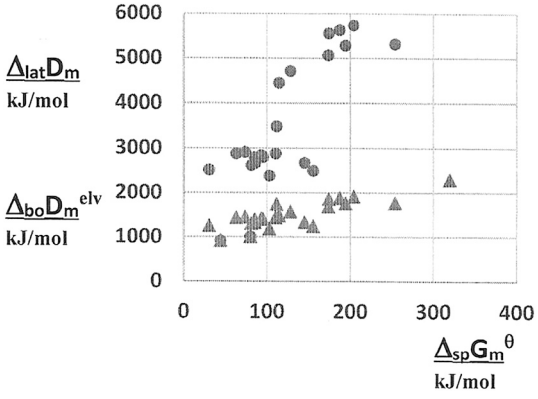

Fig. 17. Dependence of molar lattice energy (kJ/mol, circles, Eq. (15a)) and molar electrovalent bond energy (kJ/mol, triangles, Eq. (15b)) on molar solubility product energy (Eq. (39b)).

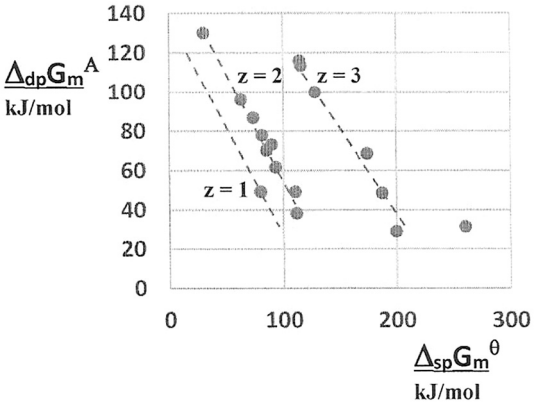

Fig. 18. Dependence of acidic molar dissolution product free energy (Eq. (40b)) on molar solubility product free energy (Eq. (39b)) for $z_M = 1$, 2 and 3 metal hydroxides.. Data from Appendix 4.

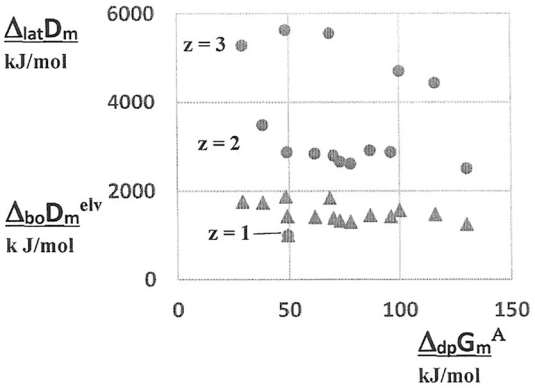

Fig. 19. Dependence of molar lattice energy (kJ/mol, circles, Eq. (15a)) and molar electrovalent (equivalent lattice) energy (kJ/mol, triangles, Eq. (15b)) on molar acidic dissolution product energy (Eq. (40)).

$$\frac{1}{2}M_2O_3(s) + \frac{3}{2}H_2O \leftrightarrow M^{z+} + 3OH^- \quad \Leftrightarrow$$

$$K^B_{dp} = \frac{\left[M^{z+}_{aq}\right][OH^-]^3}{\left[M_2O_3(s)\right]^{1/2}[H_2O]^{3/2}} \approx \left[M^{z+}_{aq}\right][OH^-]^3 \tag{41c}$$

The dissolution products obviously equal solubility product (Eq.38) for each solid. In two latter cases the dissolution product is formally altered by the participation of water (unit activity). Note that only a complete release of metal cations from metal (hydr)oxides is considered. These alternatives are also included in Appendix 4 as are a few equilibrium constants for full solvation of metal hydroxides by water [25]:

$$M(OH)_k(s) \leftrightarrow M(OH)_{k,aq} \quad \Leftrightarrow \quad k_{sol} = \frac{\left[M(OH)_{k,aq}\right]}{\left[M(OH)_k(s)\right]} \tag{42}$$

For cations with high metal valences (z_M), the dissolution does not proceed to completion and no free cations are therefore released. These processes are not included in Appendix 4.

3.2.3. Summary

The release of cations to aqueous solutions is quantified by molar standard Gibbs free energy derived from solubility product constants and from acidic and basic solid dissolution product constants. Their energies are mutually linearly correlated for each metal cation valence (z_M). Lattice and electrovalent bond energies are about one decade larger and very weakly dependent on solids dissolution product energy

into acidic solutions.

3.3. Proton exchange at surface hydroxyl sites

Metal oxides are known to hydrolyze in contact with water creating amphoteric surface groups. The acid-base character is a function of the degree of compensation for the charge on oxygen by the surrounding cations. Electroneutrality, represented by point of zero charge, results from the mutual and local compensation of ions surrounding themselves with ions of opposite charge. When protons of metal (oxo)hydroxides are exchanged with aqueous solutions they represent primary potential determining cations. However, when surface hydroxyls are result of water reactions at surface sites (not present in bulk) the protons are secondary potential determining cations.

3.3.1. Chemical equilibria

When adsorbed water reacts at surface sites to form hydroxyl groups, they resemble free hydroxyls of metal (oxo)hydroxides. Chemical proton equilibria of these surface hydroxyls provide an excellent mean to quantify surface charges. Assuming a simple two-step equilibria at singly coordinated surface hydroxyls, we can identify the following stepwise intrinsic acidity constants in acidic and alkaline aqueous [24,27,28] solutions as:

$$-M-OH \leftrightarrow -M-O^- + H^+ \quad \Leftrightarrow \quad k_{a1}^{\text{int}} = \frac{[MO^-]^s[H^+]^s}{[MOH]^s} = \frac{1}{k_{11}^{\text{int}}} \tag{43a}$$

$$-M-OH_2^+ \leftrightarrow -M-OH + H^+ \quad \Leftrightarrow \quad k_{a2}^{\text{int}} = \frac{[MOH]^s[H^+]^s}{[MOH_2^+]^s} = \frac{1}{k_{12}^{\text{int}}} \tag{43b}$$

The assignment of stepwise acid (protolysis) constants (k_{ai}^{int}) is chosen to comply with assignment of inverse proton association constants (k_{12}^{int}). For solid powders, it is common to determine surface charge density [24,27,28] as:

$$\sigma_o = \left(\frac{F}{m_S A_{sp}}\right)\left[(n_H - n_{OH})_d - (n_H - n_{OH})_b\right] \tag{44a}$$

where m_S = mass (weight) of solid with a specific area (A_{sp}). Lower index d = amount of H^+ or OH^- added to powder dispersion for each *pH* and lower index b = amount of H^+ or OH^- added to supernatant (blank) to reach the same *pH*. Expressed in terms of surface sites, the surface charge density takes the form [24,25,27,28]:

$$\sigma_o = F\left(\Gamma_{MOH_2^+} - \Gamma_{MO^-}\right) = \frac{F}{A}\left(n^s_{MOH_2^+} - n^s_{MO^-}\right) = \frac{eN_A}{A}\left([MOH_2^+]^s - [MO^-]^s\right) \tag{44b}$$

where Γ = surface excess of surface sites (mol/m^2), $[]^s = n^s$ (mol) and e= unit (electron) charge (C). The total surface density or number of OH sites per unit area is expressed as:

$$N_{OH}^s = \frac{N_A}{A}\left([MOH]^s + [MOH_2^+]^s + [MO^-]^s\right) \tag{45}$$

N_{OH}^s (sites/m^2) may be determined by acid-base titrations, chemical (gas) reactions, thermogravimetry, spectroscopy (IR, NMR), isotopic exchange and theoretical crystal plane modeling (Table 6, [24,27]). When using strongly adsorbing neutral probes (P) the contributions from surface charges and polar (solvation) interactions by water must be avoided. Therefore adsorption experiments are performed in non-polar media (hydrocarbon solutions) [24,29]. This neutralizes all dispersive (non-specific) interactions with solids. The following simple equilibrium is expected:

$$P^b + MOH^s \leftrightarrow MOHP^s \quad \Leftrightarrow \quad K_{ads}^{\text{int}} = \frac{[MOHP]^s}{[P]^b[MOH]^s} \tag{46}$$

Assuming ideal (mutually non-interacting) surface sites we may apply Langmuir isotherms to equilibrium (46) [24,29] as:

$$x_{OH}^s = \theta_{OH}^s = \frac{\Gamma_{OH}}{\Gamma_{tot}} = \frac{K_{ads}^{\text{int}}[P]^b}{1 + K_{ads}^{\text{int}}[P]^b} \quad \Leftrightarrow \quad \frac{1}{x_{OH}^s} = 1 + \frac{1}{K_{ads}^{\text{int}}[P]^b} \tag{47}$$

where θ_{OH}^s = surface coverage and Γ_{OH} = surface excess of hydroxyl groups. The intrinsic adsorption coefficient may be extracted from the slope of reversed surface mole fraction (surface excess ratio) of hydroxyl sites as a function of depletion (decreasing concentration) of probe from solution. Typical surface site densities are collected in Table 6.

The number of surface sites depends considerably on the experimental method or theoretical method used. As discussed, the density of surface sites depends also on the thermal pretreatment as shown by thermogravimetry and reactive gas adsorption experiments performed at different temperatures [24]. The fractional (degree of) dissociation or surface coverage of ionic hydroxyl groups (θ_{OH}^s) may be expressed in terms of surface charge density [24,27,28] as:

$$\theta_{OH}^s = \frac{\sigma_o}{eN_{OH}^s} = \left(\frac{[MOH_2^+]^s - [MO^-]^s}{[MOH]^s + [MO^-]^s + [MOH_2^+]}\right) \tag{48a}$$

Eq. (48a) may be rearranged as:

$$\theta_{OH}^s = \frac{\sigma_o}{eN_{OH}^s} = \left(\frac{([MOH_2^+]^s/[MOH]^s) - ([MO^-]^s/[MOH]^s)}{1 + ([MO^-]^s/[MOH]^s) + ([MOH_2^+]^s/[MOH]^s)}\right) \tag{48b}$$

In order to relate surface (s) proton equilibria to measured bulk (b) acidity Boltzmann distribution relation is engaged:

$$[H^+]^s = [H^+]^b e^{-F\psi_o/RT} \tag{49}$$

Introducing intrinsic acid constants (Eq. (43a),(43b)) and Boltzmann distribution equilibrium (Eq. (49)), Eq. (48b) takes the form [24,27,28]:

$$\theta_{OH}^s = \frac{\sigma_o}{eN_{OH}^s} = \left(\frac{\left([H^+]^b e^{-F\psi_o/RT}/k_{a2}^{\text{int}}\right) - \left(k_{a1}^{\text{int}}/[H^+]^b e^{-F\psi_o/RT}\right)}{1 + \left(k_{a1}^{\text{int}}/[H^+]^b e^{-F\psi_o/RT}\right) + \left([H^+]^b e^{-F\psi_o/RT}/k_{a2}^{\text{int}}\right)}\right) \tag{50}$$

Nernst equation may be used to establish the surface potential with reference to point of zero charge [24,27,28] as:

$$\psi_o = \frac{RT}{F} ln\left(\frac{[H^+]^s}{[H^+]^s_{PZC}}\right) \quad \Leftrightarrow \quad \frac{[H^+]^s}{[H^s]^s_{PZC}} = e^{F\psi_o/RT} \tag{51}$$

Since ψ_o= 0 at point of zero charge, Boltzmann Eq. (49) reduces to $[H^+]_{PZC}{}^b = [H^+]_{PZC}{}^s$, which combined with Eq. (51) gives $[H^+]_{PZC}{}^b = [H^+]_{PZC}{}^s = [H^+]^s$. The product of acidity constants of reactions (43a) and (43b) is:

$$K_a^{\text{int}} = k_{a1}^{\text{int}} k_{a2}^{\text{int}} = \left(\frac{[MO^-]}{[MOH_2^+]}\right)[H^+]^2 \tag{52a}$$

At point of zero charge the surface concentrations (activities) of MO^- and $MOH_2{}^+$ are equal and Eq. (52a) can be used to express $[H^+]_{PZC}{}^s$ in terms of intrinsic acidity constants [27,30] as:

Table 6
Surface hydroxyl site density per nm^2: $N_1{}^s$ = theoretical modeling, $N_2{}^s$ = isotopic exchange, $N_3{}^s$ = IR spectroscopy, $N_4{}^s$ = chemical reactions (total, acidic, basic OH) and $N_5{}^s$ = acid-base titrations (acidic, basic OH) [24,27]. * = average value.

	$N_1{}^s$	$N_2{}^s$	$N_3{}^s$	$N_4{}^s$	$N_{4+}{}^s$	$N_{4-}{}^s$	$N_{5+}{}^s$	$N_{5-}{}^s$
MgO	22		19*					
ZnO				2.0	2.7			
αAl_2O_3								2.7
γAl_2O_3								
αFe_2O_3	7.1*	22.4	7.8*	4.5	3.1	4.6	10.8	13.5
αFeO(OH)	16.8	16.4						
SiO_2	5.2*	11.4	4.7*	4.2				3.5
SnO_2				2.2	2.0	2.5		<0.1
TiO_2	12.1	12.5	11.3	5.8	7.0	3.5	2.6	4.2
CeO_2				2.7	4.3	4.5		

$$[H^+]^b_{PZC} = [H^+]^s_{PZC} = \sqrt{k^{int}_{a1}k^{int}_{a2}} = \sqrt{K^{int}_a} \quad (52b)$$

Eq. (52b) may be rewritten [24,27,28] as:

$$pH_{PZC} = -log[H^+]^b_{PZC} = \frac{pK^{int}_a}{2} = \frac{pk^{int}_{a1} + pk^{int}_{a2}}{2} \quad (52c)$$

Eq. (52c) can be related back to surface potential (Nernst Eq. (51)) as:

$$\psi_o = \frac{2.3RT}{F}(pH_{PZC} - pH) \quad (53)$$

In neutral *pH* range the total surface density or number of OH sites per unit area (Eq. (45)) may be divided into contributions of predominantly acidic and basic groups [27] as:

$$N^s_+ = \frac{N_A}{A}\left(\left[M-OH^+_2\right]^s + [M-OH]^s\right) \quad (54a)$$

$$N^s_- = \frac{N_A}{A}\left([M-O^-]^s + [M-OH]^s\right) \quad (54a)$$

Obviously, neutral hydroxyls are shared depending whether they participate in acidic (Eq. (40a)) or basic (Eq. (41a)) reactions. This simple proton exchange equilibrium at single coordinated hydroxyl sites depend on the relative strengths of the acidic ($-MOH_2^+$) and basic ($-MO^-$) groups. The ratio of neutral ($-MOH^o$) to ionized sites may be expressed [24,28] as:

$$\Delta pK^{int}_a = pk^{int}_{a1} - pk^{int}_{a2} = log\frac{[MOH^o]^2}{[MO^-][MOH^+_2]} \quad (55)$$

We may draw the following general conclusions about surface sites:

- If $\Delta pK_a{}^{int} > 4$ (high), then [-MOH] >> [-MOH_2^+] ≈ [-MO^-] and the acid [-MOH_2^+] is much stronger than the acid [-MOH^o], and the base [-MO^-] is much stronger than the base [-MOH^o]. The predominant species are [-MOH^o] and the number of ionized species is very small.
- If $\Delta pK_a{}^{int} < 4$ (small), the [-MOH_2^+] and [-MOH^o] acids and [-MO^-] and [-MOH^o] bases have similar strengths. Then the number of charged groups [-MOH_2^+] and [-MO^-] is large.
- If $pK_a{}^{int} >> 2pH_{PZC}$ then the acid strength is greater than the base strength ([-MOH_2^+] > (MO^-]).

The sum and difference of logarithmic intrinsic constants, points of zero charge and relative number of surface sites for some metal oxides are collected in Table 7.

The left side intrinsic equilibrium constants were determined in 0.1 mol/dm^3 electrolytes. The right side intrinsic equilibrium constants have been corrected to zero electrolyte concentration [27]. Note that $N_+{}^s \neq N_-{}^s$ as expected for truly amphoteric surface sites. The number of hydroxyl sites are lower than those extracted from other experiments presented in Table 6. As shown the arithmetic average of logarithmic equilibrium constants (Eq. (52c)) provide a simple way to establish pH_{PZC}. On the contrary, pH_{PZC} is another expression for half overall intrinsic acidity constants for surface hydroxyl groups. Unfortunately, the left side equilibrium constants suggests that $\Delta K_a{}^{int} < 4$, while the right side equilibrium constants suggest that $\Delta K_a{}^{int} > 4$. Since the calculated pH_{PZC} for left side equilibrium constants agreed with experimental values, it may be concluded that $\Delta K_a{}^{int} < 4$ is more reliable. The density of surface sites related to these acid constants are, however rather small as compared to those listed in Table 6, which contradict the prediction. When *pH* necessary for experiments become extreme this may influence solid dissolution which enhance uncertainty.

Jolivet [11] have criticized the two-step proton exchange equilibria at surface hydroxyls and claimed that no hydroxyl group exhibit an amphoteric character. Instead, a single equilibrium should be assigned to each hydroxyl group. According to James and Parks [27], monofunctional or single-site surfaces are not common among natural metal oxides, except silica. Functional groups on single-site surfaces may be weak acids or weak bases. Either of Eq. (43a) or (43b) may be chosen to describe the dissociation degree of a weak acid site and apply the procedures to extract $k_{ai}{}^{int}$. Point of zero carge (pH_{PZC}) values [31–34] are listed in Appendix 5.

3.3.2. Multisite complexation (MUSIC) model

Solids can exist in different crystal forms. Some preparation procedures may result in imperfections at crystal faces, giving rise to different chemical compositions exhibited as different ratios of singly and double coordinated surface groups. The stoichiometry, texture and structure host a variety of surface sites, which may catalyze chemical reactions and chemisorb a variety and ionic species. Br*ϕ*nsted acid (proton donor) ability has been ascribed to strained oxygen bridges resulting from two adjacent hydroxyl ions being active centers. The multisite complexation (MUSIC) model is developed to account for these surface site differences. It is based on Paulings formal bond valence, $\upsilon_M = z_M/m$, where m is the coordination number of metal cation. The negative surface oxygen charge may remain uncompensated maintaining a formal partial charge [11]:

$$-M-O-H \;\Leftrightarrow\; \delta_M = m\upsilon_M - z_O + nz_H \quad (56)$$

where m = number of attached metals and n = number of attached protons. For singly coordinated OH ligads the formal partial charge may vary as:

$$-Mg-OH \Leftrightarrow\; \upsilon_M = 2/6 = 1/3 \;\Leftrightarrow\; \delta_M = 1/3 - 2 + 1 = -2/3 \;\Leftrightarrow\; -Mg-OH^{2/3-}$$

$$-Si-OH \Leftrightarrow\; \upsilon_M = 4/4 = 1 \;\Leftrightarrow\; \delta_M = 1 - 2 + 1 = 0 \;\Leftrightarrow\; -Si-OH^0$$

$$-Ti-OH \Leftrightarrow\; \upsilon_M = 4/6 = 2/3 \;\Leftrightarrow\; \delta_M = 2/3 - 2 + 1 = -1/3 \;\Leftrightarrow\; -Ti-OH^{1/3-}$$

Increasing the number of attached metals changes obviously the partial charge:

Table 7
Comparison of calculated (pH_{calc}, Eq. (52c)) to experimental (pH_{exp}) point of zero charges. Number of acidic (N_+, Eq. (54a)) and basic N_-, Eq. (54b)) surface sites per nm^2 [24,27]. A = anatase and R = rutile.

	$pk_{a1}{}^{int}$	$N_+{}^s$	$pk_{a2}{}^{int}$	$N_+{}^s$	pH_{calc}	pH_{exp}	ΔpK_a	$pk_{a1}{}^{int}$	$pk_{a2}{}^{int}$	pH_{calc}	pH_{ref}	ΔpK_a
αAl_2O_3	9.70	2.7	8.50		9.10	9.10	1.20				8.95	
γAl_2O_3	9.05	0.39	7.89	0.42	8.47	8.50	1.16	11.8	5.2	8.50	9.03	6.6
αFe_2O_3	10.1	13.5	8.86	1.1	9.48	9.27	1.24	10.3	6.7	8.50	8.35	1.8
$\alpha FeO(OH)$	8.20	0.54	6.74	0.72	7.47	7.55	1.46	10.5	4.2	7.35	9.15	6.3
SiO_2	4.60	3.5	1.34		2.97	3.00	3.26	7.2		7.2	2.30	
SnO_2	6.50	<0.1	4.42		5.46	5.50	2.08				5.45	
TiO_2	6.38	4.2	5.41	2.6	5.90	6.00	0.97					
A-TiO_2								8.7	3.2	5.95	5.93	5.5
R-TiO_2								9.1	2.7	5.90	5.68	6.4

$$-Al-OH \Leftrightarrow \ \upsilon_M = 3/6 = 1/2 \ \Leftrightarrow \ \delta_M = 1/2 - 2 + 1 = -1/2 \ \Leftrightarrow \ Al-OH^{1/2-}$$

$$-Al_2-OH \Leftrightarrow \ 2\upsilon_M = 2/2 = 1 \ \Leftrightarrow \ \delta_M = 1-2+1 = 0 \ \Leftrightarrow \ Al_2-OH^0$$

$$-Al_3-OH \Leftrightarrow \ 3\upsilon_M = 3/2 \ \Leftrightarrow \ \delta_M = 3/2 - 2 + 1 = +1/2 \ \Leftrightarrow \ Al_3-OH^{1/2+}$$

The number of protons associated to surface oxygens (n) varies with pH. Considering stepwise proton association to one hydrolyzed water molecule adsorbed to a surface site:

$$-M_m^{m\upsilon+}\cdot O^{2-} + H^+ \leftrightarrow -M_m^{m\upsilon+}\cdot OH^{1-} \quad \Leftrightarrow \quad k_{m1}^{\text{int}} = \frac{\left[M_m OH^{m\upsilon_M-1}\right]^s}{\left[M_m O^{m\upsilon_M-2}\right]\left[H^+\right]^s} = \frac{1}{k_{a1}^{\text{int}}} \tag{57a}$$

$$-M_m^{m\upsilon+}\cdot OH^{1-} + H^+ \leftrightarrow -M_m^{m\upsilon+}\cdot OH_2^o \ \Leftrightarrow \ k_{m2}^{\text{int}} = \frac{\left[M_m OH_2^{m\upsilon_M}\right]^s}{\left[MOH^{m\upsilon_M-1}\right]^s\left[H^+\right]^s} = \frac{1}{k_{a2}^{\text{int}}} \tag{57b}$$

Since the acidity increases with enhanced positive formal valence MUSIC model allows for an estimate of these intrinsic acidity constants based on purely Born type of electrostatic energy.

Jolivet's modifications: The gain (negative sign) of molar Gibbs free Born type energy due to the approach of protons to $-O^{2-}$ or $-OH^-$ groups [11,28] is:

$$\Delta_{Born}^{H-O}G_m = -\left(\frac{N_A}{4\pi\varepsilon_o}\right)\frac{(z_H e)\left(z_{O(H)}e\right)}{l_{H-O}\varepsilon_r^s} \tag{58}$$

In addition, the chemical contribution to total Gibbs energy is combined with proton exchange energy to characterize the first proton association step (k_{m1}^{int}) [11,28] as:

$$\Delta_H G_m = \Delta_{Born}^{H-O}G_m + \Delta_{H-O}^{chem}G_m = -\left(\frac{N_A}{4\pi\varepsilon_o}\right)\frac{(z_H e)(z_O e)}{l_{H-O}\varepsilon_r^s} + \Delta_H^{chem}G_m \tag{59a}$$

which equals 34.06 kJ/mol when distances $l_{H\text{-}O}$ are given as Ångströms (10^{-10} m). The corresponding second proton association step (k_{m2}^{int}) is characterized [11,28] by:

$$\Delta_H G_m = \Delta_{Born}^{H-OH}G_m + \Delta_{H-OH}^{chem}G_m = -\left(\frac{N_A}{4\pi\varepsilon_o}\right)\frac{(z_H e)(z_{OH}e)}{l_{H-OH}\varepsilon_r^s} + \Delta_H^{chem}G_m \tag{59b}$$

which equals 20.16 kJ/mol when distance $l_{H\text{-}OH}$ are given as Angstroms (10^{-10} m). No information was, however provided on the parameters involved [11]. The loss (positive sign) of molar Gibbs free Born type energy (kJ/mol) due to the approach of protons to surface site metals is characterized [11,28] by:

$$\Delta_{Born}^{H-M}G_m = \left(\frac{N_A}{4\pi\varepsilon_o}\right)\frac{N_M(z_H e)(m\upsilon_M e)}{l_{H-M}\varepsilon_r^s} = 52.7\left(\frac{m\upsilon_M}{l_{H-M}}\right) \tag{60}$$

when distances $l_{H\text{-}M}$ are given as Angstroms (10^{-10} m). Note that the distance between the metal and proton varies depending on the configuration. This distance may be extracted from crystallographic data [35,36]. The relative permittivities at the surface (ε_r^s) are microscopic effective dielectric (fitting) constants. Due to the simplicity of MUSIC model, they are without real physical significance. The total absolute standard molar Gibbs free energy is obtained as:

$$\Delta_H G_m^\theta = -RTlnK_{mn}^{\text{int}} = \left(\Delta_{Born}^{H-O(H)}G_m^\theta + \Delta_H^{chem}G_m^\theta\right) + \Delta_{Born}^{H-M}G_m^\theta \tag{61}$$

where $K_{mn}^{\text{int}} = k_{m1}^{\text{int}}k_{m2}^{\text{int}}$. These values allow estimation of proton association constants for singly coordinated ($m = 1$) Al [11] as:

$$-Al-O^{-3/2} + H^+ \leftrightarrow -Al-OH^{-1/2} \Leftrightarrow pk_{12}^{\text{int}} = 34.06 - 52.7(0.5/2.59) = 23.89$$

$$-Al-OH^{-1/2} + H^+ \leftrightarrow -Al-OH_2^{+1/2} \Leftrightarrow pk_{12}^{\text{int}} = 20.16 - 52.7(0.5/2.59) = 9.98$$

where $l_{H\text{-}M}$ =2.59 Å. For doubly coordinated ($m = 2$) Al the proton association constants may be derived [11] as:

$$-Al_2-O^- + H^+ \leftrightarrow -Al_2-OH \ \Leftrightarrow \ pk_{21}^{\text{int}} = 34.06 - 52.7(1/2.43) = 12.37$$

$$-Al_2-OH + H^+ \leftrightarrow -Al_2-OH_2 \ \Leftrightarrow \ pk_{22}^{\text{int}} = 20.16 - 52.7(1/2.43) = -1.53$$

where $l_{H\text{-}M}$ =2.43 Å. Gibbsite Al(OH)$_3$ particles are hexagonal platelets. The upper and lower large 001 faces exhibit only doubly coordinated OH groups with a density of 13.8 OH/nm^2. The particle sides (*hk0* faces) contain single and doubly coordinated OH groups with a density of 9.6 and 4.8 OH/nm^2, respectively [11,27]. Acicular particles of Goethite (α-FeO(OH)) have three type crystal faces. The 100 faces bear singly ($m = 1$), doubly ($m = 2$) and triply ($m = 3$) coordinated Fe. The density of all three face types are 3.3 OH/nm^2, as calculated using the dimensions of the unit cell. The 010 and 001 faces carry single 7.1 OH/nm^2 and doubly 8.6 OH/nm^2 coordinated OH groups, respectively [11,27]. The 100 faces of CeO_2 particles contain doubly coordinated 6.8 OH/nm^2 groups, 111 faces both singly and triply coordinated 7.9 OH/nm^2 goups each [11]. The same is true for 110 faces which carry 9.6 OH/nm^2. Table 8 summarizes proton association constants for aluminium, iron and cerium hydroxides.

The found acidity of surface groups are quite reasonable and increases dramatically with the degree of coordination of hydroxyl groups. This effect can be visualized by hydrogen bond energy in surface hydroxyl groups, which decreases with increasing coordination. The weakening O-H bond with the coordination number of hydroxyl ligands is also reflected by the decrease of infrared resonance frequency [11]. Other metal hydroxide particles contain surfaces with a range of coordination options. A general observation is that no surface hydroxyl exhibits amphoteric character, in spite of the fact that particles maybe positively and negatively charged. Contrary to general belief, each surface hydroxyl is involved in only one protonation equilibrium over the entire pH range. Therefore, successive involvement of two protons on the same hydroxyl group appears quite unrealistic. As discussed, this conclusion was opposed by James and Parks [27].

Parks' modifications: Parks considered simultaneous double proton association to single coordinated surface sites [31]:

$$-M-O^- + 2H^+ \leftrightarrow -M-OH_2^+ \quad \Leftrightarrow \quad K_{12}^{\text{int}} = \frac{\left[MOH_2^+\right]^s}{\left[MO^-\right]^s\left[H^s\right]^2} \tag{62}$$

where $K_{12}^{\text{int}} = k_{11}^{\text{int}}k_{12}^{\text{int}}$. He assumed that the primary electrostatic work was due to the approach of $2H^+$ to $-MO^-$. Including the non-Coulombic interaction energy $\Delta_{2H}^{chem}G$, the pH at point of zero charge becomes [31]:

$$\Delta_{2H}G = -kTlnK_{1,2}^{\text{int}} = \left[\frac{(2z_H e)(z_O e)}{\varepsilon_o\varepsilon_r^s l_{2H-O}} - \Delta_{2H}^{chem}G\right] - \frac{(2z_H e)(z_O e)}{\varepsilon_o\varepsilon_r^s l_{2HO-M}} \tag{63}$$

where $l_{2H\text{-}O=}\ r_O$ =1.40 Å and $l_{2HO\text{-}M=}\ l_{2H\text{-}O} + r_M = (2.80 + r_M)$ Å. The factor 2 results from two protons participating in the equilibrium. The standard Gibbs free energy is expressed in kcal/mol ($1/4\pi\varepsilon_o$ was omitted). Since $[MOH_2^+]^s = [MO^-]^s$ at point of zero charge, pH_{PZC} the equilibrium constant may be written (Eq. (52c)) as:

$$K_{12}^{\text{int}} = \frac{1}{\left[H^s\right]^2} \quad \Leftrightarrow \quad pH_{PZC}^s = -log[H^s] = \frac{1}{2}logK_{12}^{\text{int}} \tag{64a}$$

Eq. (64a) may be expressed as molar Gibbs free energy of intrinsic proton association:

$$\Delta_{PZC}^{\text{int}}G_m = -4.6RT\,pH_{PZC} \tag{64b}$$

where 4.6 = 2ln10. The pH_{PZC} values in Table 7 are listed with a number

Table 8
Intrinsic proton association constants of singly, doubly and triply coordinated surface hydroxyl groups of aluminum hydroxide, iron hydroxide and cerium hydroxide [11].

	-AlOH$^{1/2-}$	-AlOH$_2^{1/2+}$	-Al$_2$OH^0	-Al$_2$OH$_2^+$	-Al$_3$OH$^{1/2+}$	
pk$_{m,n}$	24.0	10.0	12.3	-1.5	1.6	
		-FeOH$_2^{1/2+}$	-Fe$_2$OH	-Fe$_2$OH$_2^+$	Fe$_3$OH$^{1/2+}$	
pk$_{m,n}$		10.7	13.7	0.1	4.3	
	-CeOH$^{1/2-}$	CeOH$_2^{1/2+}$	-Ce$_2$OH^0	-CeOH$_2^+$	-Ce$_3$OH$^{1/2+}$	-Ce$_3$OH$_2^{3/2+}$
pk$_{m,n}$	23.0	9.2	14.0	0	4.2	-9.8

of other pH_{PZC} values in Appendix 5. A combination with Eq. (64) results in:

$$pH_{PZC} = \frac{1}{2.3kT}\left[\frac{(z_H e)(z_O e)}{\varepsilon_o \varepsilon_r^s l_{2H-O}}\right] - \frac{1}{2.3kT}\left[\frac{(z_H e)e}{\varepsilon_o \varepsilon_r^s}\left(\frac{z_M}{l_{2HO-M}}\right)\right] - \frac{\Delta_{2H}^{chem}G}{4.6kT} \quad (65a)$$

With reference to pH_{PZC} of Al_2O_3(hyd) and MgO(hyd) Eq. (65a) was rewritten for species with $N_C = 6$ [31] as:

$$pH_{PZC} = 18.6 - 11.5\left(\frac{z_M}{l_{2HO-M}}\right) - \frac{\Delta_{2H}^{chem}G}{4.6kT} \quad (65b)$$

where energies are expressed as kcal/mol and lengths are given in Angstrom. The points of zero charge, in particular for transition metals, must be corrected for crystal field stabilization energy (CFSE) since CFSE increases the stability of M-OH bonds (increased basicity) which decreases pH_{PZC} and contributes to $\Delta_{2H}{}^{chem}G$. Kosmulski evaluated Parks dataset and compared calculated points of zero charge (Eq. (65b)) to experimental values [31,32]. The selected most reliable pH_{PZC} values [31–35] are listed in Appendix 5. Experimental, calculated and reference points of zero charges are plotted as a function of $z_M/l_{2HO\text{-}M}$ (Eq. (65b)) and of $\upsilon_M/l_{HO\text{-}OM}$, (Eq. (69b)) in Fig. 20.

Yoon et.al. modifications: Yoon et-al. [35] applied Parks two proton association equilibrium to adsorbed water molecules, corrected for formal charges as:

$$-M^{\upsilon+}\cdot O^{2-} + 2H^+ \leftrightarrow -M^{\upsilon+}\cdot OH_2^o \quad \Leftrightarrow \quad K_{12}^{int} = \frac{\left[MOH_2^{\upsilon+}\right]^s}{\left[M_m O^{(\upsilon-2)+}\right]\left[H^s\right]^2} = \frac{1}{K_{a2}^{int}} \quad (66)$$

At point of zero charge (pH_{PZC}), the overall charge neutrality imposes the condition:

$$|\upsilon_M - 2|\left[MO^{(2-\upsilon_M)-}\right] = |\upsilon_M|\left[MOH_2^{\upsilon_M}\right] \quad (67)$$

at charge neutrality point, when $\upsilon < 2$. Introducing Eq. (67) into Eq. (66) we [35] obtain:

$$K_{12}^{int} = \frac{|\upsilon_M - 2|}{|\upsilon_M|\left[H^s\right]^2} \quad \Leftrightarrow \quad 2pH_{PZC} = logK_{12}^s - log\left(\frac{\upsilon_M - 2}{\upsilon_M}\right) \quad (68)$$

Point of zero charge may be expressed in terms of Gibbs free energy of proton association (kcal/mol) [35] as:

$$pH_{PZC}^s = \frac{1}{2.3kT}\left[\frac{(z_H e)(z_O e)}{\varepsilon_o \varepsilon_r^s l_{H-O}} - \frac{\Delta_{2H}^{chem}G^\theta}{2}\right] - \frac{1}{2.3kT}\left[\frac{(z_H e)e}{\varepsilon_o \varepsilon_r^s}\left(\frac{\upsilon_M}{l_{HO-OM}}\right)\right] - \frac{1}{2}log\left(\frac{\upsilon_M - 2}{\upsilon_M}\right) \quad (69a)$$

where $pH_{PZC}{}^s \approx pH_{PZC}{}^b$, $l_{2H\text{-}O} = 1.01$ Å (ice) and $l_{HO\text{-}OM} = l_{H\text{-}O}$ (ice) + $l_{O\text{-}M}$ (cry) = (1.01 + $l_{O\text{-}M}$ (cry)) Å. The crystal lattice, $l_{O\text{-}M}$ (cry) value was determined from crystal structure determi-nations [36,37]. With reference to $pH_{PZC}(\alpha Al_2O_3) = 9.1$ and $pH_{PZC}(MgO) = 12.4$ Eq. (68) could be condensed [35] as:

$$pH_{PZC}^s = pH_{PZC}^b = 18.43 - 53.12\left(\frac{\upsilon_M}{l_{HO-OM}}\right) - \frac{1}{2}log\left(\frac{\upsilon_M - 2}{\upsilon_M}\right) \quad (69b)$$

In particular for some transition metals and metal hydroxides the following correction for crystal field stabilization energy was applied:

$$pH_{PZC} = 18.43 - 53.12\left[\left(\frac{\upsilon_M}{l_{HO-OM}}\right) + 5.61\cdot 10^{-4} CFSE\right] - \frac{1}{2}log\left(\frac{\upsilon_M - 2}{\upsilon_M}\right) \quad (70a)$$

where the correction constant was determined from $pH_{PZC}(Co(OH)_2) = 11.4$ with $CFSE(Co^{2+}6H_2O) = 33$ kcal/mol. Eq. (70a) may be expressed as:

$$pH_{PZC} = 18.43 - 53.12\left(\frac{\upsilon_M}{l_{HO-OM}}\right)_{eff} - \frac{1}{2}log\left(\frac{\upsilon_M - 2}{\upsilon_M}\right) \quad (70b)$$

The point of zero charge predictions of Eqs. (69b) and (70b) are listed in Appendix 5. It may be of interest whether the electronegativity of metal (hydr)oxides influence proton exchange on surface sites. In Fig. 21 the point of zero charge is plotted as a function of Paulings single bond (Eq. (3)) and Jolivets average molecular electronegativity (Eq.(10a), (10b)) listed in Appendix 3.

Neither electronegativities do correlate with pH_{PZC}. There seem to be some loose correlation between Jolivets average molecular electronegativities and pH_{PZC}, but this relationship is limited to different sets of

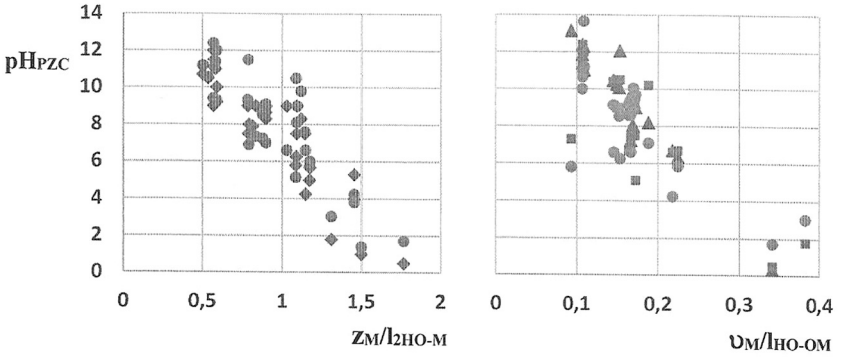

Fig. 20. Left diagram: Experimental (diamonds, [31,32]) and reference (circles, [33,34]) points of zero charges (pH_{PZC}) plotted against adjusted ionic potential ($z_M/l_{2HO\text{-}M}$), Eq. (65b)). Right diagram: Calculated (triangle, Eq. (52c)), experimental (squares, [35]) and published (circles, [33,34]) point of zero charges (pH_{PZC}) plotted against ($\upsilon_M/l_{HO\text{-}OM}$, Eq. (69b)).

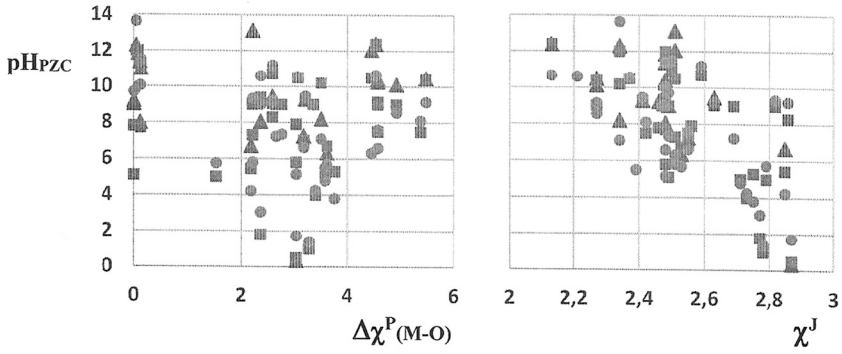

Fig. 21. Calculated (triangle, Eq. (52c)), experimental (squares, [32,35]) and reference (circles, [33,34]) point of zero charges (pH_{PZC}, Appendix 5) plotted against Pauling average single bond electronegativity differences (eV, left diagram, (Eq. (3), Appendix 3) and against Jolivet's average molecular electronegativities (eV, right diagram, (Eq.(10a),(10b), Appendix 3).

metal (hydr)oxides.

A more refined analysis of MUSIC model results shows that dissociation equilibrium must be considered separately for each surface group. The *pH* at which the net charge is zero depends on the relative fractions of each type of group, as well as on their respectivepk_{mn}^{int}. For many oxides, cancellation of the global charge may take place through global compensation. Moreover, the influence of neighboring hydroxyl groups must be taken into account. The number of hydroxyl groups decrease linearly within various temperature ranges [24]. However, when the com-munication between –OH groups ceases, the dependence on temperature is strongly reduced. In this case the rehydroxylation becomes much slower. In porous matrixes double (gemini) and triple coordinated hydroxyl groups exist which are not described by the MUSIC model and they are only fractionally accessible to chemical reactions. Appendix 5 show point of zero charges for some metal oxides and metal hydroxides adjusted to fit $pH_{PZC}(MgO) = 12.4$ and $pH_{PZC}(Al_2O_3) = 9.1$. Since 6-coordination of elements were assumed, there is a large difference for compounds with different coordination number. In compounds containing hydrogen bonds ($Zn(OH)_2$) , the experimental pH_{PZC} is expected to be lower than the calculated one. The hydroxyl ion in such compounds tend to anchor non-reversibility solution hydroxyl ions within surface layer. Corrective terms must be added for elements stabilized by crystal field, because the CFSE contributes to the $\Delta_{2H}{}^{chem}G$ term. The surface charge reversal is explained by considering an average reaction site involving two steps of proton association defined by Eq. (57a) and (57b). In MUSIC model this corresponds to $m\upsilon_M = 1$ and neutral hydroxyl groups. If one of the $pk_{m,n}$ values are outside pH range a single equilibrium is obtained with $pH_{PZC} = pk_{a,n}$.

3.3.3. Summary

Instead of extracting proton association energies, MUSIC model is used to express intrinsic proton association constants (Eq. (64)) in terms of point of zero charge (pH_{PZC}) as a function of z_M. A crystal field stabilization energy is introduced to correct Born type electrostatic repulsion energy for some transition metals. This is considered sufficient representation of chemical energy. The pH_{pzc} values in Appendix 5 supports the rough classification of metal oxides and hydroxides shown in Table 9. Molar Gibbs free energy of intrinsic proton association ($\Delta_{PZC}{}^{int}G_m = -4.6RTpH_{PZC}$, Eq. (64b)) is included for limiting (not extreme) pH_{PZC}.

Due to variable experimental methods, there is a very large scatter of points of zero charge (pH_{pzc}) found for metal oxides. Different raw materials (crystal habits), as well as processing and precipitation conditions a clear differentiation between the oxy- and hydroxyl complexes cannot be made. Experimental points of zero charge for compounds involved in hydrogen bonds, such as metal oxo-hydroxides and metal hydroxides are expected to be lower than calculated ones [31]. This is not obvious from Table 9. It might be expected that heat treatment of some oxides would result in superficial loss of oxygen resulting in non-stoichiometry. This effect is not probable and can equally well be explained by assuming that oxygen vacancies and *n*-type of semiconductivity would exhibit a more basic pH_{PZC} than predicted for the stoichiometric oxide, owing to stabilization of adsorbed protons by mobile electrons. Similarly, *p*-type semiconductors might be expected to exhibit a more acidic pH_{PZC} than predicted due to proton repulsion or stabilization of adsorbed hydroxyls. As compared to previous interaction energies, proton association contributes only marginally to the overall energy balance in aqueous systems. In the theoretical modeling of proton association energy, very little attention was paid to the chemical contribution.

3.4. Potential determining cation and charge exchange

Metal (hydr)oxide surfaces may be both Lewis acids and Lewis bases and can catalyze oxidation as well as reduction reactions. Lewis acidity (electron acceptor) ability has been assigned to expose coordinately unsaturated metal (cat)ions. When dissolved as potential

Table 9
Points of zero charge limits of "dry" (hydroxide free) metal oxides as a function of metal valence reported by Parks [31] and also of metal (hydr)oxides listed in Appendix 6 (A-low < pH_{PZC} < A-high, extreme values in parenthesis). Molar Gibbs free energy of intrinsic proton association ($\Delta_{PZC}G_m$, kJ/mol Eq. (64b)) is given only for limiting (not extreme) pH_{PZC} values.

		P-low	$\Delta_{PZC}G_m$	P-high	$\Delta_{PZC}G_m$	A6-low	$\Delta_{PZC}G_m$	A6-high	$\Delta_{PZC}G_m$
z = 1	M_2O	11.5	-131			11	-126		
z = 2	$M(OH)_2$					(7) 8	-91.3	12 (14)	-137
z = 2	MO	8.5	-97.0	12.5	-143	(6,7) 9	-103	12	-137
z = 2.7	M_3O_4					7	-79.9	11	-126
z = 3	$M(OH)_3$					5	-57.1	10	-114
z = 3	MO(OH)					7	-79.9	10	-114
z = 3	M_2O_3	6.5	-74.2	10.4	-119	7	-79.9	10	-114
z = 4	MO_2	0	0	7.5	-85.6	(2,3) 4	-45.7	9 (11)	-103
z = 5	M_2O_5			0.5	-5.71	1	-11.4	5	-57.1
z = 6	MO_3			0.5	-5.71	0	0	2	-22.8

determining cations they leave behind excess electrons at the solid surface. This extreme Lewis activity corresponds to cation oxidation. Cations react with water and may readsorb to charged surface sites and become reduced back to metals. The latter process corresponds to reversed cation solvation. Fig. 22 illustrates each step of the thermodynamic cycle for metal cations.

Since the metal is in its standard state at 298.15 K and 1 bar, the sublimation of solid metal to dilute vapor (gas) may be denoted formation process ($\Delta_{fo}D_m^{\theta}(M^o,g) = \Delta_{sub}D_m(M^o,s)$). In the next process step metal is oxidized to produce ionized cations ($\Delta_{ox}D_m(M^o,g) = \Delta_{ion}D_m(M^{z+},s)$). The formation of ionized, gaseous cations equals the sum of sublimation and ionization ($\Delta_{fo}D_m^{\theta}(M^o,g) = \Delta_{sub}D_m(M^o,s) + \Delta_{ion}D_m(M^{z+},g)$). The gaseous cations are then transferred into infinitely dilute water solution. This hydration of cations ($\Delta_{hyd}D_m(M^{z+},g) = \Delta_{hyd}D_m(M_{aq}{}^{z+})$) is not directly related to any standard state. The thermodynamic cycle is closed when hydrated cations are reduced ($\Delta_{red}D_m^{\theta}(M^{z+},aq)$) back to metal species. This process step corresponds to reversed solvation of metal cations to infinite dilute aqueous solutions ($\Delta_{sol}D_m^{\theta}(M^o,s) = -\Delta_{red}D_m^{\theta}(M^{z+},aq)$), for which unit concentration (molality, molarity or mole fraction) represent the hypothetical standard state at 298.15 K and 1 bar [8].

The reduction of metal oxides creates an associated thermochemical cycle: Jointly with oxygen (O_2, g, Fig. 1) metal atoms form metal oxides ($\Delta_{fo}D_m^{\theta}$). Solid metal (hydr)oxides are dissolved in acidic and/or alkaline (basic) solutions ($\Delta_{dis}D_m^{\theta}$) to produce hydrated cations diluted in aqueous solutions. These cations are reduced ($\Delta_{red}D_m^{\theta}(M^{z+},aq)$) back to metals at their standard state. Standard reduction potentials of this incompletely defined process for metal hydroxides and metal oxohydroxides, are quoted in parallel to standard reduction potentials for metal cations. The reduction energy of such metal (hydr)oxide species is, however self-evidently different from reduction energy of hydrated cations ($\Delta_{red}D_m^{\theta}(M_xO_y,M(OH)_y,s) \neq \Delta_{red}D_m^{\theta}(M^{z+},aq)$).

3.4.1. Redox energy exchange – ion solvation

Standard molar reduction (free) energies for metal cations are reported relative to standard hydrogen Pt-electrode (SHE) at 298.15 K and 1 bar as:

$$\Delta_{red}^{rel}D_m^{\theta}(M^{z+},aq) = -\Delta_{sol}^{rel}D_m^{\theta}\left(M_{aq}^{z+}\right) = -zFE_{red}^{\theta} \quad (71)$$

where $D_m^{\theta} = G_m^{\theta}$. Solvation energy is, however reported both as free energy and enthalpy ($D_m^{\theta} = G_m^{\theta}$, H_m^{θ}) [8]. Protons at SHE have, however been assigned an absolute reduction potential of $E_{red}^{\theta} = 4.44$ V ($\Delta_{red}^{abs}G_m^{\theta}(H_{aq}{}^{+}) = 428.4$ kJ/mol) [18], which allows molar standard reduction potentials to be given both as relative (Eq. (28c)) and absolute (Eq. (27b)) values.

$$\Delta_{red}^{abs}G_m^{\theta}\left(M_{aq}^{z+}\right) = \Delta_{red}^{rel}G_m^{\theta}\left(M_{aq}^{z+}\right) + z\Delta_{red}^{abs}G_m^{\theta}\left(H_{aq}^{+}\right) = \Delta_{red}^{rel}G_m^{\theta}\left(M_{aq}^{z+}\right) + z428.4 \quad (72)$$

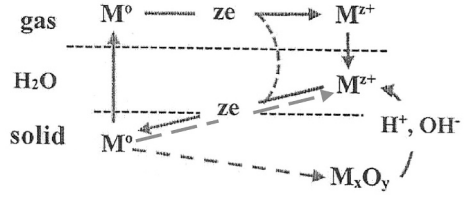

Fig. 22. Thermodynamic HBH cycle for metal species: Sublimation to neutral gaseous metals ($\Delta_{sub}D_m$), oxidation/ionization in gas phase ($\Delta_{ox}D_m = \Delta_{ion}D_m$), hydration ($\Delta_{hyd}D_m$) and reduction (full drawn line)/solvation (dashed line) ($\Delta_{red}D_m^{\theta} = -\Delta_{sol}D_m^{\theta}$) back to atomic metal. Jointly with oxygen (O_2, g, see Fig.1) metal atoms form metal oxide ($\Delta_{fo}D_m^{\theta}$), which may be dissolved ($\Delta_{dis}D_m^{\theta}$) in acidic or alkaline aqueous solutions (dotted line) to release cations which are reduced back to atomic metal.

When reduction potentials of metal (hydr)oxides are referred to, it should be stated whether acidic or alkaline (basic) aqueous solutions are considered.

Acidic solutions	*Alkaline (basic) solutions*
$M(OH)_z + ze^- + zH^+ \leftrightarrow M^o + zH_2O$	$M(OH)_z + ze^- \leftrightarrow M^o + zOH^-$
$MO_{z/2} + ze^- + zH^+ \leftrightarrow M^o + z/2H_2O$	$MO_{z/2} + ze^- + z/2H_2O \leftrightarrow M^o + zOH^-$
$M_xO_y + N_ee^- + N_eH^+ \leftrightarrow xM^o + N_e/2H_2O$	$M_xO_y + N_ee^- + N_e/2H^+ \leftrightarrow xM^o + N_eOH^-$

where $N_e = x|z+| = y|z-|$. In a few cases reduction energies are given for both acid and alkaline reactions. Such reactions are, for example:

$SnO_2 + 4e^- + 4H^+ \leftrightarrow Sn^o + 2H_2O$	$SnO_2 + 4e^- + 2H_2O \leftrightarrow Sn^o + 4OH^-$

Standard reduction potential in acidic aqueous solution is $E_{red}^{\theta} = -0.117$ V ($\Delta_{red}^{rel}G_m^{\theta} = 45.2$ kJ/mol) and in alkaline aqueous solution $E_{red}^{\theta} = -0.945$ V ($\Delta_{red}^{rel}G_m^{\theta} = 364.7$ kJ/mol) [8]. The corresponding standard absolute free energies are 428.8 and 346.7 kJ/mol, respectively. No standard reduction potential was found for tin cation in aqueous solution. Reduction of metal cation is characterized by rather different potential as compared to metal hydroxide:

$Al^{3+} + 3e^- \leftrightarrow Al^o$	$Al(OH)_3 + 3e^- \leftrightarrow Al^o + 3OH^-$

or metal oxide:

$Bi^{3+} + 3e^- \leftrightarrow Bi^o$	$Bi_2O_3 + 6e^- + 3H_2O \leftrightarrow 2Bi^o + 6OH^-$

The reduction potential of trivalent aluminium is $E_{red}^{\theta} = -1.662$ V ($\Delta_{red}^{rel}G_m^{\theta} = 481.1$ kJ/mol) and of $Al(OH)_3$ in alkaline aqueous solution $E_{red}^{\theta} = -2.31$ V ($\Delta_{red}^{rel}G_m^{\theta} = 668.6$ kJ/mol) [8]. The reduction potential of trivalent bismuth is $E_{red}^{\theta} = 0.308$ V ($\Delta_{red}^{rel}G_m^{\theta} = -89.1$ kJ/mol) and of Bi_2O_3 in alkaline aqueous solution $E_{red}^{\theta} = -0.46$ V (each cation, $E_{red}^{\theta} = -0.23$ V, $\Delta_{red}^{rel}G_m^{\theta} = 66.6$ kJ/mol) [8]. The acidic or basic (alkaline) process conditions are indicated in Table 3. It should be pointed out that successive redox processes of metal(cation)s are not additive [8]:

$Cu^+ + e^- \leftrightarrow Cu^o$	$E_{red}^{\theta} = 0.521\,V$	$Au^+ + e^- \leftrightarrow Au^o$	$E_{red}^{\theta} = 1.692\,V$
$Cu^{2+} + e^- \leftrightarrow Cu^+$	$E_{red}^{\theta} = 0.153\,V$	$Au^{3+} + 2e^- \leftrightarrow Au^+$	$E_{red}^{\theta} = 1.401\,V$
$Cu^{2+} + 2e^- \leftrightarrow Cu^o$	$E_{red}^{\theta} = 0.342\,V$	$Au^{3+} + 3e^- \leftrightarrow Au^o$	$E_{red}^{\theta} = 1.498\,V$

3.4.2. Cation hydration

Absolute hydration energies for metal cations may be derived indirectly from the thermodynamic cycle as:

$$\Delta_{hyd}^{abs}G_m\left(M_{aq}^{z+}\right) = -\Delta_{sub}^{abs}G_m(M^o,s) - \Delta_{ion}^{abs}G_m(M^o,g) + \Delta_{sol}^{abs}G_m^{\theta}(M^o,s) \quad (73)$$

Both sublimation and ionization energies are listed as absolute values. Relative standard reduction energies may also be converted to absolute values using absolute proton reduction potential 4.44 V ($\Delta_{red}^{abs}G_m^{\theta}(H_{aq}{}^{+}) = 428.4$ kJ/mol) [18] (Eq. (72)). Hydration free energies for cations are listed in Appendix 6.

The listed hydration energies are compared to previously published values [8,9]. Marcus [38] converted conventional (relative) hydration energies compiled by NBS to absolute values using $\Delta_{red}^{abs}G_m^{\theta}(H_{aq}{}^{+}) = -1056\,z$ kJ/mol. He corrected original data by adding a compression term due to transfer of ions from dilute gas (vacuum) to infinitely diluted aqueous solutions. Irrespective of ion charge the correction was found to be 7.93 kJ/mol [38]. More recently Kepp [18] evaluated Marcus and other published data and found it necessary to include surface potential of water 0.13 V to the SHE reduction potential. This overpotential arises due to non-alignment of water dipoles at Pt-electrode surface. He claimed a consensus value of $\Delta_{red}^{abs}G_m^{\theta}(H_{aq}{}^{+}) = -1100$ kJ/mol which corresponds to $E_{red}^{con}(H_{aq}{}^{+}) = 4.32$ V. Corrected for surface potential he arrived at the recommended $E_{red}^{\theta}(H_{aq}{}^{+}) = 4.44$ V. This value

corresponded to $\Delta_{red}{}^{abs}G_m{}^{\theta}(H_{aq}{}^{+}) = -1089$ kJ/mol, which is not far from the value $\Delta_{red}{}^{abs}G_m{}^{\theta}(H_{aq}{}^{+}) = -1056$ kJ/mol, used by Marcus. In his correction scheme of standard reduction (half) potentials of tri- and bivalent metal cations Kepp relied on subtraction of standard electrode potentials such as $E_{red}{}^{\theta}(M_{aq}{}^{3+}) - E_{red}{}^{\theta}(M_{aq}{}^{2+})$. The stepwise standard reduction potentials were, however previously shown to be non-additive. He did not report whether the compression correction of Marcus was removed or not. However, as shown in Appendix 6 the Gibbs hydration (free) energies arrived at through a normal thermochemical cycle without corrections agree closely with those reported by Kepp [18]. The reason may be that the compression correction introduced by Marcus (7.93 kJ/mol) and the overpotential introduced by Kepp 0.13 V $\Longleftrightarrow$ 12.5 kJ/mol) largely cancel each other. The contributing sublimation, ionization and solvation/reduction energies are plotted against hydration energy in Fig. 23.

Due to scale compression the scatter of relative energies appear greater. As expected $\Delta_{ion}G_m > \Delta_{sol}G_m > \Delta_{sub}G_m$. If relative reduction potential is used, sublimation and solution energies need to be converted to relative scale as:

$$\Delta_{sub}^{rel}G_m(M^o,s) = \Delta_{sub}^{abs}G_m(M^o,s) - z\,\Delta_{sub}^{abs}G_m(H^o,g) \tag{74a}$$

$$\Delta_{ion}^{rel}G_m(M^o,g) = \Delta_{ion}^{abs}G_m(M^o,g) - z\,\Delta_{ion}^{abs}G_m(H^o,g) \tag{74b}$$

where the values (CRC data [8]) used in present calculations were $\Delta_{sub}{}^{abs}G_m(H^o,g)$=203.3 kJ/mol and $\Delta_{ion}{}^{abs}G_m(H^o,g)$=1312,1 kJ/mol. Relative hydration energies for metal cations may then be derived indirectly from the thermodynamic cycle as:

$$\Delta_{hyd}^{rel}G_m\left(M_{aq}^{z+}\right) = -\Delta_{sub}^{rel}G_m(M^o,s) - \Delta_{ion}^{rel}G_m(M^o,g) + \Delta_{sol}^{rel}G_m^{\theta}(M^o,s) \tag{75}$$

These conventional (relative) hydration free energies for metal cations may be converted back to absolute values by adding $\Delta_{hyd}{}^{abs}G_m(H_{aq}{}^{+})$=– 1086.8 kJ/mol to relative values.

As shown in Appendix 6 the converted $\Delta_{hyd}{}^{rel}G_m(M_{aq}{}^{z+})$ values agree closely with those published [9] for univalent cations and [38] for bi- and trivalent cations. It should be realized, that in order to calculate relative (conventional) hydration values (Eq. (71)) using thermodynamic cycle (Eq. (73)), maintaining the aqueous standard reduction energy ($\Delta_{red}{}^{rel}G_m{}^{\theta}(M_{aq}{}^{z+})$) unchanged, the sublimation energy ($\Delta_{sub}G_m(M^o,s)$, Eq. (74a)) and the oxidation/ionization energy ($\Delta_{ox}G_m(M^o,g) = \Delta_{ion}G_m(M^o,g)$Eq. (64b)) have to be reduced by $z\,\Delta_{fo}G_m{}^{\theta}(H^o,g) = z/2\,\Delta_{dis}G_m(H_2,g)$ and $z\,\Delta_{ox}G_m(H^o,g) = z\,\Delta_{ion}G_m(H^o,g)$, respectively. Since the conventional values involve considerable reduction of physical processes it is questionable whether $\Delta_{hyd}{}^{rel}G_m(M_{aq}{}^{z+})$ represent any real physical state.

3.4.3. *Extended Born's hydration model*

Born developed models for absolute hydration/solvation energy change ($\Delta_{hyd}{}^{abs}D_m{}^{\theta}(M_{aq}{}^{z+})$) characterizing the process when isolated ions are transferred from vacuum (dilute gas) into solvent (water) continuum (Fig.1).

Model by Bockris and Reddy [40]: Born's model (Eq. (19a)) was previously used to calculate "solid formation" energies of metal oxides. Expressed for hydrated ions the standard molar Gibbs free energy becomes [40]:

$$\Delta_{hyd}^{abs}G_m = -\left(\frac{N_A}{4\pi\varepsilon_o}\right)\frac{(z_Me)^2}{2(r_M+2r_W)}\left(1-\frac{1}{\varepsilon_W}\right) \tag{76}$$

where permittivity is assumed to be $\varepsilon_W = 78.38$ and $d\varepsilon_W/dT < 0$ because of randomization of dipoles, quadrupoles and polarizabilities at increased temperature. Entropy is the negative partial derivative of free energy [40,41]:

$$\Delta_{hyd}^{abs}S_m = -\left(\frac{\partial\Delta_{hyd}^{abs}G_m}{\partial T}\right)_P = \left(\frac{N_A}{4\pi\varepsilon_o}\right)\frac{(z_Me)^2}{2(r_M+2r_W)}\left(\frac{1}{\varepsilon_W^2}\left(\frac{\partial\varepsilon_W}{\partial T}\right)\right) \tag{77}$$

Gibbs-Helmholtz equation may then be used to derive enthalpy of absolute hydration [40,41] as:

$$\begin{aligned}\Delta_{hyd}^{abs}H_m &= \Delta_{hyd}^{abs}G_m + T\Delta_{hyd}^{abs}S_m \\ &= -\left(\frac{N_A}{4\pi\varepsilon_o}\right)\frac{(z_Me)^2}{2(r_M+2r_W)}\left(1-\frac{1}{\varepsilon_W}-\frac{T}{\varepsilon_W^2}\left(\frac{\partial\varepsilon_W}{\partial T}\right)\right)\end{aligned} \tag{78}$$

The hydration energy resulting from Born charging can be improved by adding 0.85 Å to cation radius or 0.10 Å to anion radius [45]. When applying Born's model water is considered to be a dielectric continuum. In the primary hydration sheet water behaves rather as oriented dipoles. Introducing N_W as number of nearest neighbor water dipoles in primary hydration sheet of cations, we find [40] that:

$$\Delta_{dip}^{abs}H_m = -\left(\frac{N_A}{4\pi\varepsilon_o}\right)\frac{N_W(z_Me)p_W}{(r_M+r_W)^2} \tag{79}$$

where p_W represents dipole moment of water ($p_W = 6.216^{x}10^{-30}$ Cm). A closer examination of water molecules reveal that they consist of two negative electron clouds oriented opposite to two positive protons. This quadrupole interaction around cations may be accounted for [40] as:

$$\Delta_{qud}^{abs}H_m = \left(\frac{N_A}{4\pi\varepsilon_o}\right)\frac{N_W(z_Me)\,q_W}{2(r_M+r_W)^3} \tag{80}$$

where q_W represents quadrupole moment of water ($q_W = 1.9^{x}10^{-39}$ Cm^2). This quadrupole interaction is important, since it distinguishes between interaction with cations (positive sign) and anions (negative sign). The ion charge causes slight variations of electron distribution in water. This induced ion – induced dipole (polarizability) interaction is very weak and distance dependent [40]:

$$\Delta_{ind}^{abs}H_m = -\left(\frac{N_A}{4\pi\varepsilon_o}\right)\frac{N_W(z_Me)^2\,\alpha_W}{2(r_M+r_W)^4} \tag{81}$$

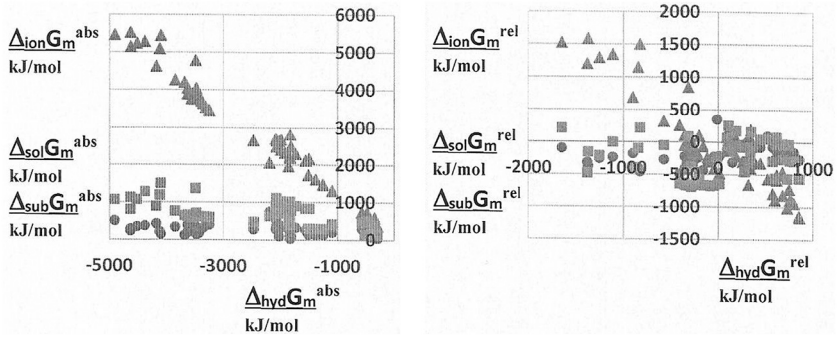

Fig. 23. Dependence of sublimation (circles, [8]), ionization (triangles, Eq. (16), [8]) and solution (squares, [8]) free energies on hydration free energy. Left diagram, absolute values. Right diagram, relative values. Data from Appendix 6.

where α_W represents deformation polarizability of water ($\alpha_W/4\pi\varepsilon_o$ = $1.48^{x}10^{-30}$ m^3). Born's model was further improved [40] by considering a constant (chemical) contribution for cavity formation ($\Delta_{cav}{}^{abs}H_m$) consisting of:

1. Creation of a primary solvation sheet (cluster formation) around bare ions. If cations surround themselves by $N_W = 4$ nearest neighbors in the tetrahedral primary hydration sheet 4 x 20.9 = 83.7 kJ/mol is consumed for dissociation of water from clusters in gas phase.
2. Twelve hydrogen bonds which are broken when water is removed to form a cavity for cations and ten water molecules which are reoriented around it. A net of two hydrogen bonds are broken during the combined process of cavity formation and structure breaking. Assuming that four water molecules are nearest neighbors in the primary hydration sheet this process consumes 2 ^{x} 20.9 = 41.8 kJ/mol.
3. Condensation of excess water molecules to bulk water which are not engaged in formation of primary solvent sheet absorbs 41.8 kJ/mol.

The total enthalpy balance of creating a primary hydration shell of tetrahedrally coordinated cations is $\Delta_{cav}{}^{abs}H_m \approx$ 83.7 – 41.8 + 41.8 = 83.7 kJ/mol. The total absolute hydration enthalpy is obviously the sum of these contributions:

$$\Delta^{abs}_{hyd}H_m = \Delta^{abs}_{Born}H_m + \Delta^{abs}_{dip}H_m + \Delta^{abs}_{qup}H_m + \Delta^{abs}_{ind}H_m + \Delta^{abs}_{cav}H_m \quad (82)$$

In Table 10 the contribution of each interaction to the total absolute hydration enthalpy is compared to experimental values.

Unfortunately no data on metal (hydr)oxides was available. No detailed information was provided [40] on dielectric constant (permittivity) of water inside ($6 < \varepsilon_r < 10$) and outside primary hydration shell used in calculations. Moreover, ion radii and absolute hydration enthalpy of protons vary depending on the source. Table 10 provides, however useful information of the compensation contribu-tions from ion – water interactions. For extensively hydrated cations (Li^+, Na^+), the absolute hydration enthalpies seem to be slightly too large as compared to experimental and reference values.

Model by Marcus [38]: Marcus distinguished water within primary hydration shell (*hs*) from bulk (*b*) water by a modified Born charging model:

$$\Delta^{hs}_{Born}G_m = \left(\frac{N_A}{4\pi\varepsilon_o}\right)\frac{N_W(z_M e)^2}{2r_M}\left(\frac{l^{hs}_M}{r_M + l^{hs}_M}\right)\left(1 - \frac{1}{\varepsilon^{hs}_W}\right) \quad (83)$$

where $r_{M=}$ ion radius (nm) and $l_M{}^{hs}$= thickness of hydration shell (nm). The dielectric constant within primary hydration shell expected to be $6 < \varepsilon_r < 10$ is defined as $\varepsilon_W{}^{hs} = n_D{}^2$, the squared index of refraction of D-line corresponding to non-polar interactions (Eqs. (34a),(36)), which are low in comparison to polar solvents. The coordination number of water was defined [38] as $N_W = 0.36 \cdot 10^{-9}(|z|/r_M)$. The influence of charging on bulk (*b*) water adjoining the hydration shell is given by:

$$\Delta^{b}_{Born}G_m = \left(\frac{N_A}{4\pi\varepsilon_o}\right)\frac{N_W(z_M e)^2}{2\left(r_M + l^{hs}_M\right)}\left(1 - \frac{1}{\varepsilon^{b}_W}\right) \quad (84)$$

For water at 25°C, the total Born charging effect was summarized [38] as:

$$\Delta^{abs}_{Born}G_m = \Delta^{hs}_{Born}G^{\theta}_m + \Delta^{b}_{Born}G_m = -28.4\left(\frac{z^2_M l^{hs}_M}{r_M\left(r_M + l^{hs}_M\right)}\right) - 63.7\left(\frac{z^2_M}{r_M + l^{hs}_M}\right) \quad (85)$$

The cavity is created by introducing ions uncharged into water. Assuming noble gas configuration the energy required was found [38] to be:

$$\Delta^{abs}_{cav}G_m = 41 - 87\left(r_M + l^{hs}_M\right) \quad (86)$$

The contribution of other ion effects on the structure of water is zero, since structured and bulk water are at equilibrium. A correction for the compression of ion space on transfer from gas to water (7.93 kJ/mol) is added to the energy balance irrespective of cation valence. In Table 11 absolute standard molar Gibbs free energies of hydration are compared to reference values.

No data on metal (hydr)oxides is available. For large cations an additional water orientation (quadrupole) contribution $\Delta_{Born}{}^{ori}G_m = 120\, r_M z_M{}^3$ must be added to $\Delta_{Born}{}^{abs}G_m$. This contribution distinguishes between cations and anions. Moreover, for bulky hydrocarbon cations an additional term ($1200 r_{HC}{}^2$) must be added to $\Delta_{cav}{}^{abs}G_m{}^{\theta}$. The Gibbs free energies listed in Table 11 are of same magnitude as the absolute enthalpies of hydration listed in Table 10 [40]. However, the contribution of Born electrostatic energy, as well as dipole, quadrupole van der Waals type induction energies differ substantially. Appendix 6 provides an extended list of absolute hydration energies of metal (hydr) oxides.

3.4.4. Summary

It is shown that cation reduction in acidic and alkaline solutions are characterized by different standard reduction potentials. Stepwise reduction potentials seem to be non-additive. The relative reduction free energy equals negative free energy of cation solvation. Hess-Born-Haber thermodynamic cycle characterizes successfully the dissolution and hydration of cations. The cycle encompass energy of sublimation, oxidation/ionization and solvation/ reduction of metals and their cations. Calculation of energy of cation hydration can be made both on absolute and relative (conventional) scales. There is some concerns whether relative (conventional) energies represent true physical states. Extensive and focused theoretical modeling of alkali cations result in nearly the same absolute Gibbs free energies and absolute enthalpies of

Table 11
Absolute standard Gibbs energies of hydration (kJ/mol) contributions: Born charging of hydration shell ($\Delta_{Born}G_m$), as well as of cavity formation ($\Delta_{cav}G_m$). The sum of these contributions ($\Delta_{hyd}G_m$) are compared to absolute hydration free energies ($\Delta_{ref}G_m$) = $\Delta_{hyd}{}^{ref}$ G_m) in reference [9,39]. Ion radii expressed in nm.

	r_M	l_M	N_W	$\Delta_{Born}G_m$	$\Delta_{cav}G_m$	$\Delta_{hyd}G_m$	$\Delta_{ref}G_m$
H^+	0.030	0.300	12	-1058	43	-1050	-1051
Li^+	0.069	0.172	5.2	-558	48	-510	-472.3
Na^+	0.102	0.116	3.5	-440	55	-385	-372.3
K^+	0.138	0.074	2.6	-372	67	-305	-300.0
Rb^+	0.149	0.064	2.4	-356	71	-285	-277.4
Cs^+	0.170	0.049	2.1	-328	83	-245	-245.1

Table 10
Absolute enthalpies of hydration (kJ/mol) contributions: Born charging, dipole, quadrupole, induced ion-dipole interactions and cavity formation [40]. The sum of these contributions are compared to experimentally determined and reference absolute hydration enthalpies. Ion radius r_M expressed in nm.

	r_M	$\Delta_{Born}H_m$	$\Delta_{dip}H_m$	$\Delta_{qup}H_m$	$\Delta_{ind}H_m$	$\Delta_{cav}H_m$	$\Delta_{hyd}H_m$	$\Delta_{exp}H_m$	$\Delta_{ref}H_m$
Li^+	0.060	-207.5	-546.0	290.8	-261.1	83.7	-640.1	-542.7	-514.7
Na^+	0.095	-188.3	-394.1	178.2	-136.8	83.7	-457.3	-428.0	-405.5
K^+	0.133	-170.7	-291.6	113.4	-80.3	83.7	-345.6	-348.5	-320.9
Rb^+	0.148	-164.4	-261.9	96.6	-61.1	83.7	-307.1	-323.0	-296.2
Cs^+	0.169	-156.9	-227.2	78.2	-43.9	83.7	-266.1	-298.7	-263.0

hydration. However, the contribution of Born electrostatic energy, as well as dipole, quadrupole van der Waals type induction energies differ substantially. This suggests that the contribution from absolute entropy of hydration is small and relatively constant. As expected, cation interactions are characterized by larger Gibbs free energies as compared to energies related to proton exchange. Very little attention is paid on chemical contribution to hydration energy.

3.5. Surface interaction energy – DLVO model

We have now collected all information needed to evaluate the interaction between two planar solids in aqueous solutions (Fig.24). Since we exclude external addititives (added anions and cations), we assume initially that sufficient ions dissolve from the solid to form a thermally distributed ion diffuse ion layer close to the solid surface planes. There is a decreased degree of freedom and attraction to the surface as well as mutual molecular repulsion close to surfaces. The excess ion concentration decreases exponentially when moving from the surface until a bulk value is attained. This (infinite) limit is chosen as reference point where both the potential and potential gradient become zero.

When the two surface planes illustrated in Fig. 24 are brought closer to each other the average ion concentration increases, resulting in an osmotic repulsive pressure aiming at diluting the electrolyte with surrounding solvent. We assume a symmetric distribution of ions and choose the midpoint between planes as reference point. The repulsive force created between planes due to the approach can be expressed with reference to the osmotic pressures at midpoint and at surface [21,42]. Assuming further that the potential at midpoint is low due to small overlap of diffuse layers remote from surfaces we can express the repulsive force (Deryagin disjoining pressure, [21,42]) as:

$$F_R = P_{1/2} - P_o \approx c_{xy}RT\left(\frac{zF\psi_{1/2}}{RT}\right)^2 \approx 64c_{xy}RT\Psi_o^2\, e^{-l_{ss}/(1/\kappa_d)} \tag{87}$$

where Ψ_o (no unit) is the complex surface potential and $(1/\kappa_d)$ is the reference thickness (l_D, Debye length) of the diffuse ion layer:

$$l_D = \frac{1}{\kappa_d} = \sqrt{\frac{\varepsilon_o\varepsilon_r RT}{F^2 c_{xy}\Sigma_i \nu_i z_i^2}} \quad \Leftrightarrow \quad l_D^{25} = 1.3597\sqrt{\frac{1}{c_{xy}\Sigma_i \nu_i z_i^2}} \tag{88}$$

where $\nu(c_{xy}) = x{+}y$, number of ions from molecule and z = valence (charge number). Examples of Debye length for symmetric and asymmetric aqueous electrolyte solutions at 25°C are presented in Table 12.

Potential interaction energy is obtained by integration of Eq. (87) as:

$$\Delta_{el}^{rep}D^s = \frac{64c_{xy}RT\Psi_o^2}{\kappa_d}\, e^{-l_{ss}/(1/\kappa_d)} \tag{89}$$

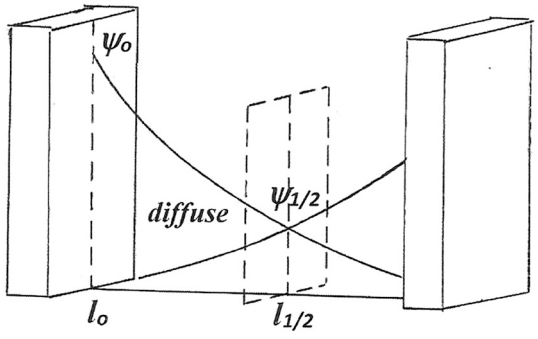

Fig. 24. Schematic illustration of potential drop between two parallel charged blocks due to the presence of electrolyte. The surface charge densities of each parallel plate are equal but of opposite sign. The remote (dashed) mid-plane is a fictive mirror reference.

with the unit mJ/m^2. A quantitative model for the net interaction between two planes is provided by Deryagin-Landau-Verwey-Overbeek model for ion distribution near solid planes. DLVO model combines attractive energy (Eq. (36) and repulsive energy (Eq. (89) [21,28,42] as:

$$\Delta_{DLVO}D^s = \Delta_{vrW}^{attr}D^s + \Delta_{el}^{rep}D^s = -\frac{A_{SWS}}{12\pi l_{SS}^2} + \frac{64c_{xy}RT\Psi_o^2}{\kappa_d}\, e^{-l_{SS}/(1/\kappa_d)} \tag{90}$$

with the unit mJ/m^2. Hamaker constant (A_{SWS}), distance between planes (l_{SS}), electrolyte concentration and valence (z), as well as complex surface potential (Ψ_o), determine the overall interaction. Attraction energy (Eq. (36)), which was introduced previously decays faster (approaching $1/{l_{SS}}^7$ dependence) when moving far away (lss > 100 nm) from the equilibrium molecular distance. This is denoted retardation effect and ${\Delta_{vdW}}^{attr}G^s$ retardation energy.

3.5.1. Surface charging – dependence on solution acidity

Surface charging results in thermally induced exponentially declining diffuse ion distribution near solid-liquid interfaces. Surface potentials cannot be determined on an absolute scale. Therefore, the inner (Galvani, ϕ) potentials of both solid and bulk liquid are set equal to zero (Fig. 25). When the external (Volta, ψ) potential, as well as its derivative ($d\psi/dl$) are also set equal to zero, the potential at solid-liquid interface is denoted surface potential (ψ_o). The potential at diffuse layer and its thickness is modeled by Deryagin-Landau-Verwey-Overbeek (DLVO) theory, which combines van der Waals attraction and electrostatic repulsion energies (Eq. (90)).

The potential decline with distance can be described by Gouy-Chapman complex surface potential (no unit) as:

$$\Psi = \Psi_o\, e^{-l_{SS}/(1/\kappa_d)} \quad \Leftrightarrow \quad \Psi = \frac{e^{zF\psi/2RT-1}}{e^{zF\psi/2RT}+1} \tag{91}$$

Two useful limits can be introduced. Expansion of Ψ_o (or Ψ) in series provides criteria for high surface potentials as:

$$\Psi_o = \frac{e^{zF\psi_o/2RT}-1}{e^{zF\psi_o/2RT}+1} \approx \frac{zF\psi_o}{4RT + zF\psi_o} \approx \frac{zF\psi_o}{zF\psi_o} \approx 1 \tag{92a}$$

where it is assumed that $4RT < zF\psi_o$. Exponent expansion of Ψ_o (or Ψ) in series provides criteria for low complex surface potentials as:

$$\Psi_o = \frac{e^{zF\psi_o/2RT}-1}{e^{zF\psi_o/2RT}+1} \approx \frac{zF\psi_o}{4RT + zF\psi_o} \approx \frac{zF\psi_o}{4RT} \tag{92b}$$

where it is assumed that, $zF\psi_o < 4RT$. Introducing the low potential approximation of both complex surface potentials into Eq. (91) we find Debye-Hückel approximation for potential dependence on distance from surface as:

$$\psi \approx \psi_o e^{-l_{SS}/(1/\kappa_d)} \tag{93a}$$

When Deryagin disjoining pressure (Eq. (87)) was derived it was assumed that the potential remote from solid surface is low ($\Psi \approx zF\psi/4RT$). Introduction into Eq. (91) results in:

$$\psi \approx \frac{4RT\Psi_o}{zF}\, e^{-l_{SS}/(1/\kappa_d)} \tag{94b}$$

If surface potential is very large ($\Psi_o \approx 1$) we find that:

$$\psi \approx \frac{4RT}{zF}\, e^{-l_{SS}/(1/\kappa_d)} \tag{94c}$$

In this case, the potential remote from solid surface is independent of surface potential. The volumetric charge density of diffuse layer is defined [27] as:

$$\sigma_d = -\sqrt{8\varepsilon_o\varepsilon_r c_{xy}kT}\sinh\left(\frac{zF\psi_o}{2RT}\right) = -0.1174\sqrt{c_{xy}}\sinh\left(\frac{zF\psi_o}{2RT}\right) \tag{95a}$$

The negative sign, $\sigma_o = -\sigma_d$ is due to electroneutrality requirement.

Table 12
Debye length (l_D/m, Eq. (88)) as a function of aqueous symmetric and asymmetric electrolyte concentrations ($c_{z:z}$/mol/dm^3) at 25°C [12,42].

c(z:z)	1:1	2:2	3:3	1:2	1:3	2:3
10^{-1}	$9{,}61^{x}10^{-10}$	$4.81^{x}10^{-10}$	$3.20^{x}10^{-10}$	$5.56^{x}10^{-10}$	$3.93^{x}10^{-10}$	$2.49^{x}10^{-10}$
10^{-2}	$3.04^{x}10^{-9}$	$1.52^{x}10^{-9}$	$1.01^{x}10^{-9}$	$1.76^{x}10^{-9}$	$1.24^{x}10^{-9}$	$0.79^{x}10^{-9}$
10^{-3}	$9{,}61^{x}10^{-9}$	$4.81^{x}10^{-9}$	$3.20^{x}10^{-9}$	$5.56^{x}10^{-9}$	$3.93^{x}10^{-9}$	$2.49^{x}10^{-9}$
10^{-4}	$3.04^{x}10^{-8}$	$1.52^{x}10^{-8}$	$1.01^{x}10^{-8}$	$1.76^{x}10^{-8}$	$1.24^{x}10^{-8}$	$0.79^{x}10^{-8}$
10^{-5}	$9{,}61^{x}10^{-8}$	$4.81^{x}10^{-8}$	$3.20^{x}10^{-8}$	$5.56^{x}10^{-8}$	$3.93^{x}10^{-8}$	$2.49^{x}10^{-8}$
10^{-6}	$3.04^{x}10^{-7}$	$1.52^{x}10^{-7}$	$1.01^{x}10^{-7}$	$1.76^{x}10^{-7}$	$1.24^{x}10^{-7}$	$0.79^{x}10^{-7}$
10^{-7}	$9{,}61^{x}10^{-7}$	$4.81^{x}10^{-7}$	$3.20^{x}10^{-7}$	$5.56^{x}10^{-7}$	$3.93^{x}10^{-7}$	$2.49^{x}10^{-7}$
10^{-8}	$3.04^{x}10^{-6}$	$1.52^{x}10^{-6}$	$1.01^{x}10^{-6}$	$1.76^{x}10^{-6}$	$1.24^{x}10^{-6}$	$0.79^{x}10^{-6}$
10^{-9}	$9{,}61^{x}10^{-6}$	$4.81^{x}10^{-6}$	$3.20^{x}10^{-6}$	$5.56^{x}10^{-6}$	$3.93^{x}10^{-6}$	$2.49^{x}10^{-6}$
10^{-10}	$3.04^{x}10^{-5}$	$1.52^{x}10^{-5}$	$1.01^{x}10^{-5}$	$1.76^{x}10^{-5}$	$1.24^{x}10^{-5}$	$0.79^{x}10^{-5}$
10^{-15}	$9{,}61^{x}10^{-3}$	$4.81^{x}10^{-3}$	$3.20^{x}10^{-3}$	$5.56^{x}10^{-3}$	$3.93^{x}10^{-3}$	$2.49^{x}10^{-3}$
10^{-20}	3.04	1.52	1.01	1.76	1.24	0.787
10^{-45}	$9{,}61^{x}10^{12}$	$4.81^{x}10^{12}$	$3.20^{x}10^{12}$	$5.56^{x}10^{12}$	$3.93^{x}10^{12}$	$2.49^{x}10^{12}$
10^{-70}	$3.04^{x}10^{25}$	$1.52^{x}10^{25}$	$1.01^{x}10^{25}$	$1.76^{x}10^{25}$	$1.24^{x}10^{25}$	$0.79^{x}10^{25}$

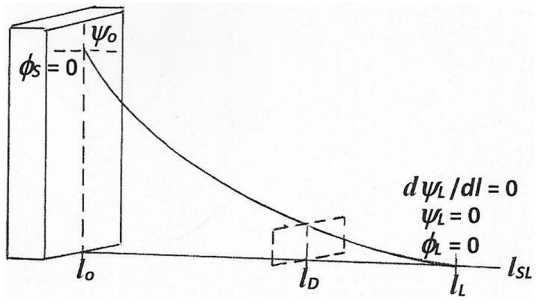

Fig. 25. Schematic illustration of potential drop due to a diffuse distribution of (cat)ions at a charged solid-liquid interface. The inner (Galvani, ϕ) potential of both solid and bulk liquid is set equal to zero. When the external (Volta, ψ) potential as well as its derivative ($d\psi/dl$) are also set equal to zero, the potential at solid-liquid interface is denoted surface potential (ψ_o).

Expansion in series leads to:

$$\sigma_o \approx \sqrt{8\varepsilon_o\varepsilon_r c_{xy}RT}\left(\frac{zF\psi_o}{2RT}\right) = \varepsilon_o\varepsilon_r\kappa_d\psi_o = \varepsilon_o\varepsilon_r\left(\frac{\psi_o}{l_D}\right) \quad (95b)$$

Nernst Eq. (51) enables determination of the relative surface potential using a reference concentration of protons (H^+) reducing surface potential to zero. The dependence of surface potential on point of zero charge (pH_{PZC}) was found (Eq. (53)) to be:

$$\psi_o = \frac{RT}{F}ln\left(\frac{[H^+]}{[H^+]_{PZC}}\right) = \frac{2.3RT}{F}(pH_{PZC} - pH) \quad (96a)$$

where 2.3 = ln10. Eq. (96a) may be expressed as changes in surface potential relative to logarithmic concentration as:

$$\frac{d\psi_o}{dpH} = -\frac{2.3RT}{F} \quad (96b)$$

At 25°C the expected slope slope is –59.16 mV (Table 13). This is an idealized reference behavior for real systems. The diffuse counterbalance charge density is obtained by inserting Eq. (95a) into Eq. (50) to obtain [27]:

$$\theta^d_{OH} = \frac{\sigma_d}{eN^s_{OH}} = \frac{0.1174\sqrt{c_{xy}}}{eN^s_{OH}}sinh\left(\frac{F\psi^*_o}{2RT}\right) \quad (97)$$

where relative (not measured) Nernst surface potential is denoted ψ_o*. Introducing $\tau = 2\sqrt{k^{int}_{a,1}/k^{int}_{a2}}$ or $\tau = 2\cdot 10^{pH_{PZC}} = 2\cdot 10^{pK_a int/2}$ into Eq. (97), we find the fraction of ionized surface sites [27] as:

$$\theta^{\#}_{OH} = \frac{\sigma_o}{eN^s_{OH}} = \frac{\tau sinh\left(\frac{F\psi^*_o}{RT} - \frac{F\psi^{\#}_o}{RT}\right)}{1 + \tau cosh\left(\frac{F\psi^*_o}{RT} - \frac{F\psi_o}{RT}\right)} \quad (98)$$

where calculated surface potential is denoted $\psi_o{}^{\#}$. Eqs. (97) and (98) contain all of the stoichiometric and thermodynamic constraints of diffuse ion distribution layer. The requirement of electrical neutrality ($\sigma_o + \sigma_d = 0$) and Eq. (95a), relating surface potential to diffuse layer charge density complete the mathematical description. Eqs. (97) and (98) can be solved graphically or numerically for unique values of surface charge density (σ_o) and surface potential (ψ_o) for any set of *pH*, electrolyte concentration (c_{xy}) and selected $N_{OH}{}^s$, $k_{a1}{}^{int}$ and $k_{a2}{}^{int}$ [27]. Table 13 lists the dependence of these parameters on *pH* when $pk_{a2}{}^{int} = 5.0$, $pk_{a1}{}^{int} = 7.0$, $pH_{PZC} = 6.0$, $\tau = 0.2$, $N_{OH}{}^s = 1.0\cdot 10^{18}$ sites/m^2, $c_{xy} = 10^{-2}$ mol/dm^3, $0.1174\sqrt{c_{xy}}/eN^s_{OH} = 7.342\cdot 10^{-2}$. Note that according to Table 6 $N_{OH}{}^s/10^{-18} \approx 14$ ($z = 1$), 12 ($z = 2$), 10 ($z = 3$), 8 ($z = 4$) sites/m^2.

The calculated surface potential ($\psi_o{}^{\#}$) decreases with increasing electrolyte concentration (c_{xy}) and it is always below experimental relative Nernst potential (ψ_o*), i.e. $0 < l\psi_o{}^{\#}l < l\psi_o{}^{*}l$. An increased difference between surface acidity constants ($\Delta pK_a{}^{int} = pk_{a2}{}^{int} - pk_{a1}{}^{int}$) enhances this surface potential difference. The rate of change of surface potential with *pH* ($d\psi_o/dpH$, Eq. (96b)), which should be 59.16 mV is smaller and variable (40 mV for SiO_2). The Nernst equation has been found to apply only when the surface charge density and surface potential are very small, or when the difference in partial acidity constants is very small. A small $\Delta pK_a{}^{int}$ implies that the fraction of ionized surface sites is large and fraction of neutral sites small.

Table 13
Surface charge density (σ_o, μC/cm^2) and surface potential (mV, Nernst $\psi_o{}^*$, calculated $\psi_o{}^{\#}$) dependence on *pH* for an ideal amphoteric solid with simple diffuse ion layer [27]. Details in text.

pH	ψ_o*	slope*	$\psi_o{}^{\#}$	Slope$^{\#}$	σ_o
4	+118.4		+87.4		+3.20
		-59.2		-42.4	
5	+59.2		+45.0		+1.28
		-59.2		-45.0	
6	0		0		0
		59.2		45.0	
7	-59.2		-45.0		-1.28
		59.2		42.4	
8	-118.4		-87.4		-3.20
		59.2		37.2	
9	-177.6		-124.6		-6.70

3.5.2. Surface charging – dependence on interlayer distance and on electrolyte concentration

As discussed, the repulsive force is based on the assumption that mid-point between planes (Fig.23) are far from surfaces and have a low potential. On the other hand, van der Waals forces decay to zero within a few nanometer from surfaces. It is therefore of great interest to find conditions where the distance between planes become equal for attractive van der Waals and repulsive electrostatic interactions. When plotting $\Delta_{DLVO}G^s$ as a function of inter-planar distance it goes from a deep minimum determined by $\Delta_{vdW}{}^{attr}G^s$, over a maximum interaction energy barrier to an exponential decay dominated by $\Delta_{el}{}^{rep}G^s$ at large distances. The critical distance separating dominance of attractive and repulsive forces, is given by the location of energy barrier maximum. Mathematically, this is found by requiring that both $\Delta_{DLVO}G^s = 0$ and $(d\Delta_{DLVO}G^s/dl_{ss}) = 0$. The first condition results in:

$$\frac{A_{SWS}}{12\pi l_{SS}^2} = \frac{64c_{xy}RT\Psi_o^2}{\kappa_d}e^{-l_{SS}/(1/\kappa_d)} = \frac{k_{el}}{\kappa_d}e^{-l_{SS}\kappa_d} \tag{99a}$$

The second condition is fulfilled when:

$$\frac{A_{SWS}}{6\pi l_{SS}^3} = k_{el}e^{-l_{SS}\kappa_d} = \frac{A_{SWS}\kappa_d}{12\pi l_{SS}^2} \quad \Leftrightarrow \quad l_{crit} = \frac{2}{\kappa_{crit}} \tag{99b}$$

This Schulze-Hardy model predicts that the critical interlayer distance equals twice Debye lengths at barrier maximum [21,28,42]. Gouy-Chapman theory allows for two limits for complex surface potential Ψ_o. For low potentials we found (Eq.92b)) that $\Psi_o \approx zF\psi_o/4RT$. Inserting this condition and $l_{crit} = 2/\kappa_d$ into Eq. (99a) we find that:

$$\frac{A_{SWS}\kappa_{crit}^2}{48\pi} = \frac{64c_{crit}RT}{\kappa_{crit}}\left(\frac{z^2F^2\psi_o^2}{16R^2T^2}\right)e^{-2} = 0.5413 \quad \frac{c_{crit}z^2F^2\psi_o^2}{\kappa_{crit}RT} \tag{100a}$$

We rewrite Eq. (100a) in terms of critical (inverse) Debye length as:

$$\kappa_{crit}^3 = 81.63 \quad \frac{c_{crit}z^2F^2\psi_o^2}{A_{SWS}RT} \quad \Leftrightarrow \quad l_{crit}^3 = \frac{8}{\kappa_{crit}^3} = 9.800{\cdot}10^{-2}\frac{A_{SWS}RT}{c_{crit}z^2F^2\psi_o^2} \tag{100b}$$

In order to make derivation of l_{crit} for low and high surface potentials compatible, we assume an average low range surface potential of $\psi_o = \pm$ 50mV (Table 13). At 25°C we may write Eq. (100b) as:

$$l_{crit}^3 = \frac{8}{\kappa_{crit}^3} = 9.800{\cdot}10^{-2}\frac{A_{SWS}RT}{c_{crit}z^2F^2\psi_o^2} \quad \Leftrightarrow \quad l_{crit}^{25} = 2.1854{\cdot}10^{-2}\sqrt[3]{\frac{A_{SWS}}{c_{crit}z^2}} \tag{100c}$$

Eq. (100a) may be rewritten in terms of critical concentration as:

$$c_{crit} = 1.225{\cdot}10^{-2}A_{SWS}\left(\frac{RT}{F^2}\right)\left(\frac{\kappa_{crit}^3}{z^2\psi_o^2}\right) = 3.2618{\cdot}10^{-9}\left(\frac{A_{SWS}}{z^2\psi_o^2}\right)\kappa_{crit}^3 \tag{101a}$$

Introducing inverse Debye length for symmetric electrolytes results in:

$$c_{crit} = 3.2618{\cdot}10^{-9}\left(\frac{A_{SWS}}{z^2\psi_o^2}\right)\left(\frac{2.8F^3}{\varepsilon_o^{3/2}\varepsilon_W^{3/2}R^{3/2}T^{3/2}}\right)c_{crit}^{3/2}z^3 = k_\kappa\left(\frac{A_{SWS}}{\psi_o^2}\right)c_{crit}^{3/2}z \tag{101b}$$

The critical concentration is thus proportional to inverse valence in second power ($c_{crit} \propto (1/z^2)$). The influence of electrolyte valence ($z = 1$, 2, 3. 4) on critical concentration scales as: 1, 1/4, 1/9, 1/16. Such dependence has been observed with experiments on colloids (nano-sized particles) [22,42,43].

Nernst equation enables determination of surface potential with reference to cation concentration when surface potential becomes zero. Since surface charging requires energy, it may be assumed that solubility product concentration (c_{sp}, Eq. (39b), Appendix 4) represents such limit. The surface potential (mV) changes from zero at c_{sp} (Eq. (96a)) as:

$$\psi_o = \frac{RT}{|z|F}ln\left(\frac{c_M}{c_{sp}}\right) = \frac{2.3RT}{|z|F}\left(pc_{sp} - pc_M\right) \tag{102a}$$

Eq. (102a) may be expressed as a change in surface potential as a function of logarithmic concentration (Eq(96b)) as:

$$\frac{d\psi_o}{dpc_M} = -\frac{2.3RT}{|z+|F} \quad \Leftrightarrow \quad \frac{d\psi_o}{dpH} = -\frac{2.3RT}{|z|F} \tag{102b}$$

With reference to point of zero charge (pH_{PZC}, Table 9), Table 14 lists the solubility product (pK_{sp}) and surface potential (ψ_o) dependence on solubility product concentration (pc_{sp}) and on cation valence (z_M).

In order to establish surface potential we need to extract c_{sp} from K_{sp}. As shown by Eq. (39b) $pc_{sp} = pK_{sp} - zpc_{OH} = pK_{sp} - z(14 - pH_{PZC})$. For multivalent metal hydroxides ($1 < z_M < 3$) only mid-range pK_{sp} and pH_{PZC} values are used. Table 14 shows that the high-end surface potentials are extreme as compared to values recorded in Table 13.

For high potentials we found (Eq. (92a))that $\Psi_o \approx 1$ (Eq. (92a)). Inserting this condition and $l_{crit} = 2/\kappa_d$ into Eq. (90) we find that:

$$\frac{A_{SWS}\kappa_{crit}^2}{48\pi} = \frac{64c_{crit}RT}{\kappa_{crit}}e^{-2} = 8.6615 \quad \frac{c_{crit}RT}{\kappa_{crit}} \tag{103a}$$

We write Eq. (103a) in terms of critical inverse Debye length as:

$$\kappa_{crit}^3 = 1306\frac{c_{crit}RT}{A_{SWS}} \quad \Leftrightarrow \quad l_{crit}^3 = \frac{8}{\kappa_{crit}^3} = 6.125{\cdot}10^{-3}\frac{A_{SWS}}{c_{crit}RT} \tag{103b}$$

Considering 25°C we may write Eq. (103b) as:

$$l_{crit}^3 = \frac{8}{\kappa_{crit}^3} = 2.471{\cdot}10^{-6}\frac{A_{SWS}}{c_{crit}} \quad \Leftrightarrow \quad l_{crit}^{25} = 1.352{\cdot}10^{-2}\sqrt[3]{\frac{A_{SWS}}{c_{crit}}} \tag{103c}$$

Eq. (103a) may also be rewritten in terms of critical concentration as:

$$c_{crit} = 7.656{\cdot}10^{-4}\left(\frac{A_{SWS}}{RT}\right)\kappa_{crit}^3 = 3.089{\cdot}10^{-7}A_{SWS}\kappa_{crit}^3 \tag{104a}$$

For symmetric electrolytes insertion of inverse Debye length results in:

$$c_{crit} = 3.089{\cdot}10^{-7}A_{SWS}\kappa_{crit}^3 = k_\kappa A_{SWS}c_{crit}^{3/2}z^3 \tag{104b}$$

The critical concentration is thus proportional to inverse valence in sixt power ($c_{crit} \propto (1/z^6)$). The influence of electrolyte valence ($z = 1$, 2, 3. 4) on critical concentration scales as: 1, 1/64, 1/729, 1/4096. Such dependence has been observed with experiments on colloids (nano-sized particles) [22,42,43].

The parameters chosen to evaluate critical (Debye) length is based on data in Table 5, where Hamaker constants were found to be: $19 < A/zJ < 34$ (MO), $36 < A/zJ < 46$ (M_2O_3) and (8-17) $60 < A/zJ < 130$ (MO_2). Since Hamaker constant is expected to have a small influence on l_{crit}, only limits 20 zJ and 120 zJ were chosen. The electrolyte concentration in absence of additives may be extracted from the solubility product. In Table 14 it was found on the average for M(OH)$_z$ that: $7 < pK_{sp} < 14$ ($z = 1$), $10 < pK_{sp} < 20$ ($z = 2$), $20 < pK_{sp} < 45$ ($z = 3$) and $45 < pK_{sp} < 65$ ($z = 4$). The limits are somewhat larger for $MO_l(OH)_k$. The electrolyte

Table 14
Dependence of solubility product (pK_{sp}, Appendix 4), point of zero charge (pH_{PZC}, Table 9, Appendix 5) and surface potential (ψ_o, Eq. (102a)) and its slope ($d\psi_o/dpc_{sp}$, Eq. (102b))) on cation valence ($1 < z_M < 3$, Eq. (102a), low < c_{sp} < high, extreme values are disregarded). Cation concentration pc_{sp} , Eq. (38) and $pc_M = 0$)

z_M	M(OH)$_z$	low	high	slope	pH_{low}	pH_{high}	ψ_{low}	ψ_{high}
$z_M = 1$	M(OH)	7	14	59.2	11		237	
$z_M = 2$	$M(OH)_2$	10	20	29.6	8	12	-59.2	473
$z_M = 3$	$M(OH)_3$	20	45	19.7	5	10	-138	651
$z_M = 4$	$M(OH)_4$	45	65	14.8				
$z_M = 4$	$MO(OH)_2$	30	50	14.8				
$z_M = 6$	$M(OH)_6$		20	9.86				

Table 5
Average published (experimental) solid-gas-solid (A_{SGS}^{exp}, Eq. (33)), solid-water-solid (A_{SWS}^{exp}, Eq. (36)) [21,22] and calculated (A_{SWS}^{calc}, Eq. (37)) Hamaker constants (zJ = 10^{-21} J). Molar experimental solid-gas-solid ($A_{SGm}^{exp} = N_A{}^xA_{SGS}$), solid-water-solid ($A_{SWm}^{exp=} N_A{}^xA_{SWS}$) and calculated ($A_{SWm}^{calc}$) Hamaker energies (kJ/mol). f-SiO_2= fused quartz, c-SiO_2= crystalline quartz, r-TiO_2= rutile, dia-C = diamant, av = average (Table 4). Hamaker constant of water, A_{WGW} = 53.26 zJ.

Subst	A_{SGS}^{exp}	A_{SGm}^{exp}	A_{SWS}^{exp}	A_{SWm}^{exp}	A_{SWS}^{calc}	A_{SWm}^{calc}
BeO	147	88.3	33.9	20.4	23.2	13.9
MgO	115	69.0	20.2	12.2	11.6	6.99
ZnO	93.0	56.0	19.1	11.5	5.51	3.32
Al_2O_3	140	84.3	42.0	25.3	20.6	12.4
α-Al_2O_3	158	95.3	45.6	27.5	27.9	16.8
Y_2O_3	133	80.1	35.5	21.4	17.9	10.8
Fe_3O_4	210	126			5.17	31.2
f-SiO_2	65.0	39.2	8.33	5.02	5.84	0,35
f-SiO_2	65.9	39.7	8.60	5.18	6.68	0,40
c-SiO_2	88.3	53.2	17.0	10.2	4.40	2.65
c-SiO_2	89.7	54.0	10.3	6.22	4.73	2,85
r-TiO_2	154	92.7	58.4	35.2	26.1	15.7
av-TiO_2	249	150			71.9	43.3
r-TiO_2	430	259	260	157	181	109
ZrO_2	202	122	88.9	53.5	47.9	28.8
av-ZrO_2	236	142			65.0	39.2
ZrO_2	270	163	130	78.3	83.4	50.2
dia-C	293	177	138	82.9	96.6	58.2
Ti	253	152	131	79.1	74.0	44.5
Au	473	285	313	188	209	126
LiF	64.2	38.7	3.17	1.91	0.51	0.31
NaF	41.0	24.7	3.13	1.88	0.81	0.49
NaCl	65.5	39.4	5.62	3.38	0.63	0.38
KCl	59.1	35.6	3.64	2.19	0.15	0.09
KBr	62.4	37.6	6.06	3.65	0.36	0.22
CsI	81.1	48.8	12.1	7.31	2.91	1.75
MgF_2	59.3	35.7	3.75	2.26	0.16	0.10
CaF_2	70.4	42.4	4.44	2.68	1.19	0.72

range was chosen to cover the high $10^{-1} < c_{xy}/(mol/dm^3) < 10^{-5}$ and the low $10^{-10} < c_{xy}/(mol/dm^3) < 10^{-70}$ ranges. Table 15 lists l_{crit} calculated using Eq. (100c) for low surface potentials and Eq. (103c) for high surface potentials.

The critical length for symmetric and asymmetric electrolytes (Table 15) is compared to Debye length (Table 12) in Fig. 26.

The electrolyte concentrations, c_{xy} /mol/dm^3 were selected from Table 15: 10^{-1}, 10^{-2}, 10^{-3}, 10^{-4}, 10^{-5}, 10^{-10}, 10^{-15}, 10^{-20}, 10^{-35}, 10^{-70} and from Table 12: 10^{-1}, 10^{-2}, 10^{-3}, 10^{-4}, 10^{-5}, 10^{-7}, 10^{-15}, 10^{-20}, 10^{-45}, 10^{-70}. All curves are almost coincident at the high concentration $10^{-1} < c_{xy}/(mol/dm^3) < 10^{-5}$ limit. The order of experimental points at 10^{-1} mol/dm^3 from small negative logl_{crit} (nm-range) to large negative logl_{crit} (Å-range)) with reference to Table 12 (z:z) and to Table 15 (A:z) were: 120,1 (patterned diamond); 120 (filled square); 20,1 (filled diamond); 1:1 (open circle); 120,5 (open diamond); 20 (filled circle); 1:2 (patterned triangle); 2:2 (shaded circle); 20,5 (shaded diamond); 1:3 (shaded triangle); 3:3 (filled circle); 2:3 (open triangle). As a summary, a large l_{crit} (small negative log l_{crit}) is supported by a large Hamaker constant, small (symmetric) valence and a small electrolyte concentration. Note that l_{crit} and l_D are in the Ångström (10^{-10} m) – nanometer (10^{-9} m) range when $0.1 < c_{xy}/mol/dm^3 < 1$. Within these limits van der Waals attraction forces and hydration forces become significant. Debye lengths (l_D, Eq. (88)) grow faster than critical lengths (l_{crit}, Eqs.(100c), (103c)) when electrolyte concentration is reduced. At reduced electrolyte concentration, Hamaker constants and ion valence (z) have very small influence on l_D and l_{crit}. This is opposite to the prediction that electrolyte valence should scale c_{crit} as: 1 (z = 1), 1/4 (z = 2), 1/6 (z = 3) for low surface potentials (Eq. (100b)) and as: 1 (z = 1), 1/64 (z = 2), 1/729 (z = 3) for high surface potentials (Eq. (103b)). This scaled dependence has been confirmed for corresponding Schultze-Hardy analysis of colloid 13.8 nm TiO_2 particle suspensions. The critical distance dependence was found to range as: $0.88 < l_{crit}/nm < 8.0$ [43]. Cubic and random close packing of these particles resulted in $7.5 < l_{SS}/nm < 8.5$ nm. It should, however be kept in mind, that although the force (Deryagin disjoining pressure, Eq. (87)) may apply, the repulsive interaction energy may not [21,42] which would invalidate Schulze-Hardy model. Moreover, in particular high valent dissolved counterions tend to adsorb specifically (chemically) to the surface sites, which must be accounted for in expressions for surface charge densities. The electrostatic modeling of double or triple layers is discussed in the next chapter.

3.5.3. Summary

Although, both l_{crit} and c_{crit} provided by DLVO model are useful results, there is not any quantitative energy data for comparison with previous energy contributions. Model calculations of $\Delta_{DLVO}D$ (Eq. (90)) dependence on interlayer distance l_{SS} (nm) [42] may, however be used for this purpose. The potential energy when two blocks of 4.0 nm^2 area approach each other (Fig. 24) in 0.093 mol/dm^3 1:1 electrolyte solution (l_D = 1 nm, Table 14) was expressed as a function of interlayer distance in two ways: 1) The surface potential is kept constant (ψ_o = 103 mV) and A_{SWS}/zJ = 20, 50, 100 and 200. 2) The Hamaker constant is kept constant (A_{SWS} = 200 zJ) and ψ_o/mV = 103, 159, 180, 206 and 257. Since the interaction area is known, the interaction energy can easily be converted to mJ/m^2. When potential energy is multipled by Avogadros number, the energy may be expressed as kJ/mol, which may be compared to previous "bulk" energies. Eq. (35) enables determination calculation of van der Waals attraction energy at interaction maximum and this may be converted to other energy scales as described. Finally, Eq. (90) shows that the electrostatic repulsion energy is simply the sum of total and attraction energy. These maximum energy contributions are collected in Table 16 as a function of interlayer distance.

Note the difference between Hamaker energy (A_{SWm}/kJ/mol) and van der Waals energy ($\Delta_{vdW}D_m$/kJ/mol, Eq. (35)) arising from contact area structure constraints. The "bulk" interaction energies extracted from Table 16 are plotted against interaction maximum location distance in Fig. 27.

Unfortunately, the energy and location (l_{max}) of maximum attractive

Table 15
Critical length (m) between two planes in aqueous electrolyte solutions ($c_{xy}/(mol/dm^3)$, $1 < z_M < 5$) at 25°C. High surface potential limit values are calculated using Eq. (103c, two first l_{crit} columns) and low surface potential limit values using Eq. (100c, ψ_o = 50 mV). In order to reduce space: A_{SLS}/zJ = 20, 120, z_M = 1, 2, 3, 5 and c_{xy} = 10^{-1}, 10^{-2}, 10^{-3}, 10^{-4}, 10^{-5}, 10^{-10}, 10^{-15}, 10^{-20}, 10^{-35}, 10^{-70}. Note short hand writing, $xy^z = xy\ {}^x10^z$.

c_{xy} \ A,z_M	20	120	20,1	120,1	20,2	120,2	20,3	120,3	20,5	120,5
10^{-1}	7.91^{-10}	1.44^{-9}	1.28^{-9}	2.32^{-9}	8.05^{-10}	1.46^{-9}	6.14^{-10}	1.12^{-9}	4.37^{-10}	7.94^{-10}
10^{-2}	1.70^{-9}	3.09^{-9}	2.75^{-9}	5.00^{-9}	1.73^{-9}	3.15^{-9}	1.32^{-9}	2.40^{-9}	9.42^{-10}	1.71^{-9}
10^{-3}	3.67^{-9}	6.67^{-9}	5.93^{-9}	1.08^{-8}	5.93^{-9}	6.79^{-9}	2.85^{-9}	5.18^{-9}	2.03^{-9}	3.69^{-9}
10^{-4}	7.91^{-9}	1.44^{-8}	1.28^{-8}	2.32^{-8}	8.05^{-9}	1.46^{-8}	6.14^{-9}	1.12^{-8}	4.37^{-9}	7.94^{-9}
10^{-5}	1.70^{-8}	3.09^{-8}	2.75^{-8}	5.00^{-8}	1.73^{-8}	3.15^{-8}	1.32^{-8}	2.40^{-8}	9.42^{-9}	1.71^{-8}
10^{-10}	7.91^{-7}	1.44^{-6}	1.28^{-6}	2.32^{-6}	8.05^{-7}	1.46^{-6}	6.14^{-7}	1.12^{-6}	4.37^{-7}	7.94^{-7}
10^{-15}	3.67^{-5}	6.67^{-5}	5.93^{-5}	1.08^{-4}	5.93^{-5}	6.79^{-5}	2.85^{-5}	5.18^{-5}	2.03^{-5}	3.69^{-5}
10^{-20}	1.70^{-3}	3.09^{-3}	2.75^{-3}	5.00^{-3}	1.73^{-3}	3.15^{-3}	1.32^{-3}	2.40^{-3}	9.42^{-4}	1.71^{-3}
10^{-35}	1.70^{2}	3.09^{2}	2.75^{2}	5.00^{2}	1.73^{2}	3.15^{2}	1.32^{2}	2.40^{2}	9.42^{1}	1.71^{2}
10^{-70}	7.91^{13}	1.44^{14}	1.28^{14}	2.32^{14}	8.05^{13}	1.46^{14}	6.14^{13}	1.12^{14}	4.37^{13}	7.94^{13}

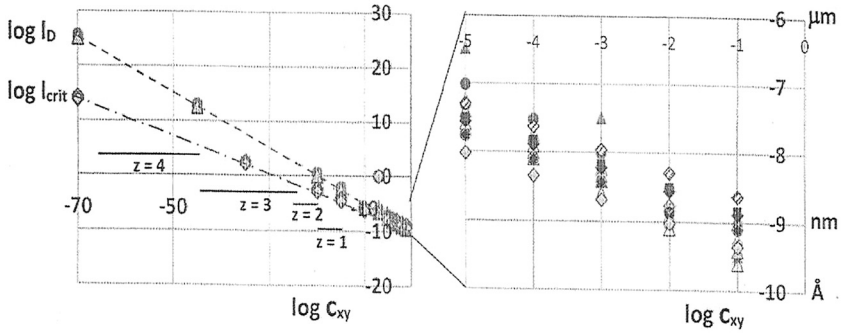

Fig. 26. Logarithmic critical length (m, log l_{crit} , Eqs.(100c) diamonds,(103c) squares, Table 15) and Debye length (m, log l_D, Eq. (88), (Table 12) of symmetric (circles) and asymmetric (triangles) electro-lytes plotted against logarithmic concentration (mol/dm^3, log c_{xy}, $1 < z < 5$) at 25°C. Right diagram is an enlargement of $10^{-10} <$ log l/m $< 10^{-6}$ range. The solubility ranges of $M(OH)_z$ are indicated. Consult text for details.

Table 16
DLVO theory prediction (Eq. (90)) of maximum total, attractive (van der Waals) and repulsive interaction energy as a function of Hamaker (A_{SWS}/zJ) constant and of surface potential (ψ_o/mV) when two similar blocks approach each other in 0.093 mol/dm$_3$ 1:1 electrolyte solution (l_D = 1 nm). The parameters held constant are indicated – * measured at break point (uncertain).

ψ_o=103mV	l_D = 1nm	A = 4.0nm^2	T = 298K		
A_{SWS}/zJ	20	50	100	200	
A_{SWm}/kJ/mol	12.05	30.11	60.23	120.5	
l_{max}/nm	0.49	0.86	1.47	2.85*	
$\Delta_{DLVO}D_{max}$/zJ	12.87	6.29	1.80	-0.84*	
$\Delta_{vdW}D_{max}$/zJ	8.65	7.16	4.97	2.60	
$\Delta_{el}D_{max}$/zJ	21.51	13.45	6.77	1.76	
$\Delta_{DLVO}D^s_{max}$/mJ/m^2	3.22	1.57	0.45	-0.21*	
$\Delta_{vdW}D^s_{max}$/mJ/m^2	2.16	1.79	1.24	0.65	
$\Delta_{el}D^s_{max}$/mJ/m^2	5.38	3.36	1.69	0.44	
$\Delta_{DLVO}D_{m,max}$/kJ/mol	7.75	3.79	1.09	-0.51*	
$\Delta_{vdW}D_{m,max}$/kJ/mol	5.21	4.31	2.99	1.57	
$\Delta_{el}D_{m,max}$/kJ/mol	12.95	8.10	4.08	1.06	
A_{SWS}=200zJ	l_D =1nm	A=4.0nm^2	T=298K		
ψ_o/mV	257	206	180	159	103
l_{max}/nm	1.15	1.37	1.60	2.00	2.96*
$\Delta_{DLVO}D_{max}$/zJ	2.64	1.65	1.04	0,35	-0.79*
$\Delta_{vdW}D_{max}$/zJ	15.98	11.16	8.32	5.32	2.43
$\Delta_{el}D_{max}$/zJ	18.62	12.81	9.35	5.66	1.64
$\Delta_{DLVO}D^s_{max}$/ mJ/m^2	0.66	0.41	0.26	0.09	-0.20*
$\Delta_{vdW}D^s_{max}$/mJ/m^2	4.00	2.77	2.08	1.33	0.61
$\Delta_{el}D^s_{max}$/mJ/m^2	4.66	3.20	2.34	1.42	0.41
$\Delta_{DLVO}D_{m,max}$/kJ/mol	1.59	1.00	0.62	0.21	-0.47*
$\Delta_{vdW}D_{m,max}$/kJ/mol	9.62	6.72	5.01	3.20	1.46
$\Delta_{el}D_{m,max}$/kJ/mol	11.22	7.72	5.63	3.41	0.99

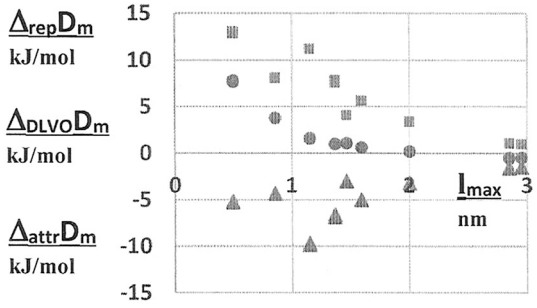

Fig. 27. Maximum total (circles), attractive (van der Waals, triangles) and repulsive (squares) potential energies predicted by DLVO theory (Eq. (90)) as a function of location of interaction maximum for two identical blocks approaching each other in 0.093 mol/dm^3 1:1 electrolyte solution at 25°C.

and repulsive interaction energy for the two simulations do not fully match for equal input data. For A_{SWS} = 200 zJ and ψ_o = 103 mV one simulation results in $D_{DLVO}D_{max}$ = -0.84 zJ at l_{max} =2.85 nm and the other simulation to $D_{DLVO}D_{max}$ = -0.79 zJ at l_{max} =2.96 nm (Table 16). The reason is that both values are measured at the break point when $D_{DLVO}D_{max}$ maximum had vanished. In order to evaluate the source for this discrepancy, the critical distance (l_{crit}) predicted for equal parameters by Schulze-Hardy model for low (Eq. (100c)) and high (Eq. (103c)) surface potentials are plotted against l_{max} in Fig. 28.

The l_{crit} location for constant low (Eq. (100c)) and high (Eq. (103c)) surface potentials for increasing Hamaker constants are superimposed. However, the l_{crit} location for constant Hamaker constant (A_{SWS}), but increasing low surface potentials (ψ_o, Eq. (100c)) do not fully agree with previous values. Neither sequence agree with l_{max} location of corresponding simulated $\Delta_{DLVO}D_{max}$ potential energy, as illustrated by the dotted unit slope line. The mismatch is caused by discrepancies of l_{max} location. Entered in Eq. (35) it gives diverging $\Delta_{attr}D_{max}$ and further $\Delta_{rep}D_{max}$ interaction energies. However, the simulated maximum $\Delta_{DLVO}D_{max}$ values remain unaffected and serve as quantified DLVO energies for comparison with previous "bulk" energies.

3.6. Surface solvation and specific cation adsorption

At the solid–liquid interface a range of exceptional phenomena are observed. The loss of one dimension of mobility freedom results in

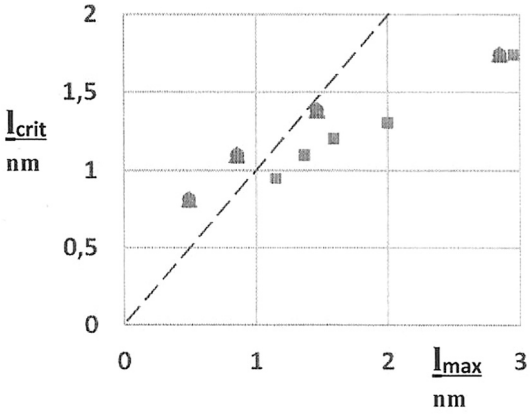

Fig. 28. The location of critical total potential energy predicted by Schultze-Hardy model (l_{crit}, nm) as a function of maximum distance predicted by DLVO theory (l_{max}, nm, Eq. (90)) for two identical blocks approaching each other in 0.093 mol/dm^3 1:1 electrolyte solution at 25°C. Symbols: Constant low surface potential (circles, Eq. (100c)), high potential (triangles, Eq. (103c)) and increasing Hamaker constant. Constant Hamaker constant and increasing surface potential (squares, Eq. (100c)). Dotted line = unit slope.

Kirkwood-Alder transitions to enhanced molecular packing even in the absence of attraction [44,45]. The enhanced surface packing is shown as fluctuation of van der Waals attraction force at molecularly smooth (mica) surfaces. For polar solvent molecules, such as water dipole and Lewis acid-base interaction results in an interfacial potential drop. Moreover, in the presence of specific adsorption of dissolved potential determining cations, the single layer diffuse ion distribution (DLVO) model must be exchanged for a double layer or even triple layer models.

3.6.1. Surface solvation forces

Any strong attractive interaction at solid-liquid interfaces leads to a denser packing of molecules at the walls. Any attraction results is an enhanced oscillatory van der Waals force (Fig.29). If the surface-liquid interaction is much weaker than the liquid-liquid interaction the oscillatory force tends to be more attractive (hydrophobic attraction). The structural interaction energy can, however be both negative (attraction) and positive (repulsion). The long-range attractive van der Waals force decays smoothly with distance from interfaces. Fig. 29 illustrates the interaction near a molecularly smooth surface.

As compared to macroscopic interactions, there is a narrow molecular pair interaction range where the macroscopic attractive energy does not fully apply. Confined to a solid surface the liquid loose one dimension of movement. Considering the periodic attraction in vicinity of solid-liquid interfaces the dimension of water molecules $d_W \approx 0.385$ nm ($d_W \approx 0.28$nm [38]) has to be accounted for. For Hamaker constants smaller than about 0.2 kT ($A_{SWS} < 0.8$ zJ $= 10^{-21}$ J at 25°C) an oscillatory structural (solvation) force is expected to dominate over adhesion. Ignoring oscillatory hydration and DLVO forces, the purely hydrophobic attractive structural surface energy (negative sign) may be characterized [21,44] by:

$$\Delta_{str}^{attr} D^s = -C_{SL}\, e^{-l_{SL}/\lambda_o} = -2\gamma_{SL} e^{-l_{SL}/\lambda_o} \tag{105a}$$

where $20 < C_{SL}/(\mathrm{mJ/m^2}) < 100$ or $10 < \gamma_{SL}/(\mathrm{mJ/m^2}) < 50$) and decay length $1.0 < \lambda_o/\mathrm{nm} < 2.0$. As shown in Table 16 the minimum $\Delta_{vdW}D^s$, = 0.61 mJ/m^2 was found at $l_{max} = 2.96$ nm and the maximum $\Delta_{vdW}D^s$ = 4.99 mJ/m^2 at $l_{max=}$ 1.15 nm. The location of these repulsive maxima are, indeed in the range of $1.0 < \lambda_o/\mathrm{nm} < 2.0$. Assuming that $l_{max} = \lambda_o$ ($e^{-1} = 0.3679$) the attractive structural energy becomes $\Delta_{str}^{attr}D^s$ = -7.36 mJ/m^2 at $l_{max} = \lambda_o$ =2.96 nm and $\Delta_{str}^{attr}D^s$ = -36.8 mJ/m^2 at $l_{max} = \lambda_o$ =1.15 nm. These energies are of opposite sign as compared to $\Delta_{vdW}D^s$ given above. As indicated, the interfacial hydrophilic attraction energy decreases with reduced surface hydrophobicity. Empirically, the decay

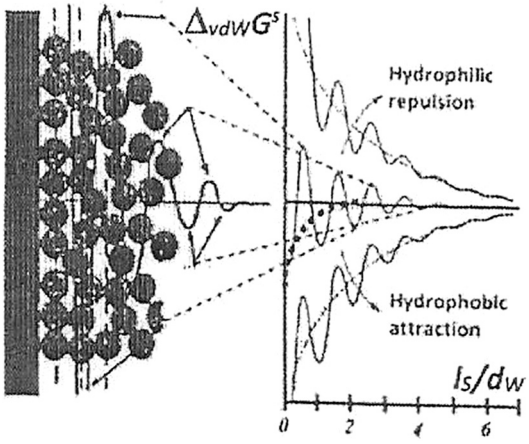

Fig. 29. Schematic illustration of an attractive and repulsive fluctuating potential due to packing of solvent molecules close to a molecularly smooth surface as a function of distance/solvent molecule diameter ratio (l_S/d_W, [21,44]). Optimal packing corresponds to maximum (repulsive) energy and disorder leads to minimum (attractive) interaction energy.

of hydrophilic structural repulsion (positive sign) in water follows the simple empirical relationships [21,44]:

$$\Delta_{str}^{rep} D^s = +\Delta_{SL} D^s\, e^{-l_{SL}/\lambda_o} \tag{105b}$$

where the interfacial energy is typically, $3 < \Delta_{SL}D^s/(\mathrm{mJ/m^2}) < 30$ and the characteristic decay length is $0.6 < \lambda_o/\mathrm{nm} < 1.1$, which is one or two times the range of oscillatory solvation force in water. As shown in Table 16 the minimum $\Delta_{el}D^s$, = 0.41 mJ/m^2 was found at $l_{max} = 2.96$ nm and the maximum $\Delta_{el}D^s$ = 5.38 mJ/m^2 at $l_{max=}$ 0.49 nm. The location of these repulsive maxima are, indeed in the range of $0.6 < \lambda_o/\mathrm{nm} < 1.1$. Assuming that $l_{max} = \lambda_o$ ($e^{-1} = 0.3679$) the repulsive structural energy becomes $\Delta_{str}^{rep}D^s$ = 1.10 mJ/m^2 at $l_{max} = \lambda_o$ =2.96 nm and $\Delta_{str}^{rep}D^s$ = 11.0 mJ/m^2 at $l_{max} = \lambda_o$ =0.49 nm. Both the magnitude and distance of repulsive structural forces agree roughly with the magnitude and distance of repulsive maximum (Table 16). The interfacial hydrophilic repulsive energy increases with enhanced surface hydrophilicity. For asymmetric molecules and heterogeneous solid surfaces, the oscillatory forces are smoothened out to the normal attractive van der Waals force decay with distance.

3.6.2. Dipole surface layering – interfacial potential jump

As discussed, water molecules may organize themselves into layers at solid–liquid interfaces. This results in a potential jump at the solid-liquid interface due to dipole and structural (solvation) forces. Assuming that the potential jump remains constant, its contribution cancels in deriving Nernst equation [28]. Since water is a dipole this results in a potential drop described by [28]:

$$\Delta_{dip}^{el}\varphi_W = \frac{q_W N_W^s d_W}{\varepsilon_o \varepsilon_W^s} = \frac{N_W^s p_W}{\varepsilon_o \varepsilon_W^s} \tag{106}$$

At charged interfaces, $6 < \varepsilon_W{}^s < 11$ [28] out of which $\varepsilon_W{}^s = 10$ is selected. When $N_W{}^s = 10^{18}\mathrm{m}^{-2}$ and $p_W = 6.216^{x}10^{-30}$ Cm, the potential drop becomes $\Delta_{dip}{}^{el}\varphi_W = 70.2$mV. It is reasonable to select the number of surface sites as a measure for $N_W{}^s$. According to Table 6 $N_{OH}{}^s/10^{-18} \approx 14$ ($z = 1$), 12 ($z = 2$), 10 ($z = 3$), 8 ($z = 4$) sites/m^2. Therefore dipolar surface potential drop may vary between, $561 < \Delta_{dip}\varphi_W/\mathrm{mV} < 983$. Faraday constant converts these limits to "bulk" values, $54.1 < \Delta_{dip}\varphi_m/(\mathrm{kJ/mol}) < 94.9$. Considering the water monolayer as a condenser the integral capacitance [41] is:

$$K_{dip} = \frac{q_W/A}{\Delta_{dip}^{el}\varphi_o} = \frac{\sigma_o}{\Delta_{dip}^{el}\varphi_o} \tag{107a}$$

with the unit (C/Vm^2) = (F/m^2). The inverse differential capacitance can be written in terms of surface potential and surface charge density as:

$$\frac{1}{C_{dip}} = \frac{d\left(\psi_o + \Delta_{dip}^{el}\varphi_o\right)}{d\sigma_o} \tag{107b}$$

As mentioned, asymmetric molecular dipoles and heterogeneous surfaces disrupt dipole layering.

3.6.3. Specific cation adsorption

The layering of dipoles and specifically bound cations is usually characterized as condensers coupled in series. Then, the charge density at all plates are equal, but opposite. As a result, the integral capacitance per unit surface is characterized by:

$$\frac{1}{C} = \frac{d\psi}{d\sigma} = \sum_i \left(\frac{1}{C_i}\right) \tag{108}$$

Specific adsorption of cations into Stern layer next to the solid-liquid interface are usually modeled by Langmuir isotherms. Surface coverage of metal cations within interfacial Stern layer ($\theta_M{}^s = N_M{}^S/N_{site}{}^s$) may, based on Eq. (47), be written in terms of surface charge densities [32,41] as:

$$\theta_M^S = \frac{\sigma_S}{\sigma_m} = \frac{zeN_M^S}{zeN_{site}^s} \quad \Leftrightarrow \quad \sigma_S = z_M e N_{site}^s \left(\frac{x_M^b K_{ads} e^{-z_M F\psi_o/RT}}{1 + x_M^b K_{ads} e^{-z_m F\psi_o/RT}} \right) \tag{109a}$$

where lower and upper index S denotes Stern layer and bulk concentration is expressed as mole fraction in order to avoid K_{ads} to be expressed by concentration unit. The adsorption against surface potential is recognized by a Boltzmann type correction, $K_{ads}^{\text{int}} = K_{ads} e^{-zF\psi_o/RT}$. Note that $N_M{}^S$ can be smaller, equal or larger than $N_{site}{}^s$. The term in denominator accounts for the effect of cations already present in Stern layer and is important when sites are almost fully occupied. This is seldom the case for adsorbed cations because of lateral repulsion. Eq. (109a) can therefore be simplified by neglecting this term as [46]:

$$\sigma_S = 2 z_M c_M r_M F e^{-z_M F\psi_o/RT} \tag{109b}$$

where r_M is the radius of adsorbed metal cation. Then $N_{site}{}^s$ is equalized with $2r_M N_V$ where $N_V$is the number of water molecules per unit volume. Fig. 30 illustrates the linear potential drop within Stern layer and subsequent exponential drop within diffuse electrolyte layer.

Considering the solid surface and imaginary interfaces as parallel condensers l_S and l_D apart, the surface charge density and surface coverage can be determined as a function of pH and dissolved (cat)ion concentration. Moreover, critical interlayer distance and critical cation concentration can be determined for the balance between attractive and repulsive forces as a function of pH and electrolyte concentration. The surface capacity of diffuse layer without specific cation adsorption may be defined [41] as:

$$K_d = C_d = \frac{\varepsilon_o \varepsilon_d}{l_d} = \frac{\sigma_o}{\psi_o - \psi_d} = -\frac{\sigma_d}{\psi_o - \psi_d} \quad \Leftrightarrow \quad \psi_o - \psi_d = \frac{\sigma_o l_d}{\varepsilon_o \varepsilon_d} \tag{110}$$

It has been shown that hydrated ions enforce the repulsive fluctuation solvation force at solid-liquid interfaces (Fig. 29). At distances below 5 nm $\Delta_{SL}G^s$ (Eq. (105b)) appears insensitive, or only weakly sensitive to the type and concentration of electrolyte [21,44]. At distances greater than 5 nm the attraction seem independent on electrolyte. Howevr, in dilute electrolyte solutions of divalent ions the van der Waals attraction seems to extend to 40 nm [21]. Other experiments indicate that at distances exceeding 5 nm, $\Delta_{SL}G^s$ depends on both the type and concentration of electrolytes.

Specific cation adsorption to Stern layer occurs as point charges to an approximate distance (l_S). The condenser is assumed chargeless enabling description of the linear potential drop as:

$$(\psi_o - \psi_S) = \frac{\sigma_o l_S}{\varepsilon_o \varepsilon_S} \tag{111a}$$

The subsequent potential change in diffuse layer may be related to Stern layer potential [41] as:

$$(\psi_S - \psi_d) = -\frac{\sigma_d (l_d - l_S)}{\varepsilon_o (\varepsilon_d - \varepsilon_S)} \tag{111b}$$

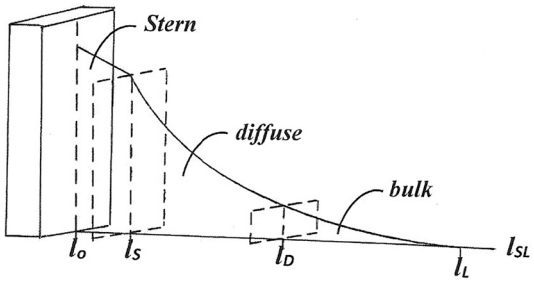

Fig. 30. Schematic illustration of the potential decay within Stern (linear potential drop) and diffuse (exponential potential decay) layers near a solid surface in the presence of electolyte. Imaginary Stern and diffuse layer planes may be modeled as parallel coupled condensers. The dipole layer has the same features as Stern layer, but it is omitted for simplicity.

The overall charge neutrality in the double layer requires that, $\sigma_o + \sigma_S + \sigma_d = 0$. In the absence of specific adsorption ($\sigma_S = 0$) the surface charge density relates to diffuse layer charge density as $\sigma_o = -\sigma_d$. Then the total inverse differential capacitance of the double layer is characterized [41] by:

$$\frac{1}{C} = \frac{1}{C_S} + \frac{1}{C_d} = \frac{d\psi_o}{d\sigma_o} = \frac{d(\psi_o - \psi_d)}{d\sigma_o} + \frac{d\psi_d}{d\sigma_o} \tag{112}$$

Expressing the double layer as condensers coupled in series (Eq. (112)), we can extract the diffuse layer potential as:

$$C_S = \frac{\sigma_o}{\psi_o - \psi_d} \quad C_d = \frac{\sigma_o}{\psi_d} \quad \Leftrightarrow \quad \psi_d = \frac{C_S \psi_o}{C_S + C_d} \tag{113}$$

Considering dipole layer (Eq. (107b)), the corresponding relationship [41] is:

$$\frac{1}{C} = \frac{1}{C_{dip}} + \frac{1}{C_d} = \frac{d(\phi_x - \psi_d)}{d\sigma_o} + \frac{d\psi_d}{d\sigma_o} \tag{114}$$

where ϕ_x is the inner (Galvani) potential of the solid. It is assumed that at any particular value of σ_o, the potential drop ($\Delta_{dip}{}^{el}\varphi_o$) is unaffected by electrolyte concentration.

Including dipole layer at surfaces, the double layer model would extend to triple parallel condensers coupled in series. However, instead of elaborating such model, the solvation, dipole interaction and other particular interfacial properties are introduced as an extended potential ($\psi_o \rightarrow (\psi_o + \phi_{solvation} + \phi_{dipole} + \phi_{image})$) of Eq. (109a) [33,41]. Here, $\phi_{solvation}$ represents van der Waals attraction, $\phi_{dipole} = \Delta_{dip}{}^{el}\varphi_o$dipole interaction and ϕ_{image} image forces across interface. Image force of a dipole or charge near a conductor is an attractive force generated by the interaction with their opposite image in the conductor. It is sometimes concluded that some cations are dehydrated and adsorb "naked" on the surface. This results in desorption of adsorbed dipoles and changed image forces, which makes the system exceedingly complex.

3.6.4. Summary

The solid-liquid interface induces enhanced packing of solvent (water) molecules due to loss of movement freedom and due to enhanced van der Waals and dipolar interactions. The solvent packing induces fluctuations of the smooth attractive force, which becomes repulsive in the presence of hydrated cations. The attractive structural (solvation) surface energy at solid–non-polar (air) environment was found to be -7.36 < $\Delta_{str}{}^{attr}D^s$/(mJ/m^2) < -36.8 (Eq. (105a)). Although the decay range are roughly equal the attractive van der Waals surface energy of 0.61 < $\Delta_{vdW}D^s$ /(mJ/m^2) < 4.00 in Table 16 is of opposite sign as compared to this attractive structural energy. The attractive structural energy is changed to a repulsive structural energy of 1.10 < $\Delta_{str}{}^{rep}D^s$/(mJ/m^2) < 11.0 in aqueous environment (Eq. (105a)). The electrostatic energy 1.10 < $\Delta_{el}D^s$/(mJ/m^2) < 11.0 in Table 16 is of same magnitude and range as this repulsive structural energy. Assuming 4.0 nm^2 interaction area and introducing Avogadro's number we find that: -48.2 < $\Delta_{str}{}^{attr}D_m$/(kJ/mol) < -241 and that 7.23 > $\Delta_{str}{}^{rep}D_m$/(kJ/mol) < 72.3. Expressed as kJ/mol the van der Waals energy limit becomes 1.46 < $\Delta_{vdW}D_m$/(kJ/mol) < 9.62 and the electrostatic interaction energy becomes 0.99 < $\Delta_{el}D_m$/(kJ/mol) < 12.9 (Table 16). The overall DLVO interaction energy amounts to -0.51 < $\Delta_{DLVO}D_m$/(kJ/mol) < 7.75 at 0.49 < l_{max}/nm < 2.85. Both dipole layering and specific cation adsorption results in a (linear) surface potential drop. The potential drop due to dipole layering at surface sites was estimated to be 54.1 < $\Delta_{dip}\varphi_m$/(kJ/mol) < 94.9. An estimate of potential drop due to cation adsorption can be extracted from Table 14. Faraday's constant can be used to convert limiting low/high surface energies to kJ/mol: 22.9 (z_M = 1), -5.71/45.6 (z_M = 2), and -13.3/62.8 (z_M = 3). The predicted DLVO surface energies for 1:1 electrolytes (Table 16) were in the range: -0.51 $\Delta_{str}{}^{rep}D^s$/(kJ/mol) < 7.75. The increased surface energy with cation valence (z_M) may be taken as a sign of enhanced adsorption specificity.

When the interfacial range is considered as parallel condensers coupled in series, it can be characterized quantitatively in terms of surface potentials, surface charge densities and surface coverages.

4. Hydration and hydrolysis of dissolved cations

In previous discussion cations were considered as non-reactive point charges in water continuum. This does not reflect reality where acidic potential determining cations react with water to form a variety of aquo-, hydroxo-, oxohydroxo- and sometimes oxo-complexes. As discussed a part of hydrated cations are immobilized by electrostatic interaction and by hydrogen bonds to surface hydroxyls to form a Stern layer (Fig. 31).

Note that the surface roughness usually exceeds the extension of structural (solvation) force, dipolar layer and Stern layer of specifically bound cations [47]. Previously the interaction of surface site hydroxyls with protons and adsorbed water was evaluated. In this section the attention is directed onto released cation – water interactions.

4.1. Chemical equilibria – cation acidity and hydrolysis

In aqueous solutions only a part of metal cations (M) may dissolve from solids as:

$$M_xA_y \Leftrightarrow M_{x-1}A_y^{z-} + M^{z+} \tag{115}$$

Dissolution is aided by formation (coordination, ligation) of hydrated (h) complexes:

$$M^{z+} + hH_2O \Leftrightarrow M(OH_2)_h^{z+} \tag{116}$$

where h is the coordination number of water molecules bound to primary hydration shell of metal cations. The total number of water molecules associated to metal cations has been concluded to exceed their coordination number. The empirical relationship $N_h = 0.36^{x}10^{-9}\,(z_M/r_M)$ has been derived [38] from $\Delta_{hyd}{}^{abs}D_m{}^{\theta}$ data and is shown as a function of $\Delta_{hyd}{}^{abs}G_m{}^{\theta}$ (Eq. (73), Appendix 6) in Fig. 32.

Increasing cation valence (from right to left) results in a slightly shifted linear dependence with a decreased slope. Deviations may be due to a coordination number differing from the assumed $N_C = 6$. According to this model, a high valence and a small radius increase the number of bound water molecules in excess of coordination number of cations. Cumulative hydrolysis constant is the product of stepwise protolysis

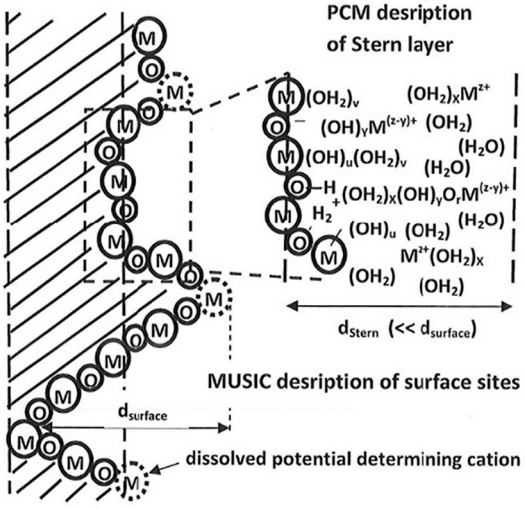

Fig. 31. Realistic illustration of a rough metal oxide surface where the roughness exceeds the thickness of Stern layer [28]. Insertion: Interaction between hydroxylated surface sites (quantified by MUSIC model) and oxo-hydroxo-aquo metal cat- and an-ions (quantified by PCM model).

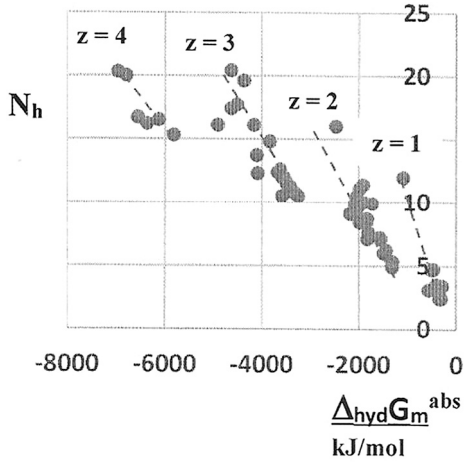

Fig. 32. Number of water molecules (N_h) associated to cations ($N_C = 6$) plotted as a function of absolute Gibbs molar free energy of hydration (Eq. (73), Appendix 6).

constants of water [25] as:

$$M^{z+} + hH_2O \leftrightarrow M(OH)_h^{(z-h)+} + hH^+$$
$$K_{hi} = \Pi_i k_{hi} = \frac{\left[M(OH)_h^{(z-h)+}\right][H^+]^h}{[M^{z+}][H_2O]^h} \tag{117a}$$

Since reactions occur in acidic and neutral solutions the valence is expressed as positive. Cumulative hydrolysis constants for a range of metal (hydr)oxides are collected in Appendix 7. Alternatively, hydrolysis may be considered as a Brϕnsted type deprotonation of aqueous solvation shells:

$$M(OH_2)_h^{z+} \leftrightarrow M(OH)_k(OH_2)_{h-k}^{(z-k)+} + kH^+ \tag{117b}$$

In some cases, single or multiple ligand coordination may be of interest. Then, only reactions between metal cation and hydroxyl ligands are of interest. The consequtive formation of cation complexes with hydroxyl ligands are defined with cumulative complexation constants/products [26] as:

$$M^{z+} + kOH^- \leftrightarrow M(OH)_k^{(k-z)-} \Leftrightarrow \quad K_{ki} = \Pi_i\beta_{ki} = \frac{\left[M(OH)_k^{(k-z)-}\right]}{[M^{z+}][OH^-]^k} \tag{118}$$

Since reactions are expected to occur in alkaline solutions the valence is expressed as negative. Cumulative hydroxyl complexation constants are listed in Appendix 7. Fig. 33 shows that hydrolysis of cation hydroxo-aquo complexes results in enhanced acidity and complex formation in reduced alkalinity of aqueous solutions.

Note that hydrolysis constants are related to complexations constants

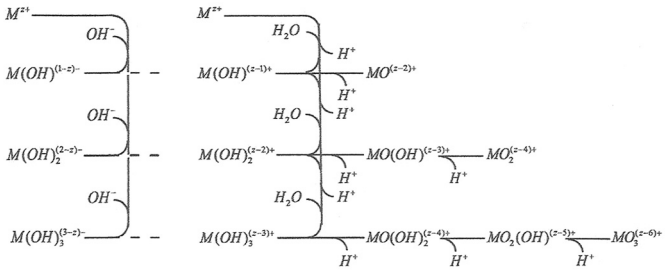

Fig. 33. Right flow diagram (top-to-bottom): Three step hydrolysis of a metal cation (cumulatively, K_{hi}) and (left-to-right): Three step proton release from metal (hydr)oxides (cumulatively, K_{ai}). Left diagram (top-to-bottom): Complexation of hydroxyl ions to metal cation (K_{ki}).

for mono-hydroxides as:

$$M^{z+} + H_2O \leftrightarrow M(OH)_1^{(z-1)+} + H^+ \Leftrightarrow \quad K_{h1}$$

$$M(OH)_1^{(1-z)-} \leftrightarrow M^{z+} + OH^- \Leftrightarrow \quad 1/K_{k1}$$

$$H_2O \leftrightarrow H^+ + OH^- \Leftrightarrow \quad K_W$$

where K_W is the ion product of water. Obviously, $pK_W = pK_{h1} - pK_{k1}$. The step-by-step protolysis from metal hydroxides are characterized by acid constants (k_{ai}), which characterize the increase of oxygen ligands in the oxo-hydroxo cluster. Introducing initially a neutral metal hydroxide we express the cumulative equilibrium as:

$$M(OH)_k^{(z-k)+} \leftrightarrow MO_l(OH)_{k-l}^{(z-2l-k)+} + lH^+$$
$$K_{al} = \Pi_i k_{ai} = \frac{\left[MO_l(OH)_{k-l}^{(z-2l-k)+}\right][H^+]^l}{\left[M(OH)_k^{(z-k)+}\right]} \tag{119}$$

Since reactions occurs in acidic and neutral solutions the valence is expressed as positive. The stepwise acid constants (Appendix 8) show an interesting pattern. The number of oxo ligands determines primarily k_{ai}, while the number of hydroxyl ligands plays a second-hand role. For neutral metal hydroxides, k_{ai} can be estimated [28,48] from:

$$pk_{ai} = -logk_{ai} = 7 - 5l \tag{120a}$$

Selecting chlorine containing acids as example, we find the sequence: pk_{a1}(ClOH) = 7 (7.3), pk_{a2}(ClO(OH)) = 2 (2.0), pk_{a3}(ClO_2OH) = -3 (-1.0), pk_{a1}(ClO_3OH) = -8 (-8.5). The values in parenthesis are from Appendix 8. Deviations are due to mineral acid structure and internal bonds. Note that hydrides have almost the same acid constants as corresponding hydroxides. When a neutral metal hydroxide has lost one proton the successive pk_{ai} values are about five units apart. This observation can be formalized for charged oxo-hydroxyl cations, $MO_l(OH)_k^{z+}$ [28,48] as:

$$pk_{ai} = -logk_{ai} = 7 - 5(l + 2z) \tag{120b}$$

For neutral$PO(OH)_3$ pk_{a1} = 2 (2.1), the charged species are $PO_2(OH)_2^-$ ($l = 2$, $z = -1$) $pk_{a2} = 7$ (7.1) and $PO_3(OH)_1^{2-}$ ($l = 3$, z = -2) $pk_{a3} = 12$ (12.0). The values in parenthesis are from Appendix 8. Mineral acids are here considered as metal (hydr)oxides in order to illustrate the interconnection between hydrolysis constants and complexation constants (Fig.30).

In the following, key processes of aluminum cations in aqueous solutions are used as models. The coordination number may change from $N_C = 6$ in acidic solutions to $N_C = 4$ in alkaline solutions. Assuming $N_C = N_W = 4$ the successive stepwise hydrolysis of aluminium cations are characterized by the following hydrolysis constants [12,28]:
$Al^{3+} + H_2O \leftrightarrow Al(OH)^{2+} + H^+$ $k_{h1} \approx 6.7 \cdot 10^{-6}$ $pk_{h1} \approx 5.2$ $Al(OH)^{2+} + H_2O \leftrightarrow Al(OH)_2^+ + H^+$ $k_{h2} \approx 5.5 \cdot 10^{-6}$ $pk_{h2} \approx 5.3$ $Al(OH)_2^+ + H_2O \leftrightarrow Al(OH)_3^o + H^+$ $k_{h3} \approx 9.1 \cdot 10^{1}$ $pk_{h3} \approx -2.0$ $Al(OH)_3^\circ + H_2O \leftrightarrow Al(OH)_4^- + H^+$ $k_{h4} \approx 1.0 \cdot 10^{-14}$ $pk_{h4} \approx 14.0$where k_{ki} are step-wise hydrolysis constants. ALCOA manual [49] reports that $k_{h4} = 8.94 \cdot 10^{-15} \Rightarrow pk_{h4} = 14.05$. The cumulative equilibrium hydrolysis constant can be calculated as:

$$K_{hi} = \Pi_i k_{hi} \quad \Leftrightarrow \quad pK_{hi} = \Sigma_i pk_{hi} \tag{121}$$

The resulting cumulative hydrolysis constants are identified by the number of released protons [28] as:

$$Al^{3+} + H_2O \leftrightarrow Al(OH)^{2+} + H^+ \quad \Leftrightarrow \quad pK_{h1} = 5.2\,(5.02, 4.97)$$

$$Al^{3+} + 2H_2O \leftrightarrow Al(OH)_2^+ + 2H^+ \quad \Leftrightarrow \quad pK_{h2} = 10.5\,(8.56, 9.30)$$

$$Al^{3+} + 3H_2O \leftrightarrow Al(OH)_3^\circ + 3H^+ \quad \Leftrightarrow \quad pK_{h3} = 8.5\,(8.11, 15.0)$$

$$Al^{3+} + 4H_2O \leftrightarrow Al(OH)_4^- + 4H^+ \quad \Leftrightarrow \quad pK_{h4} = 22.5\,(23.0, 23.0)$$

Note that the neutral $Al(OH)_3$(aq) complex is an aqueous complex. The constants in parenthesis are reported by Hem and Roberson [50] and by Baes and Mesmer [25]. Hydration constants, molar Gibbs free hydration energies, molar hydration enthalpies and formation constants, molar Gibbs free formation energies, molar enthalpies of mono- and polynuclear aqueous aluminium (oxo) hydroxides, reported by Baes and Mesmer [25], Hem and Roberson [50], Wefers and Misra [49] and Pourbaix [51] are assembled in Appendix 7 and listed in Table 17.

The formation of polynuclear complexes are not evaluated further in this review. The solubility of each dominant species from 0.011 mol/dm^3 ($pI = 1.96$) *Al*-solutions can be expressed by the following cumulative proton association equilibria [12,50]:

$$Al(OH)_3^o + H^+ \leftrightarrow Al(OH)_2^+ + H_2O \qquad K_{12} \approx 1.1{\cdot}10^{-2} \quad pK_{12} = 2.0$$

$$Al(OH)_3^o + 2H^+ \leftrightarrow Al(OH)^{2+} + 2H_2O \qquad K_{11} \approx 2.0{\cdot}10^{3} \quad pK_{11} = -3.3$$

$$Al(OH)_3^o + 3H^+ \leftrightarrow Al^{3+} + 3H_2O \qquad K_{10} \approx 3.0{\cdot}10^{8} \quad pK_{10} = -8.5$$

ALCOA manual [49] reports the following equilibrium constants: $K_{12} \approx 9.49 \cdot 10^{-3} \Rightarrow pK_{12} = 2.02$, $K_{11} \approx 1.33 \cdot 10^{3} \Rightarrow pK_{11} = -3.12$ and $K_{10} \approx 1.29 \cdot 10^{8} \Rightarrow pK_{10} = -8.11$. These reactions occur in acidic solutions and agree with the hydrolysis constant reported in Appendix 4. Hydrolysis constants for species in aqueous solutions correspond to acidity constants for hydroxyl groups at surface sites. Dissolving Gibbsite in alkaline solutions results in formation of anionic aluminum tetrahydroxide complexes [25] as:

$$Al(OH)_3^o + OH^- \leftrightarrow Al(OH)_4^- \qquad k_{14} \approx 3.16{\cdot}10^{-15} \quad pk_{14} = 14.5$$

For Bayerite dissolved in alkaline solutions $pk_{14} = 14.0$. This corresponds to the Gibbs free solubility product energy listed in Table 16. However, no of these constants agree with the solubilty product ($32.0 < pK_{sp} < 33.5$) listed in Appendix 4. Dissolving solid aluminium trihydroxide aqueous species (Eq. (42)) must be accounted for [25] as:

$$Al(OH)_3^o(s) \leftrightarrow Al(OH)_3^o(aq) \quad \Leftrightarrow \quad K_{sol} = \frac{\left[Al(OH)_3^o(aq)\right]}{\left[Al(OH)_3^o(s)\right]} \tag{122}$$

The solution constant (K_{sol}) for a few solids (unfortunately not *Al*$(OH)_3^o(s)$) are reported in Appendix 6. The overall solubility limit of Gibbsite, *Al*$(OH)_3^o$ may be related to solution acidity (*pH*) using the following simplified mass (concentration) balance [12,28,49,50]:

$$[Al]_{tot} = \left[Al^{3+}\right] + \left[Al(OH)^{2+}\right] + \left[Al(OH)_2^+\right] + \left[Al(OH)_3^o\right] + \left[Al(OH)_4^-\right] \tag{123}$$

Other mononuclear and oligomeric aluminium cat/an-ion species has been neglected. The pH dependence can be determined by inserting corresponding constants in Eq. (123) as:

$$[Al]_{tot} = K_{10}[H^+]^3 + K_{11}[H^+]^2 + K_{12}[H^+] + K_{14}(1/[H^+]) = 3.0{\cdot}10^{8}[H^+]^3 + 2.0{\cdot}10^{3}[H^+]^2 + 1.1{\cdot}10^{-2}[H^+] + 1.0{\cdot}10^{-13}/[H^+] \tag{124}$$

Fig. 34 illustrates the distribution (fraction) of these primary aluminium hydroxide species.

As shown the distribution of species is strongly dependent on the total aluminum concen-tration ($p[Al^{3+}]$) and solution *pH*. Cumulative hydrolysis constants of metal oxo-hydroxides and metal oxides formed by high valent ($z_M > 4$) metal cations was expressed (Eq. (117a))) as:

$$M^{z+} + hH_2O \leftrightarrow M(OH)_h^{(z-k)+} + hH^+ \quad \Leftrightarrow \quad K_{hi} = \Pi_i k_{hi} \tag{125}$$

Cumulative hydrolysis constants [25] for a range of metal cations are collected in Appendix 7. The dependence of logarithmic cumulative hydrolysis constants (pK_{hi}) on ion potential (z_M/r_M) is shown in Fig. 35.

Although the scatter is considerable, roughly linear, but branched

Table 17
Average cumulative hydrolysis constants (pQ_{hi}, concentrations), (pK_{hi}, activities), molar Gibbs free hydration energy ($\Delta_{hyd}G_m$, kJ/mol) and hydration enthalpy ($\Delta_{hyd}H_m$, kJ/mol) of the most stable mono- and polynuclear aluminium hydroxide complexes. $Al(OH)_3^o$ = dissolved aqueous complex. Average formation constants (pK_{fo}, activities), molar Gibbs free formation energy $\Delta_{fo}G_m$, kJ/mol) and formation enthalpy $\Delta_{fo}H_m$, kJ/mol) of aluminium (oxo)hydroxides [25,28,49–51]. (am) = amorphous, (μc) = microcrystalline, (Gi) = Gibbsite, (Ba) = Bayerite, (Bo) = Boehmite, (Di) = Diaspore, (Co) = corundum.

	pQ_{hi}	pK_{hi}	$\Delta_{hyd}G_m$	$\Delta_{hyd}H_m$		pK_{fo}	$\Delta_{fo}G_m$	$\Delta_{fo}H_m$
Al^{3+}					Al^{3+}	-84.6	-483	-531
$Al(OH)^{2+}$	5.2	5.00	28.5	49.8	$Al(OH)^{2+}$	-121	-690	
$Al(OH)_2^+$	9.9	8.93	51.0		$Al(OH)_2^+$	-158	-900	
$Al(OH)_3^o$	15.6	15.0	85.6		$Al(OH)_3^o$			
$Al(OH)_4^-$	23.0	23.0	131		$Al(OH)_4^-$	-229	-1309	
$Al_2(OH)_2^{4+}$	8.0	7.51	42.8	78.2	$Al(OH)_3$(am)	-199	-1138	
$Al_3(OH)_4^{5+}$	13.5	13.9	79.6	148	$Al(OH)_3$(μc)	-200	-1139	
$Al_7(OH)_{17}^{4+}$		48.8	279		$Al(OH)_3$(Gi)	-202	-1154	-1293
$Al_{13}(OH)_{34}^{5+}$		97.6	557		$Al(OH)_3$(Ba)	-202	-1152	-1288
$Al_{13}O_4(OH)_{24}^{7+}$		98.7	564	1166	AlO(OH)(Bo)	-160	-913	-990
					AlO(OH)(Di)	-161	-921	-1000
					Al_2O_3(Co)	-277	-1582	-1675

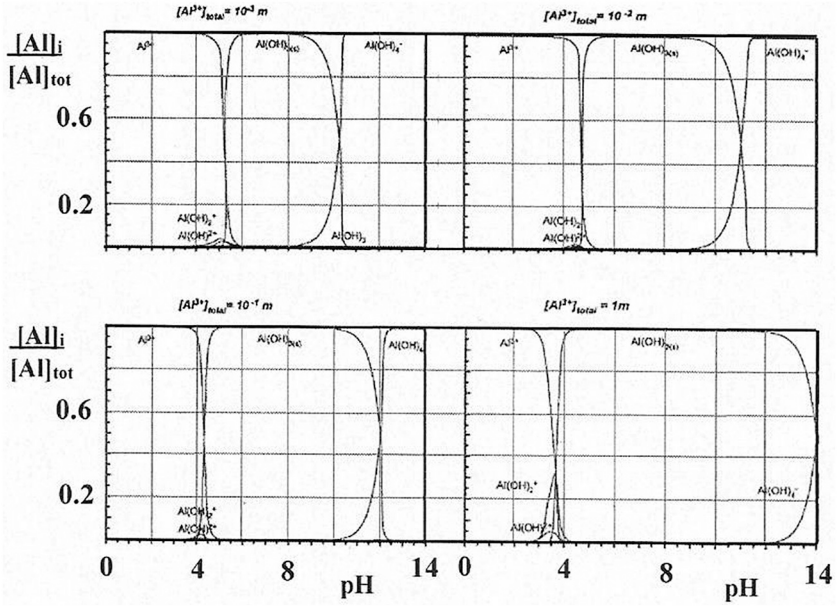

Fig. 34. Fractions of aluminium hydroxyl species [$Al(OH)_z$] as a function of pH at four total aluminium concentrations at 25°C [12,28].

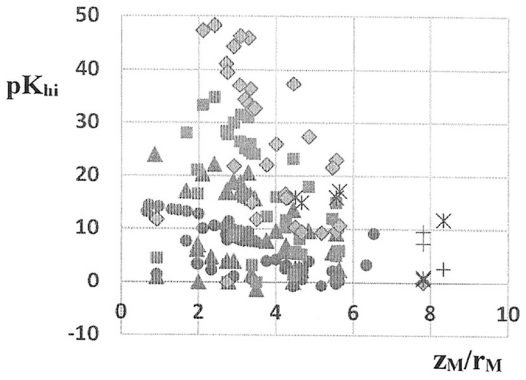

Fig. 35. Dependence of cumulative logaritmic hydrolysis constants (pK_{hi}, Eq (117a)) of metal cations (Appendix 7) on ion potential (z_M/r_M). Monohydroxides ($pK_{h,1}$, circles), dihydroxides ($pK_{h,2}$, triangles), trihydroxides ($pK_{h,3}$, squares), tetrahydroxides ($pK_{h,4}$, diamonds), pentahydroxides ($pK_{h,5}$, asterisks) and hexahydroxides ($pK_{h,6}$, plus).

dependencies are found for each degree of hydrolysis. The steepest reduction of pK_{hi} with increasing ion potential (z_M/r_M) is found for tetrahydroxides, followed by tri-, di- and monohydroxide species. Since ion hydration should be related to cation hydrolysis Fig. 36 presents pK_{hi} plotted against $pK_{hyd} = \Delta_{hyd}G_m^{\theta}/2.3RT$ (Appendix 6).

The linearity is, indeed improved resolving the slopes for each set of hydrolysis constants. The best correlation is found for relative logarithmic hydration constants. There is a particular minimum found at $pK_{hyd}^{abs} = 1149$ (Pu^{4+}) and $pK_{hyd}^{rel} = 195$ (Fe^{3+}). A general observation is that hydration and hydrolysis are, as expected closely related properties.

4.1.1. Summary

Cations react with water in successive steps which may be classified as hydrolysis, hydroxyl complexation and as acid protolysis. These ractions are quantified by their cumulative equilibrium constants. The low < high molar Gibbs free energy dependencies on cation valence is listed in Table 18.

Considering the number of involved reaction steps (in parenthesis) the cumulative molar Gibbs energy changes as: $\Delta_{hi}G_m^{\theta} > \Delta_{ki}G_m^{\theta} > \Delta_{ai}G_m^{\theta}$. Although not conclusive, the energy change seems to increase with cation valence (z_M). Overall, the molar Gibbs free energies are of expected magnitude.

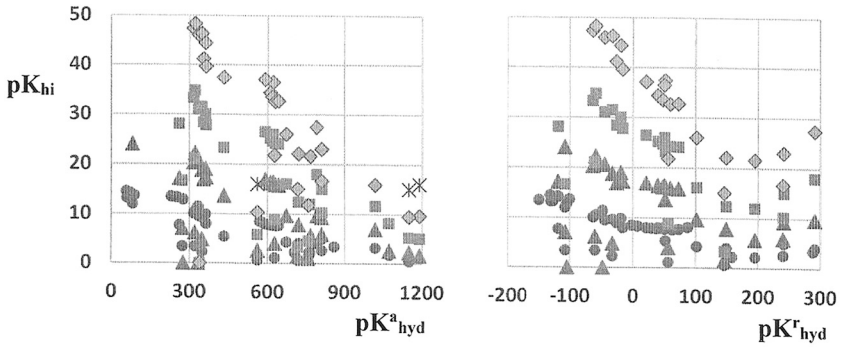

Fig. 36. Dependence of cumulative logarithmic metal cation hydrolysis constant (pK_{hi}, Appendix 7) on logaritmic hydration constants (Appendix 6). Absolute values (pK^{a}_{hyd}, left diagram) and relative (conventional) values (pK^{r}_{hyd}, right diagram). Monohydroxides ($pK_{h,1}$, circles), dihydroxides ($pK_{h,2}$, triangles), trihydroxides ($pK_{h,3}$, squares), tetrahydroxides ($pK_{h,4}$, diamonds) and pentahydroxides ($pK_{h,5}$, asterisks).

Table 18
Cumulative low<high limits of hydrolysis, hydroxyl complexation and acid constants/molar Gibbs energies (kJ/mol) for metal hydroxides as a function of cation valence (z_M). Values in parenthesis indicate the number of reaction steps. Data extracted from Appendix 7 and 8.

	pK_{hi}	$\Delta_{hi}G_m$	pK_{ki}	$\Delta_{ki}G_m$	pK_{ai}	$\Delta_{ai}G_m$
z =	12.0 < 24	68.5 <	-0.7 < 4.8	-4.0 <	7.3 <	41.7 <
1	(2)	137	(3)	27.4	10.1 (1)	57.6
z =	2.3 <	13.1 <	0.7 <	4.0 <	2.4(1)	13.7
2	48.3 (4)	276	15.5 (4)	88.5		
z =	-1.5 <	-8.6 <	3.9 <	22.3 <	1.9 <	10.8 <
3	36.5 (4)	208	25.4 (2)	145	13.4 (3)	76.5
z =	-0.3 <	-1.7 <	9.7 <	55.4 <	8.9 <	50.8 <
4	17.2 (5)	98.2	53.0 (4)	303	12.0 (3)	68.5

4.2. Semi-quantitative and empirical models

Cation reactions results in proton and hydroxyl exchange with bulk and coordinated water. It is therefore of interest to relate hydrolysis to proton association and to establish the extent of protolysis in neutral, acidic and alkaline aqueous electrolyte solutions.

4.2.1. Multisite complexion (MUSIC) model

Proton association constants for dissolved singly hydrated ($h = 1$) metal species are defined within MUSIC model [11] as:

$$M - O^{\upsilon_M - 2} + H^+ \leftrightarrow M - OH^{\upsilon_M - 1} \quad \Leftrightarrow \quad k_{11} = \frac{[MOH^{\upsilon_M - 1}]}{[MO^{\upsilon_M - 2}][H^+]} \tag{126a}$$

$$M - OH^{\upsilon_M - 1} + H^+ \leftrightarrow M - OH_2^{\upsilon_M} \quad \Leftrightarrow \quad k_{12} = \frac{[MOH_2^{\upsilon_M}]}{[MO^{\upsilon_M - 1}][H^+]} \tag{126b}$$

We generalize the proton association equilibrium constants for each step (Eq. (61)) as:

$$pk_{1n} = log\left(\frac{1}{k_{1,n}}\right) = -\frac{1}{2.3RT}\left(\Delta_{Born}G_m^{\theta} + \Delta_H^{chem}G_m^{\theta}\right) + B_{HM}\left(\frac{\upsilon_M}{l_{H-M}}\right) \tag{127}$$

where n = number of associated protons. Fig. 37 shows the dependence of logaritmic proton association constants on υ_M/l_{H-M}.

The parallel lines indicate that the successive proton association constants of hydroxo and oxo species are about 13 units apart. The regularity resembles acid constants expressed by Eq. (120a) and (120b). The proton association to aluminium tetrahydroxide anion $pK_{11=} - pK_{k4} = -14$) and to neutral aluminium trihydroxide ($K_{12=} - K_{k3} = 2$) equals roughly that of proton association to aqueous hydroxide anion ($pK_{W=}$ 14, open triangles) and to water ($pK_{1,2} = -1$, filled triangles). This difference is quite large because proton association occurs on the same site and involve strong H-H repulsions. For polyacids, successive $pk_{1,n}$ values differ by about 5 units. Since N_C and $l_{HO\text{-}OM}$ (Yoonś model, Eq.(70b)

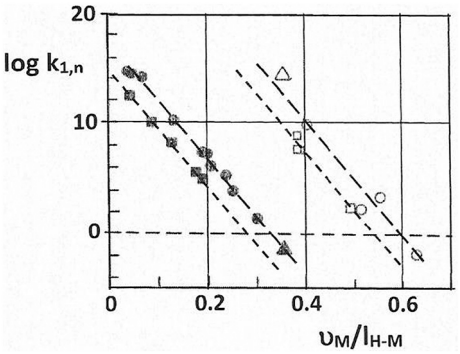

Fig. 37. Dependence of logarithmic proton association constants on modified ion potential, υ_M/l_{HM} ratio [11]: Neutral hydroxo complexes with rare gas configuration: $logk_{1,1}$ (open cricles), $logk_{1,2}$ (filled circles) and d^{10} elements: $logk_{1,1}$ (open squares), $logk_{1,2}$ (filled squares). Reference water: $logk_{1,1}$ (open triangles), $logk_{1,2}$ (filled triangle).

[35]) for most metal (hydr)oxides are unavailable, the hydrolysis constants in Appendix 7 were replotted against corrected ion potential $z_M/l_{HO\text{-}M}$ and according to Parks' model (Eq. (63), [31]) against $z_M/l_{2HO\text{-}M}$. The result is shown in Fig. 38.

There is, indeed an improvement as compared to Fig. 35. Each set of pK_{hi} for metal hydroxides are almost linearly dependent on ($z_M/l_{H\text{-}M}$). The slopes decrease as: $M(OH)_4 > M(OH)_3 > M(OH)_2 >$ MOH. The slopes for penta- and hexahydroxides are almost zero which may be due to the small number of samples compared. It is obvious that the double hydroxide-metal cation distance (Parks model, Eq. (63)) results in a fictive pillar assembly of experimental points. The single hydroxide-metal cation distance provides a more reasonable spread of data points. As shown in Fig. 38 the best resolution of each $pK_{h,1}$ class was, however achieved when it was plotted against relative pK^{r}_{hyd} (Fig.36).

4.2.2. Partial charge (PCM) model

Jolivet [11] developed electronic partial charge (PCM) model in order to predict the nature and extent of Brϕnsted acid-base equilibria of both neutral and charged acidic metal cations in aqueous solutions. The relationship between valence and formal partial charge (introduced within MUSIC model) for surface sites is defined as:

$$z_M = \Sigma_i N_i \delta_M \tag{128}$$

The electronegativity of metal cations is expected to change linearly with its partial charge as:

$$\chi_M = \chi_M^* + k_M \delta_M \sqrt{\chi_M^*} \tag{129}$$

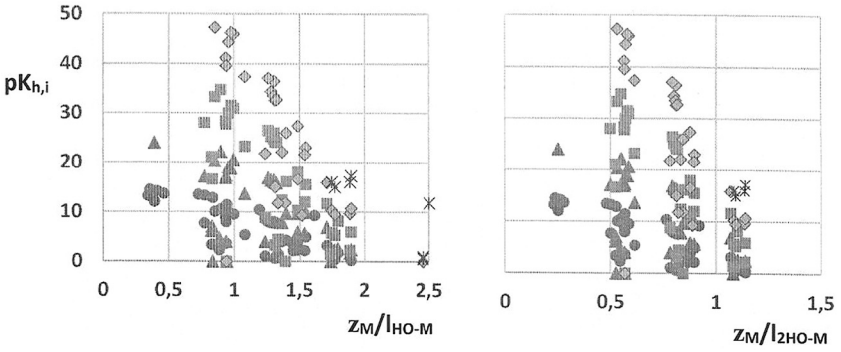

Fig. 38. Dependence of cumulative logaritmic hydrolysis constants (pK_{ki}) of metal cations listed in Appendix 5 on modified ionic potential, $z_M/l_{2HO\text{-}M}$ and on Parks $z_M/l_{2HO\text{-}M}$. Monohydroxides ($pK_{h,1}$, circles), dihydroxides ($pK_{h,2}$, triangles), trihydroxides ($pK_{h,3}$, squares), tetrahydroxides ($pK_{h,4}$, diamonds), pentahydroxides ($pK_{h,5}$, asterisks) and hexahydroxides ($pK_{h,6}$, plus).

where χ_M*is Allred-Rochow electronegativity for neutral atoms (Appendix 2), k_M =1.36 and $\eta_M = k_M\sqrt{\chi_M^*}$ corresponds to metal cation hardness. Incorporating the influence of charges to the average electronegativity of singly coordinated metal oxide cation species, Eq. (10a) is modified [11,28] as:

$$\chi^J = \chi^*(M_xO_y) = \frac{x\sqrt{\chi_M^*} + z\sqrt{\chi_O^*} + 1.36z_M}{x/\sqrt{\chi_M^*} + z/\sqrt{\chi_O^*}} \tag{130a}$$

By introducing hydrogen to the balance we find average electronegativity of metal hydroxides (Eq. (10b), [11,28]) as:

$$\chi^J = \chi^*(M_x(OH)_z) = \frac{x\sqrt{\chi_M^*} + z\sqrt{\chi_O^*} + z\sqrt{\chi_H^*} + 1.36z_M}{x/\sqrt{\chi_M^*} + z/\sqrt{\chi_O^*} + z/\sqrt{\chi_H^*}} \tag{130b}$$

In acidic and neutral solutions only aquo and hydroxo-aquo complexes remain stable. The formal partial charge distribution may now be expressed [11] as:

$$\delta_M = \frac{\chi_M^*(M_xO_y - \chi_M^*}{1.36\sqrt{\chi_M^*}} = \omega_M\left[\chi_M^*(M_xO_y) - \chi_M^*\right] \tag{131a}$$

and as:

$$\delta_M = \frac{\chi_M^*(M_x(OH)_z) - \chi_M^*}{1.36\sqrt{\chi_M^*}} = \omega_M\left[\chi_M^*(M_x(OH)_z) - \chi_M^*\right] \tag{131b}$$

where $\omega_M = 1/\eta_M$, represents softness of metal cations. Protolysis of hydrated metal cations (Eq. (116)) is chosen instead of metal cation hydrolysis. The cumulative proton release (protolysis, olation) may be written as:

$$\left[M(OH_2)_h\right]^{z+} \leftrightarrow \left[M(OH)_k(OH_2)_{h-k}\right]^{(z-k)+} + kH_{hyd}^+ \tag{132}$$

In acidic and neutral solutions the complex valence is assumed to be positive. Proton dissociation is considered a result of hydration of the released proton to hydronium ions ($H_{hyd}^+ = [H_9O_4]^+$). Coordinated water molecules behave as stonger acids than bulk water. The process continues until δ_{OH} remains positive, because negatively charged hydroxyls would attract protons and prevent protolysis. When δ_{OH}= 0 the equilibrium deprotonated (hydrolyzed) species are characterized by:

$$\chi^J = \chi^*\left[M(OH)_k(OH_2)_{h-k}\right]^{(z-k)+} \tag{133a}$$

In accordance with electroneutrality principle the average electronegativity of the complex and aqueous proton complex in solution become equal. The averaged electronegativity of the aquo-hydroxo complex can be estimated [11,28] as:

$$\chi^J = \frac{\sqrt{\chi_M^*} + h\sqrt{\chi_O^*} + (2h-k)\sqrt{\chi_H^*} + 1.36(z-k)}{1/\sqrt{\chi_M^*} + h/\sqrt{\chi_O^*} + (2h-k)/\sqrt{\chi_H^*}} \tag{133b}$$

Average electronegativities of some cation aquo-hydroxo complexes of aluminium are compared with those of iron and silicium in Table 19.

.

In neutral solutions ($pH = 7$) the electronegativity of protons in the hydrated complex, $\chi_{H^+}^* = \chi[H(OH_2)_\infty]^+ = 2.487$ is almost equal to water $\chi_{H2O}^* = 2.491$, which is considered the electronegativity of solution (χ_{soln}^*). Although PCM is a microscopic model independent of macroscopic changes in concentration, temperature and *pH* the electronegativity of solution may be interconnected with changes in *pH* [11,28] as:

$$\chi_{soln}^* = 2.621 - 0.02\,pH \quad \Leftrightarrow \quad 2.341 < \chi_{soln}^* < 2.621 \tag{134}$$

The number of protons released (number of hydroxyls, *k*) previously calculated [11,28] as:

$$k = \left[\frac{1}{1+0.41\,pH}\right]\left[(1.36\,z_M - h)(0.236 - 0.08\,pH) - \frac{(2.621 - 0.02pH) - \chi_M^*}{\sqrt{\chi_M^*}}\right] \tag{135}$$

Protolysis is controlled primarily by metal cation valence (formal charge number, z_M), but also by its original coordination of water molecules *h* (size) and its electronegativity. The calculated *k* need not be an integer. Then, two equilibrium complexes should be considered jointly and at least one of them should be a hydroxo complex.

At pH = 0 the electronegativity of hydrated proton complex $H_{hyd}^+ = [H_9O_4]^+$ is 2.621. However, $pH = 0$ was not simply inserted into Eq. (135). Instead, the following relation was suggested [11,28]:

$$k = 1.36\,z_M - 0.236\,h - \frac{2.621 - \chi_M^*}{\sqrt{\chi_M^*}} \tag{136a}$$

where water coordination number is assumed to be $h = 6$. For negative *k*-values the aquo ion does not exhibit any acid character. However, it may be deprotonated by the addition of a base and eventually forms a

Table 19
Average electronegativities of some metal cation- and anion hydroxo-aquo complexes (acids, Eq. (123b)). $\chi_H^* = 4.071$, $\chi_{OH}^* = 2.711$, $\chi_{H2O}^* = 2.491$ [11,12,25,28].

cations, anions	χ^J	cations, anions	χ^J	cations, anions	χ^J
$N_M = 6$		$N_M = 4$		$N_M = 4$	
$Al(OH_2)_6^{3+}$	2.754	$Fe(OH_2)_4^{3+}$	2.90	$SiO_2(OH)_2^{2-}$	2.10
$Al(OH)(OH_2)_5^{2+}$	2.675	$FeOH(OH_2)_3^{2+}$	2.80	$SiO(OH)_3^-$	2.37
$Al(OH)_2(OH_2)_4^+$	2.588	$Fe(OH)_2(OH_2)_2^+$	2.68	$Si(OH)_4^o$	2.58
$Al(OH)_3(OH_2)_3^o$	2.487	$Fe(OH)_3(OH_2)^o$	2.53	$Si(OH)_3(OH_2)^+$	2.74
$Al(OH)_4(OH_2)_2^-$	2.373	$Fe(OH)_4^-$	2.34		

hydroxo complex. Previously, protolysis in very acidic solutions ($pH = 0$) was characterized [28,52] by:

$$k = 1.45\,z - 0.45\,h - \frac{1.07\,(2.71 - \chi_M^*)}{\sqrt{\chi_M^*}} \quad (136b)$$

which was based on the mean electronegativity of hydroxyl anion $\chi_{OH}^* = 2.715$. For aluminum ($\chi_{Al}^* = 1.47$, $h = 6$) Eq. (136a) gives $k = 1.72$ ($Al(OH)_2^{+}$) and Eq. (136b) gives $k = 0.56$ ($Al(OH)^{2+}$). As shown in Fig. 31, only aluminum cations Al^{3+} ($k = 0$) exist at $pH < 4$. The prediction of Eq. (136b) is thus closer to reality. Cationic species, which may be found in dilute aqueous solutions are listed in Table 20.

At pH =14 the electronegativity of the hydrated anionic proton complex $[H_7O_4]^-$is 2.334 (2.341). However, $pH = 14$ is not simply inserted into Eq. (135). Instead, the following relation is given in reference [11,28]:

$$k = 1.14\,z_M + 0.250\,h' - \frac{0.836\,(2.341 - \chi_M^*)}{\sqrt{\chi_M^*}} \quad (137)$$

Due to changes in pH the coordination number is suggested to change from $h = 6$ at $pH = 0$ to $h' = 4$ at $pH = 14$. For aluminum, Eq. (137) gives $h' = 3.82$ ($Al(OH)_4^-$). As shown in Fig. 34 aluminum exist, indeed as anionic $[Al(OH)_4]^-$ complex at $pH > 14$. Aquo-oxo-hydroxo ligands are formed (hydrolysis, oxolation) in alkaline solutions through protolysis. They are characterized by:

$$\left[M(OH)_k(OH_2)_{h-k}\right]^{(z-k)+} \Leftrightarrow \left[MO_l(OH)_k(OH_2)_{h-l-k}\right]^{(z-k-2l)+} + 2l\,H^+ \quad (138)$$

where the involvement of water as hydrated proton complexes is omitted for clarity. Electronically protolysis continues in strongly alkaline solutions until the mean electronegativity of aquo-hydroxo species equals the mean electronegativity of water ($\chi_{H_2O}^* = 2.491$, [11,28,51,52]):

$$\chi_{soln} = 2.732 - 0.035\,pH \quad \Leftrightarrow \quad 2.242 < \chi_{soln} < 2.732 \quad (139)$$

At $pH = 7$ $\chi_{H_2O}^* = 2.487$, which is close to electronegativity of water $\chi_{H_2O}^* = 2.491$. At $pH = 14$ protolysis of hydrated aluminium ($\chi_{Al}^* = 1.47$, $h' = 4$) was found to continue until $h' = 3.82$ (Eq. (137)). Metals with a high formal charge ($z_M > 4$) may, however form proton-free oxo-complexes. Neglecting water coordination number, the formation of oxo-hydroxo complexes may be formed by hydrolysis in water as:

$$[MO_l]^{(2l-z)-} + k\,H_2O \Leftrightarrow \left[MO_{l-k}(OH)_k\right]^{(2l-z-k)-} + k\,OH^- \quad (140)$$

In alkaline solutions the complex valence is assumed to be negative. Stable anionic complexes can be characterized [28,51,52] by:

$$k = 1.45\,l - z_M + \frac{0.74\,(2.1 - \chi_M^*)}{\sqrt{\chi_M^*}} \quad (141)$$

where the mean electronegativity of protons is $\chi_H^* = 2.1$. Protolysis will go on as long as $\delta_H < 0$ until $\delta_H = 0$. Such complexes can be found in dilute very alkaline aqueous solutions ($pH = 14$). Assuming that $l = h' = 4$, Eq. (141) predicts that $k = 3.2$. The overall oxo-hydroxo complex reaction may thus be written [28] as:

$$AlO_4^{5-} + 3\,H_2O \Leftrightarrow \left[AlO(OH)_3\right]^{2-} + 3\,OH^- \quad (142)$$

since $l - k = 4 - 3.2 = 0.8$. Experimentally, the only known oxo-hydroxo species are dehydrated Boehmite and Diaspore,*AlOOH*(Table 17). Species such as $AlO(OH)_3^{2-}$, which are predicted by reaction (142) is not found in alkaline aqueous solutions. Only neutral $Al(OH)_3^o$ and $Al(OH)_4^-$ anions as predicted by Eq. (137). Aquo-xo-hydroxo complexes formed according to Eq. (142) by some cations are listed in Table 21.

Fig. 39 illustrates the presence of aquo-, aquo-hydroxo, and hydroxo-oxo species as a function of valence (charge, z_M) and pH.

A low charge promotes aquo complexes in acidic solutions, while a high valence promotes oxo complexes (oxolation) in alkaline solutions. Intermediate charges and pH stabilizes hydroxo complexes (olation). The limiting borders between these ranges are given by k in Eqs. (136a), (136b),(137) and (141).

The partial charge (PCM) model can also be used to evaluate when a neutral form of metal-oxo-hydroxo-aquo complexes (pH_{PZC}) act as strong acids (protolysis) and bases (hydroxolysis).

Acidity test: Assume that the complex $[M(OH)_k(OH_2)_{h-k}]^{(z-k)+}$(Eq. (132)) is neutral ($z_M = k$) and deprotonated producing anions(bases, B^-) as:

$$\left[M(OH)_k(OH_2)_{h-k}\right]^o \leftrightarrow \left[M(OH)_{k+1}(OH_2)_{h-(k+1)}\right]^- + H^+ \quad (143)$$

If electronegativity of the base anion $\chi_{B^-}{}^J > \chi_{H_2O}^* = 2.49$ protolysis occurs, but if $\chi_{B^-}{}^J < \chi_{H_2O}^*$, the proton remains in the stable coordination sphere. The critical threshold electronegativity for an acidic neutral hydrated cation complex [11,28] is:

$$\sqrt{\chi_A'} = -0.136\,(z_M - 4) + \sqrt{2.49 + [0.136\,(z_M - 4)]^2} \quad (144)$$

For Al^{3+} ($z_{Al} = 3$) Eq. (144) results in $\sqrt{\chi_A'} = 1.72 \Rightarrow \chi_A^J = 2.96$. If $\chi_{Al}^* > \chi_A{}^J$then the complex is a strong acid. Since the proton within hydroxyl groups has a very high positive partial charge this leads to protolysis in water. Aluminium ($\chi_{Al}^* = 1.47$) does obviously not alone possess an acidic property. Aqueous species give rise to aquo-ions, which may behave like strong acids. According to the average electronegativities given in Tables 17 and 18, no metal complex exceeds the limiting value (2.96) and therefore they remain stable but depend on the experimental conditions.

Basicity test: Assume that the complex $[M(OH)_k(OH_2)_{h-k}]^{(z-k)+}$(Eq. (132)) is neutral ($z_M = k$) and dehydroxylated to produce cations as:

$$\left[M(OH)_k(OH_2)_{h-k}\right]^o \leftrightarrow \left[M(OH)_{k-1}(OH_2)_{h-(k-1)}\right]^+ + OH^- \quad (145)$$

If electronegativity of the acid cation $\chi_{A^+}{}^J < \chi_{H_2O}^* = 2.49$ hydroxylysis occurs, but if $\chi_{A^+}{}^J > \chi_{H_2O}^*$ the hydroxyl remains stable in the coordination sphere. The critical threshold electronegativity for neutral basic hydrated cation complexes [11,28] is:

$$\sqrt{\chi_B'} = -0.136\,(z+4) + \sqrt{2.49 + [0.136\,(z+4)]^2} \quad (146)$$

Table 20
Aquo-Oxo-hydroxo complexes formed by some cations in dilute acidic-to-neutral aqueous solutions [52,53].

M^{z+}	χ_M^*	h	k	Theoretical	Experimental
Fe^{2+}	1.72	6	< 0	$[Fe(OH_2)_6]^{2+}$	$[Fe(OH_2)_6]^{2+}$
B^{3+}	2.02	3	2.5	$[B(OH)_3]^o$	$[B(OH)_3]^o$
Al^{3+}	1.47	6	0.6	$[Al(OH)(OH_2)_5]^{2+}$	$[Al(OH)(OH_2)_5]^{2+}$
Fe^{3+}	1.72	6	0.8	$[Fe(OH)(OH_2)_5]^{2+}$	$[Fe(OH)(OH_2)_5]^{2+}$
Si^{4+}	1.74	4	3.3	$[Si(OH)_4]^o$	$[Si(OH)_4]^o$
Ti^{4+}	1.32	6	1.9	$[Ti(OH)_2(OH_2)_4]^{2+}$	$[TiO(OH_2)_5]^{2+}$
Zr^{4+}	1.29	8	0.9	$[Zr(OH)(OH_2)_7]^{3+}$	$[Zr(OH)(OH_2)_7]^{3+}$
V^{5+}	1.59	6	3.6	$[V(OH)_4(OH_2)_2]^+$	$[VO_2(OH_2)_4]^+$

Table 21
Aquo-oxo-hydroxo complexes formed by some cations in dilute alkaline aqueous solutions [52,53].

M^{z+}	χ_M^*	h	k	Theoretical	Experimental
Fe^{2+}	1.72	4	4.0	$[Fe(OH)_4]^{2-}$	$[Fe(OH)_4]^{2-}$
B^{3+}	2.02	4	2.8	$[BO_2(OH)_2]^{2-}$	$[B(OH)_4]^-$
Al^{3+}	1.47	4	3.2	$[AlO(OH)_3]^{2-}$	$[Al(OH)_4]^-$
Fe^{3+}	1.72	4	3.0	$[FeO(OH)_3]^{2-}$	$[Fe(OH)_4]^-$
Si^{4+}	1.74	4	2.0	$[SiO_2(OH)_2]^{2-}$	$[SiO_2(OH)_2]^{2-}$
Ti^{4+}	1.32	6	5.2	$[Ti(OH)_6]^{2-}$	
Zr^{4+}	1.29	5	3.8	$[ZrO(OH)_4]^{2-}$	$[Zr(OH)_5]^-$
V^{5+}	1.59	4	1.1	$[VO_3(OH)]^{2-}$	$[VO_3(OH)]^{2-}$

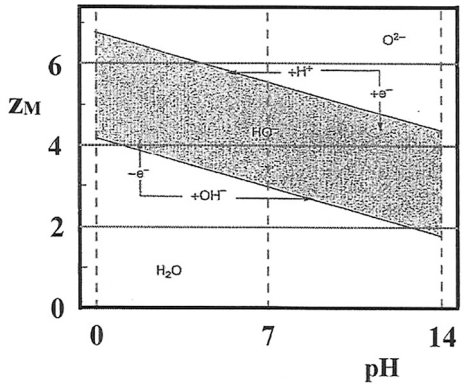

Fig. 39. Expected cation species of valence (charge, *zM*) at different aqueous solution acidities (*pH*) [11,12,52,53]. Aquo complexes form at low cation charge and low *pH*, while highly charged oxo(hydroxo) complexes remain stable at high z_M and *pH*. The boundary for occurrence of mainly aquo-hydroxo complexes (olation) is defined by Eq. (136a) and (136b). The limit for occurrence of oxo-hydroxo complexes (oxolation) is defined by Eqs. (137) and (141).

For Al^{3+} ($z_M = 3$) Eq. (146) results in $\sqrt{\chi_B^J} = 0.89 \Rightarrow \chi_B^* = 0.79$. If $\chi_{Al}{}^* < \chi_B{}^*$ the complex is a strong base and a spontaneous release of hydroxyl groups occur in aqueous solutions. Since only alkaline cations behave in this way, the critical electronegativity is very low and all complexes remain stable. Since a great deal of common solids are cation (metal) (hydr)oxides, the dehydration (precipitation and/or annihilation) of solution species to chargeless solids is of particular interest:

$$XO_l(OH)_k(OH_2)_{h-l-k}^{(z-2l-k)+} \leftrightarrow XO_l(OH)_k \leftrightarrow XO_l \quad (147)$$

In diluted aqueous solutions the aquo-hydroxo-oxo complex may interact unaltered with hydroxylated surface sites and form a cation complex coat in Stern layer.

4.2.3. Summary

Instead of existing as point charges, cations react in reality with water to form hydroxylated (aquo-hydroxo) complexes in acid-to-neutral solutions and deprotonated hydroxyl (oxo-hydroxo) complexes in alkaline solutions. These complexes may interact unaltered with hydrated surface sites and it is very improbable that they are dehydrated upon adsorption. Chemical equilibria provides an excellent mean to characterize this process. Hydrolysis, hydroxyl complexation and acidity equilibrium constants (energies) are offered in Appendix 7 and 8 to quantify these reactions. Hydrolysis constants are successfully correlated to ionic potentials and to cation hydration constants (energies). Multisite complexation (MUSIC) may be used to quantify proton adsorption energy to cations. Using partial charge (PCM) model the *pH* range and extent of cation olation and oxolation can be estimated. As exemplified by Al^{3+} reactions, the PCM model predicted hydroxylation and oxolation with reasonable success.

Table 22
Summary of main cohesive and interaction energies expressed as low < high MJ/mol. Energies are extracted from 22 Tables and 8 Appendices. Top rows characterizes metal hydroxides and metal oxides, while rows below E_g(M) concerns metal cations. ^{A} = acid solutions, ^{a} = absolute/attractive, ^{r} = relative/repulsive, * A = 4.0 nm^2.

	z = 1	z = 1	z = 2	z = 2	z = 3	z = 3	z = 4	z = 4	z = 5
	$M(OH)_z$	M_xO_y	$M(OH)_z$	M_xO_y	$M(OH)_z$	M_xO_y	$M(OH)_z$	M_xO_y	M_xO_y
$\Delta_{lat}D_m$	0.71<1.02	2.13<3.27	2.14<3.48	3.03<4.51	4.71<6.21	12.7<19.1	8.62<10.9	9.63<15.4	32.1<39.0
$\Delta_{elv}D_m$	0.71<1.02	1.07<1.66	1.07<1.74	1.52<2.61	1.48<2.07	2.08<3.18	2.16<2.73	2.45<3.85	3.21<3.90
$\Delta_{Born}D_m$		0.48<0.56		0.98<1.30		1.47<1.98		2.24<2.75	3.27<3.31
$\Delta_{dip}D_m$	0.27<0.56		0.68<1.53		1.32<2.10		2.31<2.80		
$\Delta_{ato}D_m$		0.73<1.17		0.40<1.24		1.46<3.49		0.90<2.78	2.74<4.85
$\Delta_{sie}D_m$	0.33<0.43	0.21<0.34	0.21<0.48	0.24<0.67	0.55	0.21<0.81		0.29<0.88	0.43<0.84
$\Delta_{cov}D_m$		0.55<1.02		0.79<1.12		0.88<1.29		0.86<1.29	1.13<1.21
E_g	0.10	0.11<0.21	0.07<0.27	0.12<0.85	0.12<0.44	0.18<0.85	0.19	0.20<0.88	0.23<0.51
$E_g(R_m)$				0.03<0.06				0.01<0.06	
A_{SGm}				0.03<0.09		0.08<0.09		0.04<0.26	
A_{SWm}				0.01<0.02		0.02<0.03		0.01<0.16	
$\Delta_{sp}D_m$	0.04<0.08		0.03<0.16		0.11<0.26		0.26<0.38		
$\Delta_{dp}{}^AD_m$	-0.05		-0.13<-0.01		-0.12<-0.03				
$\Delta_{PZC}D_m$		0.12	0.09<0.15	0.07<0.14		0.07<0.12		0.02<0.14	0.01<0.06
E_g(M)	0.08<0.63	0.07<0.63	0.02<0.75	0.02<0.75	0.08<0.77	0.08<0.77	0.49<0.77	0.16<0.77	0.57<0.87
$\Delta_{sub}{}^aD_m$	0.05<0.30		0.03<0.75		0.11<0.43				
$\Delta_{sub}{}^rD_m$	-0.15<0.09		-0.32<0.35		-0.49<-0.10				
$\Delta_{ion}{}^aD_m$	0.38<0.74		1.47<2.82		3.46<5.52				
$\Delta_{ion}{}^rD_m$	-0.93<-0.57		-1.14<0.19		-0.48<1.53				
$\Delta_{sol}{}^aD_m$	0.14<0.51		0.30<1.11		0.59<1.50				
$\Delta_{sol}{}^rD_m$	-0.29<0.08		-0.56<0.26		-0.69<0.22				
$\Delta_{hyd}{}^aD_m$	-0.56<-0.31		-2.39<-1.25		-4.66<-3.20		-6.97<-5.82		
$\Delta_{hyd}{}^rD_m$	0.052<0.80		-0.01<0.86		-1.38<0.01				
$\Delta_{DLVO}D_m$	-0.005<0.01								
$\Delta_{vdW}D_m$*	0.001<-0.01								
$\Delta_{rep}D_m$	0.001<0.01								
$\Delta_{str}{}^aD_m$*	0.05<-0.24								
$\Delta_{str}{}^rD_m$*	0.01<0.07								
$\Delta_{dip}D_m$	0.05<0.09								
$\Delta_{ads}D_m$	0.02		-0.06<0.47		-0.13<0.65				
$\Delta_{hi}D_m$	0.07<0.14		0.01<0.28		-0.01<0.21		-0.005<0.01		
$\Delta_{ki}D_m$	0.01<0.03		0.004<0.09		0.02<0.19		0.05<0.30		
$\Delta_{ai}D_m$	0.04<0.06		0.01		0.01<0.08		0.05<0.07		

5. Conclusions

The mutual relationship between solids from which potential determining cations dissolve and (saturated) electrolyte solutions from which solids are precipitated is reviewed and evaluated quantitatively. 42 metal hydroxides and 106 metal oxides were selected as model substances.

Solid cohesion is characterized by lattice, electrovalent, Born and dipolar electrostatic, atomization, Paulings single bond and covalent (bond) energies. Kapustinskiis model was found to be particularly useful when predicting lattice energies. Semi-metals and semiconductors are characterized by electron band gap, Hamaker and van der Waals interaction energies.

Dissolution of potential determining cations into water is characterized by solubility product and dissolution product energies. Borns and Marcusmodels were evaluated for determi-nation of cation hydration energies. Proton association to hydrolyzed surface sites (*pH* dependence) was quantified using Jolivets, Parksand Yoon et.als modifications of multisite complexation (MUSIC) model.

Schulze-Hardy procedure employing Deryagin-Landau-Veerwey-Overbeek (DLOVO) model was used to determine critical distance and electrolyte concentration for diffuse layer stability between two similar blocks in electrolyte solutions. The results were evaluated using simulations of total, attractive and repulsive DLVO interaction energies.

The particular attractive and repulsive structural (solvation) force, the dipolar potential drop and cation adsorption at solid-water interface was quantified and compared to other "bulk" interaction energies.

Cation reactions with water was quantified by hydrolysis, hydroxyl complexation and acid protolysis energies. Multisite complexation (MUSIC) model and partial charge (PCM) model were engaged to quantify proton association and extent of olation and oxolation in neutral, acidic and basic aqueous soltions.

Results are collected in 22 Tables and 8 Appendices. Key properties are mutually correlated in 37 Figs. The cohesive, solid-water interface and cation-water interaction energies are compared to each other (quantified as MJ/mol) in Table 22.

Energies representing solids cohesion are, as expected a decade larger than all other energies. Solids dissolution energies are somewhat larger than interaction energies for low energy solids. The largest cation energies are related to electron exchange in gas phase and in solution. The energies relating to interaction at solid-water interface and to cation-water interaction are very much smaller.

Symbols and abbreviations

A	anion, acid, affinity, Hamaker const.
B	base
C	cation, cohesion
D	energy
E	electronic energy
F	Faraday constant
G	Gibbs free energy
H	enthalpy, hydrogen
I	iconicity
K	global equilibrium constant
M	molar mass, metal
N	number
O	oxygen
P	probe
R	gas constant
S	entropy
T	temperature
NBS	National Bureau of Standards
CFSE	crystal field stabilization energy
Δ	process (final – initial states)
Γ	surface excess
Ψ	complex surface potential
[]	activity, concentration, amount
κ	inverse Debye length
μ	chemical potential
π	3.14…
τ	function
ϕ	Galvani (inner) potential
ψ	surface (Volta) potential
d	molecule diameter
e	unit (electron) charge
g	gas
h	Planckś constant
k	(Boltzmann) costant
l	distance
m	mass (weight)
n	refractive index, amount
p	dipole moment
q	quadrupole constant, charge
r	radius
s	solid
x	number of metals/cations in molec.
y	number of oxygens/anions in mol.
z	number of hydroxyls in molecule
z	valence, charge number
α	polarizability
β	complexation constant
γ	surface/interfacial tension
δ	partial charge
ε	permittivity, dielectric constant
η	metal hardness
θ	surface coverage
λ	molecular distance
ν	number of ions in molecule
σ	surface charge density
υ	formal charge
χ	electronegativity
ω	$1/\eta$ = metal softness

Upper indices

A	acidic, arithmetic
G	geometric
M	Mullikens scale
abs	absolute
b	bulk
cov	covalent
dip	dipolar
elv	electrovalent
gas	gaseous phase
int	intrinsic
ori	oriented
pc	purely covalent
s	surface
z	valence, charge number
1^{st}	first electron transitions
B	base
J	Jolivets scale
P	Paulings scale
ave	average
chem	chemical
d	dispersive
el	electrostatic
eq	equivalent
hs	hydration shell
o	chargeless
p	polar

rel	relative (contemporary)
sie	single
θ	standard (state)
*	Allred-Rochow scale

Lower indices

A	anion, Avogadro
Born	Born model
E	electronic energy
G	gas
L	liquid
M-O	metal-oxide bond
R	(molar) refraction
vdW	van der Waals
ads	adsorption
aff	affinity
aq	(dilute) aqueous
b	blank
c	conduction
cor	corrected
cry	crystal
dip	dipole
dp	dissolution product
eq	equivalent
g	(electron band) gap
hyd	hydration, hydrolysis
ind	induced
lat	lattice
n	coord. number
o	reference state, vacuum
qup	quadrupole
ref	reference
sp	specific, solubility product
str	structural (solvation)
χ	electronegativity
υ	formal valence
A-B	acid-base pair
C	cation, coordination
F	Fermi
Kap	Kapustinskii
M	Madelung, metal
PZC	point of zero charge
S	solid
W	water
acid	acidic
a(n)	acid constant
ato	atomization
bo	bond
cav	cavity
crit	critical
d	dispersion
dis	dissociation
e	electron(ic)
fo	formation
h	numer of coord. water molec.
i	component
ion	ionization
m	coord. number, molar
(m)n	nuber of associated protons
ox	oxidation
red	reduction
ro	red(uction)-ox(idation
sol	solution
sub	sublimation
κ	inverse Debye length, (electron) conductivity

Declaration of Competing Interest

There are no conflicts of interest with coauthors (I am sole contributor) or financial counterparts.

Acknowledgements

This investigation was supported by Academy of Finland funding to Center of Excellence of Functional Materials, Laboratory of Physical Chemistry at Åbo Akademi University.

Appendix 1. Energies of interaction in kJ/mol: $\Delta_{lat} = \Delta_{lat}D_m$ = lattice energy (Eq. (15a)) [1–3], $\Delta_{bo}{}^{elv}D_m$ = electrovalent cohesion (bond) energy (Eq. (15b)), $\Delta_{Kap} = \Delta_{Kap}D_m$ = Kapustinskii crystal energy (Eq. (18b)), $\Delta_{Born} = \Delta_{Born}{}^{el}D_m$ = Born "solids formation" energy (Eq. (19b)), $\Delta_{dip} = \Delta_{dip}{}^{el}D_m$ = charge-dipole energy (Eq. (20b)), $\Delta_{ro} = \Delta_{ro}D_m$ = red-ox gas phase energy (Eqs. (16, 17a)), $\Delta_{ro}{}^{eq}$ = equivalent red-ox gas phase energy (Eq. (17b)), $\Delta_{ato} = \Delta_{ato}D_m$ = atomization energy (Eq. (8)) [1–3], $\Delta_{bo}{}^{ave} = \Delta_{bo}{}^{ave}D_m$ = average bond energy (Eq. (9)), $\Delta_{bo}{}^{sie} = \Delta_{bo}{}^{sie}D_m$ = single bond energy (Eq. (4b)) [8], $\Delta_{bo}{}^{cov} = \Delta_{bo}{}^{cov}D_m$ = covalent bond energy (Eq. (11a),(11b)). Accuracy 2%

M_xO_y	Δ_{lat}	$\Delta_{bo}{}^{elv}$	Δ_{Kap}	Δ_{Born}	Δ_{dip}	Δ_{ro}	$\Delta_{ro}{}^{eq}$	Δ_{ato}	$\Delta_{bo}{}^{ave}$	$\Delta_{bo}{}^{sie}$	$\Delta_{bo}{}^{cov}$
z = 1	$N_e = 1$	ν = 2	$N_{C=}$ 6								
LiOH	1021	1021	955		555	466	466			431	
NaOH	887	887	869		442	445	445			342	
KOH	789	789	772		333	456	456			359	
RbOH	766	766	744		305	461	461			356	
CsOH	721	721	708		273	448	448			373	
TlOH	705	705	744		305	400	400			330	
CuOH	1006	1006	952		550	456	456			406	
AgOH	918	918	832		396	522	522				
z = 1	$N_{e=}$ 2	ν = 3	$N_{C=}$ 6								
Li_2O	2799	1400	2833			1634	817	1165	582	341	799
Na_2O	2481	1241	2581			1601	801	880	440	270	668
K_2O	2238	1119	2294			1450	725	788	394	272	593
Rb_2O	2163	1082	2213			1421	711	742	371	276	564
Cs_2O	2131	1066	2106			1400	700	731	365	293	553
Tl_2O	2659	1351	2213			1867	934	792	396	213	813
Cu_2O	3273	1661	2822	556		2178	1089	1095	547	287	1017

(continued on next page)

(*continued*)

M_xO_y	Δ_{lat}	Δ_{bo}^{elv}	Δ_{Kap}	Δ_{Born}	Δ_{dip}	Δ_{ro}	Δ_{ro}^{eq}	Δ_{ato}	Δ_{bo}^{ave}	Δ_{bo}^{sie}	Δ_{bo}^{cov}
z = 1	$N_e = 1$	$\nu = 2$	$N_{C=}$ 6								
Ag_2O	3002	1527	2470	483		2152	1076	850	425	221	870
z = 2	$N_{e=}$ 2	$\nu = 3$	$N_{C=}$ 6								
$Be(OH)_2$	3477	1739	3189		1525	1952	976			476	
$Mg(OH)_2$	2870	1435	2910		1157	1713	857			349	
$Ca(OH)_2$	2506	1253	2626		899	1607	804			409	
$Sr(OH)_2$	2330	1165	2486		788	1542	771			407	
$Ba(OH)_2$	2142	1071	2383		677	1465	733			443	
$Zn(OH)_2$	2795	1398	2877		1124	1671	836				
$Cd(OH)_2$	2607	1304	2673		939	1668	834				
$Hg(OH)_2$	2669	1335	2608		884	1785	893				
$Sn(OH)_2$	2489	1245	2617		891	1598	799				
$Pb(OH)_2$	2376	1188	2462		770	1606	803				
$Ti(OH)_2$	2953	1477	2760		1015	1938	969				
$Mn(OH)_2$	2909	1455	2792		1043	1866	933				
$Fe(OH)_2$	2653	1327	3014		1263	1390	695				
$Co(OH)_2$	2786	1393	2990		1237	1549	775				
$Ni(OH)_2$	2832	1416	2944		1189	1643	822				
$Pd(OH)_2$	3189	1595	2759		1015	2174	1087			213	
$Cu(OH)_2$	2870	1435	2899		1144	1726	863				
z = 2	$N_{e=}$ 2	$\nu = 2$	$N_{C=}$ 6								
BeO	4514	2257	9712	1298		3342	1671	1172	586	437	1116
MgO	3795	1898	3835	1175		2797	1399	998	499	358	935
CaO	3414	1774	3465	1058		2354	1177	1060	530	383	881
SrO	3217	1609	3282	1008		2215	1108	1002	501	426	835
BaO	3029	1515	3079	977		2048	1024	981	490	562	791
RaO	3145	1573	2968			2191	1096	954	477		798
ZnO	4142	2052	3789	1144		3416	1708	726	363	250	924
CdO	3806	1903	3525			3191	1596	615	308	236	848
HgO	3907	1954	3440			3507	1754	400	200	269	808
GeO	3919	1960	3820			3003	1502	916	458	660	1134
SnO	3652	1847	3452			2817	1409	835	418	528	1056
PbO	3520	1782	3250	1032		2861	1431	659	330	374	978
TiO	3832	1916	3641			2594	1297	1238	619	668	1064
VO	3932	1966	3735			2764	1382	1168	584	637	1111
MnO	3724	1937	3681	1149		2813	1407	911	456	362	1006
FeO	3795	1898	3971	1273		2864	1432	931	466	407	1047
CoO	3837	1919	3940	1250		2926	1463	911	456	385	1047
NiO	3908	1954	3880	1218		2996	1498	912	456	366	1064
PdO	3736	1868	3641			3000	1500	736	368	238	993
PtO	4241	1900	3722			3358	1679	883	441	391	1117
CuO	4135	2608	3820	1232		3391	1696	744	372	284	963
z = 3	$N_{e=}$ 3	$\nu = 4$	$N_{C=}$ 6								
$Al(OH)_3$	5627	1876	6275		2098	3529	1176			547	
$Ga(OH)_3$	5732	1911	6050		1914	3818	1273				
$In(OH)_3$	5280	1760	5667		1624	3656	1219				
$Tl(OH)_3$	5314	1771	5482		1497	3817	1272				
$Sc(OH)_3$	5063	1688	5798		1717	3346	1115				
$Y(OH)_3$	4707	1569	5442		1470	3237	1079				
$Cr(OH)_3$	5556	1852	6075		1932	3624	1208				
$Mn(OH)_3$	6213	2071	6050		1914	4299	1433				
$La(OH)_3$	4443	1481	5197		1316	3127	1042				
z = 3	$N_{e=}$ 6	$\nu = 5$	$N_{C=}$ 6								
B_2O_3	19052	3175	18521			15884	2647	3168	528	809	1289
Al_2O_3	15916	2585	15496	1929		12851	2142	3065	511	502	1100
Ga_2O_3	15590	2600	14950			12224	2037	2366	395	374	1095
In_2O_3	13928	2420	14010			11772	1962	2156	359	346	955
Tl_2O_3	14495	2416	13556			12986	2164	1509	252	213	883
Pb_2O_3	14841	2474	13038			12604	2101	2237	373	374	1104
Sb_2O_3	13865	2311	14167	1779		11862	1977	2003	334	494	1083
Bi_2O_3	13408	2235	12859	1621		11671	1945	1737	290	337	1054
Sc_2O_3	13557	2260	14328			10622	1770	2935	489	671	1001
Y_2O_3	12705	2118	13459	1661		9341	1557	3364	561	714	1059
Ti_2O_3	14149	2358	14661			10946	1824	3203	534	668	1076
V_2O_3	15096	2516	14833			12089	2015	3007	501	637	1120
Cr_2O_3	15276	2546	15008	1866		12600	2100	2676	446	461	1075
Mn_2O_3	15146	3218	14950	1805		12889	2148	2257	376	362	1017
Fe_2O_3	14309	2385	15372	1811		11909	1985	2400	400	407	1069
Rh_2O_3	15172	2529	14661			13031	2172	2141	357	405	1063
Au_2O_3			13704					1456	243	223	1004
La_2O_3	12452	2075	12859	1978		9020	1503	3432	572	798	1067
Ac_2O_3	12573	2096	12473							794	
Ce_2O_3	12661	2110	12949			9169	1528	3490	582	790	1074
Pr_2O_3	12703	2117	13038			9374	1562	3329	555	740	1050
Nd_2O_3	12736	2123	13084			9509	1585	3227	538	703	1036

(*continued on next page*)

(*continued*)

M_xO_y	Δ_{lat}	Δ_{bo}^{elv}	Δ_{Kap}	Δ_{Born}	Δ_{dip}	Δ_{ro}	Δ_{ro}^{eq}	Δ_{ato}	Δ_{bo}^{ave}	Δ_{bo}^{sie}	Δ_{bo}^{cov}
z = 1	$N_e = 1$	$\nu = 2$	$N_{C=}$ 6								
Pm_2O_3	12811	2135	13130			9593	1590	3218	536		1038
Sm_2O_3	12878	2146	13176			9850	1642	3028	505	573	1007
Eu_2O_3	12945	2158	13222			10183	1697	2762	460	473	939
Gd_2O_3	12996	2166	13268			9610	1602	3386	564	715	1090
Tb_2O_3	13071	2179	13363			9692	1615	3379	563	694	1078
Dy_2O_3	13138	2100	13410			9907	1651	3231	539	615	1060
Ho_2O_3	13180	2197	13459			9956	1659	3224	537	606	1066
Er_2O_3	13263	2211	13508			9978	1663	3285	548	606	1083
Tm_2O_3	13322	2220	13556			10197	1700	3125	521	514	1056
Yb_2O_3	13380	2230	13605	1468		10500	1750	2880	480	388	995
Lu_2O_3	13665	2278	13654			9883	1647	3782	630	669	1185
z = 4	$N_{e=}$ 4	$\nu = 5$	$N_{C=}$ 6								
$Sn(OH)_4$	9188	2297	9812		2381	6807	1702				
$Ti(OH)_4$	9456	2364	10166		2603	6853	1713				
$Zr(OH)_4$	8619	2155	9699		2313	6306	1577				
$Mn(OH)_4$	10933	2733	10458		2798	8135	2034				
z = 4	$N_{e=}$ 4	$\nu = 3$	$N_{C=}$ 6								
SiO_2	13125	3281	13084	2349		11313	2828	1812	453	800	1195
GeO_2	12828	3207	12397	2492		11419	2855	1409	352	660	1166
SnO_2	11807	2952	11639	2469		10430	2608	1377	344	528	1128
PbO_2	11217	2804	11250			10251	2563	966	241	374	1033
SeO_2	12447	3112	12550			11508	2877	939	235	430	1179
TeO_2	11353	2838	10503			10337	2584	976	244	377	1088
TiO_2	12150	3038	12054	2747		10240	2560	1910	477	668	1094
ZrO_2	11188	2797	11506	2471		8989	2247	2199	550	766	1157
HfO_2	10752	2688	11551	2529		8442	2111	2310	577	801	1207
VO_2	10644	2661	12150			8920	2230	1724	431	637	1120
CrO_2	12868	3217	12297			11380	2845	1488	372	461	1071
MoO_2	11648	2912	11378	2710		10744	2686	904	226	502	915
MnO_2	12970	3839	12397			11676	2919	1294	323	362	1034
IrO_2			11812					1289	322	414	1149
CuO_2	15390	3847	12550			13201	3300	2189	547	287	1292
CeO_2	9627	2453	10884			8483	2121	1144	286	790	855
ThO_2	10397	2599	10615	2249		7971	1993	2526	631	877	1223
PaO_2	10573	2618	10768							792	
UO_2			10805	2326				2075	519	755	1111
NpO_2	10707	2677	10884							731	
PuO_2	10786	2697	10923							656	
AmO_2	10799	2700	10963							553	
CmO_2	10832	2708	10963							732	
z = 5	$N_{e=}$ 10	$\nu = 7$	$N_{C=}$ 6								
As_2O_5	39000	3900	37212			36222	3622	2778	278	484	1184
Sb_2O_5	35344	3534	35160			32603	3260	2741	274	434	1128
V_2O_5	38733	3873	36013			34905	3491	3828	383	637	1128
Nb_2O_5	33550	3350	34611	3308		28922	2892	4628	463	727	1177
Ta_2O_5	32110	3211	34611	3271		27265	2727	4845	485	839	1213
z = 6	$N_{e=}$ 6	$\nu = 4$	$N_{C=}$ 6								
SeO_3	27802	4634	25947			26685	4448	1117	186	430	1185
CrO_3	29245	4874	25731			27530	4588	1715	286	461	1083
MoO_3	25502	4250	24205			23346	3891	2156	359	502	1149
WO_3			24109	4154				2420	403	720	1200
UO_3			22925					2450	408	755	1112
z = 7	$N_{e=}$ 14	$\nu = 9$	$N_{C=}$ 6								
Re_2O_7			65086					4528	323	627	1220
z = 8	$N_{e=}$ 8	$\nu = 5$	$N_{C=}$ 6								
RuO_4			44362					1807	226	528	1128
OsO_4			43798					2045	256	575	1198

Appendix 2. Paulings and Allred-Rochows electronegativities of elements arranged as a four-block periodic table according to minimum successive orbitals used by elements in their bonding: Elements in S-block use only filled and or empty *s*-orbitals, elements in P-block use filled and/or empty *s*- or *p*-orbitals, elements in D-block use filled and/or empty *s*-, *p*- or *d*-orbitals, elements in F-block use filled and/or empty *s*-, *p*-, *d*- or *f*-orbitals. The G/P symbols in upper left corner of each block represents group and periodicity, respectively

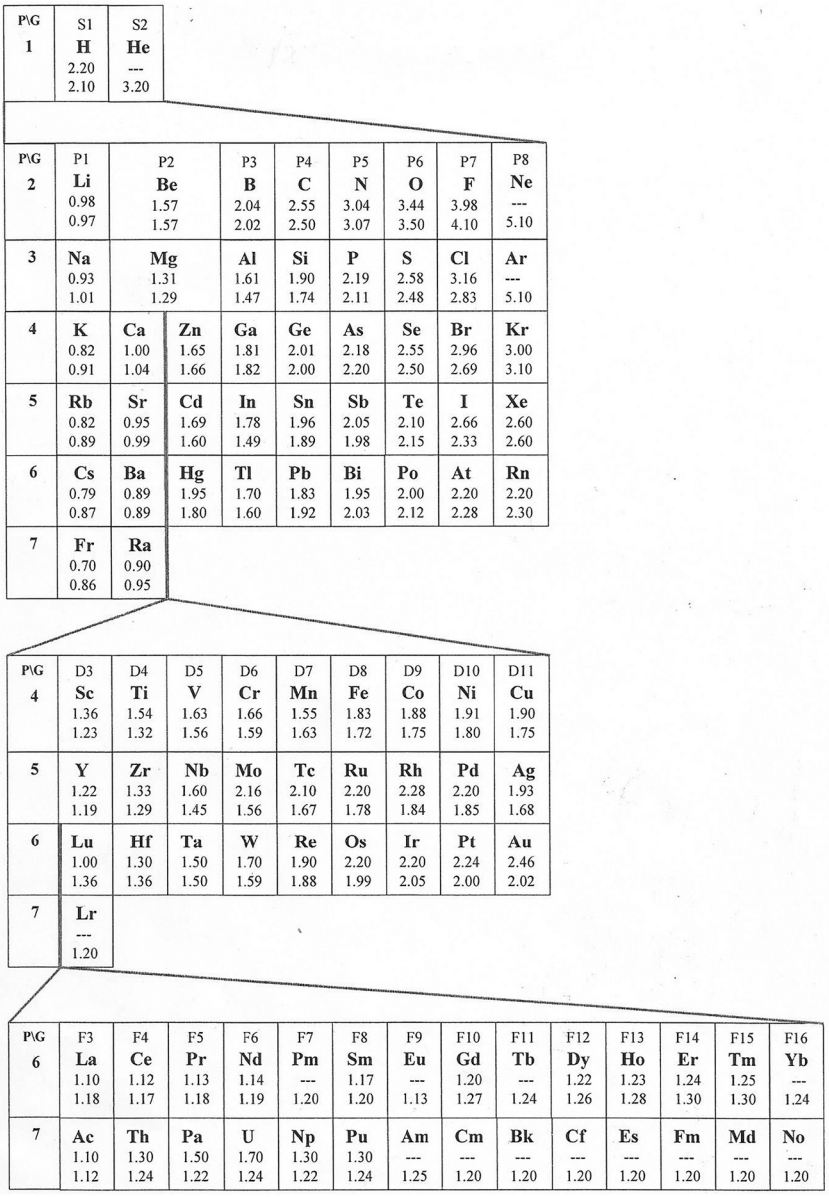

P\G	S1	S2
1	H 2.20 2.10	He --- 3.20

P\G	P1	P2	P3	P4	P5	P6	P7	P8
2	Li 0.98 0.97	Be 1.57 1.57	B 2.04 2.02	C 2.55 2.50	N 3.04 3.07	O 3.44 3.50	F 3.98 4.10	Ne --- 5.10
3	Na 0.93 1.01	Mg 1.31 1.29	Al 1.61 1.47	Si 1.90 1.74	P 2.19 2.11	S 2.58 2.48	Cl 3.16 2.83	Ar --- 5.10

P\G									
4	K 0.82 0.91	Ca 1.00 1.04	Zn 1.65 1.66	Ga 1.81 1.82	Ge 2.01 2.00	As 2.18 2.20	Se 2.55 2.50	Br 2.96 2.69	Kr 3.00 3.10
5	Rb 0.82 0.89	Sr 0.95 0.99	Cd 1.69 1.60	In 1.78 1.49	Sn 1.96 1.89	Sb 2.05 1.98	Te 2.10 2.15	I 2.66 2.33	Xe 2.60 2.60
6	Cs 0.79 0.87	Ba 0.89 0.89	Hg 1.95 1.80	Tl 1.70 1.60	Pb 1.83 1.92	Bi 1.95 2.03	Po 2.00 2.12	At 2.20 2.28	Rn 2.20 2.30
7	Fr 0.70 0.86	Ra 0.90 0.95							

P\G	D3	D4	D5	D6	D7	D8	D9	D10	D11
4	Sc 1.36 1.23	Ti 1.54 1.32	V 1.63 1.56	Cr 1.66 1.59	Mn 1.55 1.63	Fe 1.83 1.72	Co 1.88 1.75	Ni 1.91 1.80	Cu 1.90 1.75
5	Y 1.22 1.19	Zr 1.33 1.29	Nb 1.60 1.45	Mo 2.16 1.56	Tc 2.10 1.67	Ru 2.20 1.78	Rh 2.28 1.84	Pd 2.20 1.85	Ag 1.93 1.68
6	Lu 1.00 1.36	Hf 1.30 1.36	Ta 1.50 1.50	W 1.70 1.59	Re 1.90 1.88	Os 2.20 1.99	Ir 2.20 2.05	Pt 2.24 2.00	Au 2.46 2.02
7	Lr --- 1.20								

P\G	F3	F4	F5	F6	F7	F8	F9	F10	F11	F12	F13	F14	F15	F16
6	La 1.10 1.18	Ce 1.12 1.17	Pr 1.13 1.18	Nd 1.14 1.19	Pm --- 1.20	Sm 1.17 1.20	Eu --- 1.13	Gd 1.20 1.27	Tb --- 1.24	Dy 1.22 1.26	Ho 1.23 1.28	Er 1.24 1.30	Tm 1.25 1.30	Yb --- 1.24
7	Ac 1.10 1.12	Th 1.30 1.24	Pa 1.50 1.22	U 1.70 1.24	Np 1.30 1.22	Pu 1.30 1.24	Am --- 1.25	Cm --- 1.20	Bk --- 1.20	Cf --- 1.20	Es --- 1.20	Fm --- 1.20	Md --- 1.20	No --- 1.20

Appendix 3. Metal (hydr)oxides: Pauling electronegativity differences for single metal-oxide bonds ($\Delta\chi^P = |\chi_M{}^P, -\chi_O{}^P|$, Eq. (3) where $\chi_{OH}{}^P = \chi_O{}^P - \chi_H{}^P = 1.24$) and average Jolivet electronegativity energy for metal (hydr)oxide complexes ($\chi^J = \chi^*(M_xO_y,M(OH)_z$, Eq.(10a), (10b)). Metal cations: First redox ($\chi_{ro}{}^{1st}$, Eq. (12b)) electronegativity and two Mulliken electronegativities derived from Pauling electronegativities ($\chi_1{}^M$ Eq. (14a), $\chi_2{}^M$ Eq. (14b)) [6,7,11]. Electron gap energies (kJ/mol) for metal (hydr)oxides: Published ($E_g{}^{ref}$) and absolute reduction energy ($E_g{}^{abs}$ kJ/mol, Eq. (27a)) based electron gap energies (kJ/mol). Electron gap energies for metal cations: Redox ($E_g{}^{1st}$, Eq. (30)) and relative reduction energy ($E_g{}^{rel}$, Eq. (28b)) based electron gaps. Since only first ionization and affinity energy is considered for neutral metals (M^o), their electron gap (Eg^{1st}) is independent of valence (charge number). For electrochemical processes. $E_g{}^{rel}$ depends on valence, but not whether an oxide or hydroxide is considered. NS = not stable (affinity), NA = not available

$M_xO(H)_y$	$\Delta\chi^P$	χ^J	$E_g{}^{ref}$	$E_g{}^{abs}$	M	$\chi_{ro}{}^{1st}$	$\chi_1{}^M$	$\chi_2{}^M$	$\chi_{ref}{}^M$	$E_g{}^{1st}$	$E_g{}^{rel}$
z = 1	$N_e = 1$	$\nu = 2$									
LiOH	0.26	1.92			Li	1.73	3.54	3.03	1.28	460	431
NaOH	0.31	1.95			Na	1.68	3.39	2.90	1.21	443	405
KOH	0.42	1.88			K	1.56	3.06	2.63	1.03	370	422
RbOH	0.42	1.87			Rb	1.53	3.06	2.63	0.99	356	426
CsOH	0.45	1.85			Cs	1.48	2.97	2.56	0.79	330	430
TlOH	0.46	2.28		102	Tl	1.77	5.69	5.17	2.04	570	84.5

(continued on next page)

(*continued*)

$M_xO(H)_y$	$\Delta\chi^P$	χ^J	E_g^{ref}	E_g^{abs}	M	χ_{ro}^{1st}	χ_1^M	χ_2^M	χ_{ref}^M	E_g^{1st}	E_g^{rel}
z = 1	$N_e = 1$	$\nu = 2$									
CuOH	0.66	2.34			Cu	2.12	6.29	5.87		626	158
AgOH	0.69	2.31			Ag	2.11	6.38	5.98		605	137
z = 1	$N_e = 2$	$\nu = 3$									
Li_2O	2.46	1.50			Li	1.73	3.54	3.03	1.28	460	431
Na_2O	2.51	1.54			Na	1.68	3.39	2.90	1.21	443	405
K_2O	2.62	1.44			K	1.56	3.06	2.63	1.03	370	422
Rb_2O	2.62	1.42			Rb	1.53	3.06	2.63	0.99	356	426
Cs_2O	2,65	1.39			Cs	1.48	2.97	2.56		330	430
Hg_2O	1.49	2.25		222	Hg	NS	6.44	6.05		NS	67.7
Tl_2O	1.74	2.08			Tl	1.77	5.69	5.17	2.04	570	84.5
Cu_2O	1.54	2.21	206	106	Cu	2.12	6.29	5.87		626	158
Ag_2O	1.51	2.15	106	114	Ag	2.11	6.38	5.98		605	137
z = 2	$N_e = 2$	$\nu = 3$									
$Be(OH)_2$	0.33	2.43			Be	NS	5.30	4.75	1.99	NS	481
$Mg(OH)_2$	0.07	2.34		86.8	Mg	NS	4.53	3.94	1.63	NS	561
$Ca(OH)_2$	0.24	2.23		70.4	Ca	1.75	3.60	3.08	1.30	588	637
$Sr(OH)_2$	0.29	2.21		77.4	Sr	1.69	3.45	2.96	1.21	545	642
$Ba(OH)_2$	0.35	2.16		71.9	Ba	1.64	3.27	2.80	0.89	489	644
$Zn(OH)_2$	0.41	2.46			Zn	NS	5.54	5.01		NS	315
$Cd(OH)_2$	0.45	2.44			Cd	NS	5.66	5.14		NS	260
$Hg(OH)_2$	0.71	2.50		272	Hg	NS	6.44	6.05		NS	67.7
$Sn(OH)_2$	0.72	2.52			Sn	2.06	6.47	6.09	1.83	601	219
$Pb(OH)_2$	0.59	2.53			Pb	1.97	6.08	5.62	2.33	681	217
$Ti(OH)_2$	0.30	2.35			Ti	1.86	5.21	4.65		651	447
$Mn(OH)_2$	0.31	2.45		143	Mn	NS	5.24	4.68		NS	379
$Fe(OH)_2$	0.59	2.48			Fe	2.01	6.08	5.62		702	266
$Co(OH)_2$	0.64	2.48		184	Co	2.07	6.23	5.80		697	241
$Ni(OH)_2$	0.67	2.50		185	Ni	2.10	6.32	5.91		626	237
$Pd(OH)_2$	0.96	2.51		224	Pd	2.11	7.18	7.00		750	52.4
$Pt(OH)_2$	1.00	2.55		227	Pt	2.13	7.30	7.16		659	17.3
$Cu(OH)_2$	0.66	2.48		209	Cu	2.12	6.29	5.87		626	146
z = 2	$N_e = 2$	$\nu = 2$									
BeO	1.87	2.34			Be	NS	5.30	4.75	1.99	NS	481
MgO	2.13	2.13	849		Mg	NS	4.53	3.94	1.63	NS	561
CaO	2.44	1.91	637		Ca	1.75	3.60	3.08	1.30	588	637
SrO	2.49	1.86			Sr	1.69	3.45	2.96	1.21	545	642
BaO	2.55	1.77			Ba	1.64	3.27	2.80	0.89	489	644
RaO	2.54	1.82			Ra	1.64	3.30	2.83		500	626
ZnO	1.79	2.41	313		Zn	NS	5.54	5.01		NS	315
CdO	1.75	2.37	212	181	Cd	NS	5.66	5.14		NS	260
HgO	1.49	2.51	222	225	Hg	NS	6.44	6.05		NS	67.7
SiO	1.54	2.47		181	Si	2.18	6.29	5.87	2.03	653	
GeO	1.43	2.65			Ge	2.14	6.62	6.27	1.95	644	161
SnO	1.48	2.57	405		Sn	2.06	6.47	6.09	1.83	601	219
PbO	1.61	2.59	222	191	Pb	1.97	6.08	5.62	2.33	681	217
TiO	1.90	2.15			Ti	1.86	5.21	4.65		651	447
VO	1.81	2.34			V	1.91	5.48	4.94		600	378
NbO	1.84	2.25		184	Nb	1.96	5.39	4.84			566
MnO	1.89	2.39			Mn	NS	5.24	4.68		NS	379
FeO	1.61	2.45	232		Fe	2.01	6.08	5.62		702	266
CoO	1.56	2.48			Co	2.07	6.23	5.80		697	241
NiO	1.53	2.51	241		Ni	2.10	6.32	5.91		625	237
PdO	1.24	2.55			Pd	2.11	7.18	7.00		750	52.4
PtO	1.20	2.65			Pt	2.35	7.30	7.16		659	17.3
CuO	1.54	2.48	147		Cu	2.12	6.29	5.87		626	146
z = 3	$N_e = 3$	$\nu = 4$									
$B(OH)_3$	0.80	2.60		266	B	2.07	6.70	6.38	1.83	774	
$Al(OH)_3$	0.37	2.49		159	Al	1.79	5.42	4.88	1.37	536	579
$Ga(OH)_3$	0.57	2.56			Ga	1.79	6.02	5.55	1.34	537	324
$In(OH)_3$	0.54	2.49		257	In	1.74	5.93	5.45	1.30	529	276
$Tl(OH)_3$	0.46	2.51			Tl	1.77	5.69	5.17	2.04	570	84.5
$Sc(OH)_3$	0.12	2.42			Sc	1.84	4.68	4.09		615	675
$Y(OH)_3$	0.02	2.41			Y	1.81	4.26	3.68		474	742
$Cr(OH)_3$	0.42	2.51		220	Cr	1.93	5.57	5.04		589	369
$Mn(OH)_3$	0.31	2.52			Mn	NS	5.24	4.68		NS	
$Au(OH)_3$	1.22	2.60		438	Au	2.40	7.96	8.05		667	
$La(OH)_3$	0.14	2.40		115	La	1.74	3.90	3.35		493	744
z = 3	$N_e = 6$	$\nu = 5$									
B_2O_3	1.40	2.81			B	2.07	6.70	6.38	1.83	774	
Al_2O_3	1.83	2.47	675		Al	1.79	5.42	4.88	1.37	536	579
Ga_2O_3	1.63	2.69	424		Ga	1.79	6.02	5.55	1.34	537	324
In_2O_3	1.66	2.49	270	292	In	1.74	5.93	5.45	1.30	529	276
Tl_2O_3	1.74	2.56			Tl	1.77	5.69	5.17	2.04	570	84.5
Pb_2O_3	1.61	2.75			Pb	1.97	6.08	5.62		680	

(*continued on next page*)

(*continued*)

$M_xO(H)_y$	$\Delta\chi^P$	χ^J	E_g^{ref}	E_g^{abs}	M	χ_{ro}^{1st}	χ_1^M	χ_2^M	χ_{ref}^M	E_g^{1st}	E_g^{rel}
z = 1	$N_e = 1$	$\nu = 2$									
As_2O_3	1.26	2.91		339	As	2.30	7.12	6.92	2.26	866	
Sb_2O_3	1.39	2.79	332	336	Sb	2.20	6.73	6.42	2.06	730	
Bi_2O_3	1.49	2.82	260	313	Bi	2.03	6.44	6.05	2.02	612	127
Sc_2O_3	2.08	2.30			Sc	1.84	4.68	4.09		615	675
Y_2O_3	2.22	2.27	579		Y	1.81	4.26	3.68		474	742
Ti_2O_3	1.90	2.37			Ti	1.86	5.21	4.65		651	512
V_2O_3	1.81	2.53			V	1.91	5.48	4.94		600	378
Cr_2O_3	1.78	2.55			Cr	1.93	5.57	5.04		589	369
Mn_2O_3	1.89	2.58			Mn	NS	5.24	4.68		NS	
Fe_2O_3	1.61	2.63	215		Fe	2.01	6.08	5.62		703	206
Rh_2O_3	1.16	2.71			Rh	2.07	7.42	7.31		610	23.9
Ir_2O_3	1.24	2.83		334	Ir	2.30	7.18	7.00		714	
Au_2O_3	0.98	2.81			Au	2.40	7.96	8.05		667	
La_2O_3	2.34	2.27	579		La	1.74	3.90	3.35		493	744
Ac_2O_3	2.34	2.22			Ac	1.66	3.90	3.35		465	
Ce_2O_3	2.32	2.26			Ce	1.80	3.96	3.40		442	
Pr_2O_3	2.31	2.27			Pr	1.79	3.37	3.43		435	
Nd_2O_3	2.30	2.27			Nd	NA	4.02	3.46			
Pm_2O_3	2.28	2.28			Pm	NA	NA	NA			
Sm_2O_3	2.27	2.28			Sm	NA	4.11	3.54			
Eu_2O_3	2.35	2.23			Eu	1.81	NA	NA		464	
Gd_2O_3	2.24	2.33			Gd	NA	4.20	3.63			
Tb_2O_3	2.24	2.31			Tb	NA	NA	NA			
Dy_2O_3	2.22	2.33			Dy	NA	4.26	3.68			
Ho_2O_3	2.21	2.34			Ho	NA	4.29	3.71			
Er_2O_3	2.20	2.35			Er	NA	4.32	3.74			
Tm_2O_3	2.19	2.36			Tm	1.90	4.35	3.77		498	
Yb_2O_3	2.24	2.31			Yb	1.77	NA	NA		605	
Lu_2O_3	2.44	2.40			Lu	1.70	3.60	3.08		491	
z = 4	$N_{e=} 4$	$\nu = 5$									
$Sn(OH)_4$	0.72	2.60			Sn	2.06	6.47	6.09	1.83	601	
$Ti(OH)_4$	0.30	2.50			Ti	1.86	5.21	4.65		651	
$Zr(OH)_4$	0.09	2.50			Zr	1.88	4.59	4.00		599	642
$Mn(OH)_4$	0.31	2.56			Mn	NS	5.24	4.68		NS	
$Th(OH)_4$	0.06	2.48		194	Th	NA	4.50	3.91		NS	772
z = 4	$N_{e=} 4$	$\nu = 3$									
SiO_2	1.54	2.77	839	525	Si	2.18	6.29	5.87	2.03	653	
GeO_2	1.43	2.90			Ge	2.14	6.62	6.27	1.95	643	160
SnO_2	1.48	2.85	336	388	Sn	2.06	6.47	6.09	1.83	601	
PbO_2	1.61	2.86			Pb	1.97	6.08	5.62	2.33	681	
SeO_2	0.89	3.13			Se	2.43	8.23	8.44	2.51	746	
TeO_2	1.34	2.97		499	Te	2.34	6.88	6.61	2.34	679	
TiO_2	1.90	2.53	298		Ti	1.86	5.21	4.65		651	
ZrO_2	2.11	2.51	385		Zr	1.88	4.59	4.00		599	642
HfO_2	2.14	2.55	560	291	Hf	1.85	4.50	3.91		659	672
VO_2	1.81	2.67			V	1.91	5.48	4.94		600	
NbO_2	1.84	2.61		372	Nb	1.96	5.39	4.84		566	
CrO_2	1.78	2.69			Cr	1.93	5.57	5.04		589	
MoO_2	1.28	2.67		425	Mo	1.98	7.06	6.84		612	
MnO_2	1.89	2.71	26		Mn	NS	5.24	4.68		NS	
ReO_2	1.54	2.84		465	Re	2.00	6.29	5.87		741	
IrO_2	1.24	2.93			Ir	2.30	7.18	7.00		714	
PtO_2	1.20	2.90		341	Pt	2.35	7.30	7.16		659	
CuO_2	1.54	2.78			Cu	2.12	6.29	5.87		626	
CeO_2	2.32	2.42	284		Ce	1.80	3.96	3.40		442	
ThO_2	2.14	2.48		263	Th	NA	4.50	3.91		NS	772
PaO_2	1.94	2.47			Pa	NA	5.09	4.52			654
UO_2	1.74	2.48			U	NA	5.69	5.17			
NpO_2	2.14	2.47			Np	NA	4.50	3.91			
PuO_2	2.14	2.48			Pu	NA	4.50	3.91			
AmO_2	2.14	2.49			Am	NA	NA	NA			
CmO_2	2.14	2.46			Cm	NA	NA	NA			
z = 5	$N_e = 10$	$\nu = 7$									
As_2O_5	1.26	3.07			As	2.30	7.12	6.92	2.26	866	
Sb_2O_5	1.39	2.97			Sb	2.20	6.73	6.42	2.06	730	
V_2O_5	1.81	2.78	248	536	V	1.91	5.48	4.94		600	
Nb_2O_5	1.84	2.73	511	511	Nb	1.96	5.39	4.84		566	
Ta_2O_5	1.94	2.75	439	504	Ta	1.98	5.09	4.52		697	
z = 6	$N_e = 6$	$\nu = 4$									
SeO_3	0.89	3.21			Se	2.43	8.23	8.44	2.51	746	
CrO_3	1.78	2.87			Cr	1.93	5.57	5.04		589	
MoO_3	1.28	2.86		672	Mo	1.98	7.06	6.84		612	
WO_3	1.74	2.87	266		W	2.08	5.69	5.17		680	
UO_3	1.74	2.70			U	NA	5.69	5.17			

(*continued on next page*)

(*continued*)

$M_xO(H)_y$	$\Delta\chi^P$	χ^J	E_g^{ref}	E_g^{abs}	M	χ_{ro}^{1st}	χ_1^M	χ_2^M	χ_{ref}^M	E_g^{1st}	E_g^{rel}
z = 1	$N_e = 1$	$\nu = 2$									
z = 7	$N_e = 14$	$\nu = 9$									
Re_2O_7	1.54	3.05			Re	2.00	6.29	5.87		741	
z = 8	$N_e = 8$	$\nu = 5$									
RuO_4	1.24	3.06		1087	Ru	2.05	7.18	7.00		609	
OsO_4	1.24	3.12		1047	Os	2.18	7.18	7.00		708	

Appendix 4. Negative logarithmic solubility products (pK_{sp}, Eq.(40a) and dissolution product quotients/ constants (pK_{dp}, Eqs.(41a)-(41c)) for dissolving solid metal hydroxides, oxohydroxides in neutral, acidic or alkaline solutions to liberate cations [8,25,26]. Note that $pK_{dp}{}^B = pK_{sp}$. The influence of electrolytes is specified only for some solubility products as lower indices 0 and 0.1, which indicate ionic strength. [a]) 8W-hydrate,*pΔ(S-L), Eq.(42)*. Upper index A = acidic and B =basic (alkaline) solutions

	$M(OH)_0$	$M(OH)_{0.1}$	$M(OH)_k$	$M(OH)_k$	$MO_l(OH)_k$	M_mO_l	pΔ(S-L)
z = 1							
Cu		14.0		^{A}-8.64		^{A}-7.6, ^{B}14.8	
Ag	7.7		7.7			^{A}-6.29, ^{B}7.7	
z = 2							
Be	17.7	17.3	21.2	^{A}-6.69		^{A}-6.69	6.96
Mg	10.7	10.4	11.2	^{A}-16.84, ^{B}11.2			
Ca	5.3	4.9	5.3	^{A}-22.80, ^{B}5.2			
Ba			^{a}3.6				
Zn	16.9		16.5			^{A}-11.4	
Cd	14.2	13.8	14.1	^{A}-13.65			6.7
Hg	25.4	25.0				^{A}-2.56	3.8
Ge							3.7
Sn	28.1	27.7	26.3			^{A}-1.76	
Pb	16.1	15.7	19.8			^{A}-12.7	
Cr	17.0	16.6					
Mn	12.7	12.3	13.0	^{A}-15.2, ^{B}12.8			
Fe	15.1	14.7	16.3	^{A}-12.8, ^{B}15.2			
Co	15.7	15.3	14.2	^{A}-12.3			
Ni	17.2	16.8	15.3	^{A}-10.8		^{B}15.7	7.0
Cu	18.6	18.2	20.0	^{A}-8.64		^{A}-7.62	
Pd				^{A}0.6			5.4
z = 3							
Al	33.5		32.0	^{A}-8.5			
Ga	36.5	35.7	35.1	^{B}37.0	^{A}-2.9, ^{B}39.1		7.4
In	35.0			^{A}-5.1, ^{B}36.9		^{A}-6.7, ^{B}35.3	7.3
Tl	45.2		43.8			^{A}3 .9	
Bi						^{A}-3.5	
Sc	30.1		30.7	^{B}-31.3	^{A}-9.4	^{B}36.3	7.0
Y		22.8	22.0	^{A}-17.5			8.5
Lu				^{A}-14.5			
Cr	31.0			^{A}-12.0, ^{B}30.0			
Fe	38.6	37.9	38.6		^{A}-0.5	^{A}-12.0	
Co	44.5	43.8					
Au		45.6		^{A}-5.5, ^{B}2.6			5.5
La	20.0			^{A}-20.3			
Ac				^{A}-21.1, ^{B}20.9			
Ce	20.2	19.5		^{A}-19.9			
Pr			23.5	^{A}-19.5			
Nd				^{A}-18.6			7.9
Sm				^{A}-16.5			
Eu			26.0	^{A}-17.5			
Gd				^{A}-15.6			9.6
Tb				^{A}-16.5			
Dy				^{A}-15.9			8.8
Ho				^{A}-15.4			
Er				^{A}-15.0			9.2
Tm				^{A}-15.0			
Yb				^{A}-14.7			9.4
z = 4							
Pb	66.5					^{B}64.0	
Si						^{A}4.0	
Sn	56.0					^{A}8.4	
Ti		28.6				^{B}29.0	5.5
Zr		47.0				^{A}1.9 ^{B}48.2	
Hf						^{A}1.2	
Ce		50.4				^{A}8.2	
Th	44.9	44.0				^{A}-6.3	
Pa						^{A}-0.6	

(*continued on next page*)

(*continued*)

	$M(OH)_0$	$M(OH)_{0.1}$	$M(OH)_k$	$M(OH)_k$	$MO_l(OH)_k$	M_mO_l	pΔ(S-L)
U						[A]1.8	
Np						[A]4.0	
Pu				[B]19.7	[A]-5.4	[A]6.5	
z = 5							
z = 6							
U		21.6			[A]-5.6	[B]22.0	

Appendix 5. Parks' ($z_M/l_{2HO\text{-}M}$, [31,32]) and Yoon et.al's ($\upsilon_M/l_{HO\text{-}OM}$, [35]) model predictions of point of zero charges (experimental, calculated (Eq. (52c)) and reference [33,34]) for some metal oxides and metal hydroxides. C = crystal field stabilization energy [31,35]

	N_C	$z_M/l_{2HO\text{-}M}$	$\upsilon_M/l_{HO\text{-}OM}$	C	$(\upsilon/l)_{eff}$	pH_{calc}	pH_{exp}	pH_{ref}
z = 1								
Cu_2O		12.95						10,6
z = 2								
$Mg(OH)_2$	6		0.1086			12.31	12.0	13,6
$Zn(OH)_2$	4		0.1689			9.22	7.8	
$Fe(OH)_2$	6	0.587					10.0	
$Fe(OH)_2$	6		0.1068	75.3	0.1169	11.87	12.0	
$Co(OH)_2$	6	0.580					11.0	11,4
$Co(OH)_2$	6		0.1072	138	0.1257	11.40	11.4	11,4
$Ni(OH)_2$	6	0.573					11.5	11,2
$Ni(OH)_2$	6		0.1093	176	0.1329	11.02	11.1	11,2
$Cu(OH)_2$	4		0.1698	163	0.1917	8.01	7.7	10,1
BeO	4		0.1880	0		8.20	10.2	7,1
MgO	6	0.568					12.0	10,7
MgO	6		0.1070	0		12.40	12.4	10,7
ZnO	4	0.588					9.2	9,0
ZnO	4		0.1673	0		9.30	9.3	9,0
CdO	6	0.533					10.5	10,6
HgO	6		0.0931	0		13.4	7.3	5,8
PbO	6	0.501					10.7	11,2
CuO	4	0.567					9.0	
CuO	4		0.1689	163	0.1908	8.06	9.4	
z = 2.7								
Fe_3O_4	6	0.790					8.0	6,9
Co_3O_4	6	0.785					7.5	11,3
z = 3								
G-$Al(OH)_3$	6		0.1724	0		9.03	5.1	9,7
αAlO(OH)	6		0.1698	0		9.17	7.7	9,4
γAlO(OH)	6		0.1711	0		9.10	7.5	9,5
αFeO(OH)	6					7.47	7.6	8,6
αFeO(OH)	6		0.1693	0		9.48	6.7	8,6
γFeO(OH)	6		0.1661	0		9.37	7.4	8,6
αAl_2O_3	6					9.10	9.1	9,0
αAl_2O_3	6		0.1712	0		9.10	9.1	9,0
γAl_2O_3	6					8.47	8.5	8,9
Al_2O_3	6	0.898					9.0	9,0
Ga_2O_3	6	0.877					9.0	7,2
In_2O_3	6	0.833					9.0	7,4
Tl_2O_3	6	0.813					7.9	
Bi_2O_3	6	0.783					9.0	9,3
Y_2O_3	6	0.875					9.0	8,6
Y_2O_3	6		0.1520	0		10.12	9.0	8,6
Cr_2O_3	6	0.896					8.3	6,6
Cr_2O_3	6		0.1664	293	0.2057	7.26	7.0	6,6
αFe_2O_3	6					9.48	9,3	9,2
αFe_2O_3	6		0.1645	0		9.45	9.0	9,2
Fe_2O_3	6	0.896					9.1	
La_2O_3	6		0.1449	0		10.49	10.4	9,4
z = 4								
SiO_2	4					2.97	3.0	2,98
SiO_2	4	1.307					2.0	3,05
SiO_2	4		0.3817	0		-1.85	1.8	3,05
SnO_2	6					5.46	5.5	5,5
SnO_2	6	1.146					4.5	5,4
SnO_2	6		0.2177	0		6.71	6.6	4,2
PbO_2	6	1.117					8.3	9,2
TiO_2	6					5.90	6.0	5,9
TiO_2	6	1.173					6.0	5,7
TiO_2	6		0.2245	0		6.35	6.7	5,9
ZrO_2	8	1.087					6.5	6,3
ZrO_2	8		0.1529	0		12.07	10.5	7,0

(*continued on next page*)

(*continued*)

	N_C	$z_M/l_{2HO\text{-}M}$	$\upsilon_M/l_{HO\text{-}OM}$	C	$(\upsilon/l)_{eff}$	pH_{calc}	pH_{exp}	pH_{ref}
HfO_2	6	1.140					7.5	7,6
RuO_2	6	1.170					5.0	5,8
CeO_2	6	1.090					7.5	8,1
ThO_2	8	1.028					9.0	6,6
ThO_2	8		0.1456	0		10.46	9.15	6,6
UO_2	6	1.084					5.8	5,2
PuO_2	8	1.093					9.0	
PuO_2	8		0.1492	0		10.27	9.0	
z = 5								
V_2O_5	6	1.497					1.0	1,4
Nb_2O_5	6	1.453					4.0	4,3
Ta_2O_5	6	1.453					5.3	3,8
z = 6								
WO_3	6	1.765					1.5	1,7
WO_3	6		0.3405	0		0.34	0.5	1,7

Appendix 6. Absolute (Abs) and relative (Rel) standard free energies (kJ/mol) of cation hydration ($\Delta_{hyd} = \Delta_{hyd}G_m$) calculated from corresponding energy of sublimation ($\Delta_{sub} = \Delta_{sub}G_m$), energy of ionization/oxidation ($\Delta_{ion} = \Delta_{ion}G_m$) and energy of solution ($\Delta_{sol} = \Delta_{sol}G_m$) [8,9,18,38–40]. References: This work $\Delta_{hyd}G_m(H^+) = -1086.9$ kJ/mol, [39] $\Delta_{hyd}G_m(H^+) = -1100$ kJ/mol, [9] $\Delta_{hyd}G_m(H^+) = -1051.4$ kJ/mol

Abs	Δ_{sub}^{abs}	Δ_{ion}^{abs}	Δ_{sol}^{abs}	Δ_{hyd}^{abs}	Δ_{hyd}^{ref}	Δ_{hyd}^{ref}
z = 1						
H	203	1312	428	-1087	-1050	
Li	127	520	135	-512	-475	
Na	77.0	496	167	-406	-365	
K	60.5	419	145	-334	-295	
Rb	53.1	403	144	-312	-275	
Cs	49.6	376	136	-289	-250	
Tl	147	589	396	-341	-300	
Cu	298	746	478	-565	-525	
Ag	246	731	506	-472	-430	
z = 2						
Be	287	2658	477	-2466	-2395	-2483
Mg	113	2189	402	-1899	-1830	-1918
Ca	144	1735	303	-1576	-1505	-1593
Sr	131	1614	297	-1447	-1380	-1470
Ba	146	1468	296	-1318	-1250	-1338
Ra	130	1488	295	-1323	-1250	-1338
Zn	94.8	2640	710	-2025	-1955	-2043
Cd	90.5	2499	779	-1811	-1755	-1843
Hg	31.8	2817	1021	-1828	-1760	-1848
Ge	331	2300	903	-1728		
Sn	266	2120	830	-1557	-1490	-1578
Pb	162	2166	832	-1496	-1425	-1513
Ti	428	1969	542	-1855		-1887
V	754	2061	630	-2186	-1825	-1913
Mn	239	2226	629	-1836	-1760	-1848
Fe	371	2324	778	-1917	-1840	-1928
Co	380	2409	802	-1987	-1915	-2003
Ni	385	2490	811	-2064	-1980	-2068
Pd	340	2679	1033	-1986	-1910	-1998
Pt	521	2656	1112	-2064	-1960	-2048
Cu	289	2703	922	-2079	-2010	-2086
z = 3						
Al	289	5139	800	-4628	-4525	-4657
Ga	234	5521	1126	-4629	-4515	
In	209	5084	1187	-4105	-3980	-4112
Tl	147	5439	1500	-4086	-3970	
Bi	168	4781	1368	-3581	-3480	-3612
Sc	336	4257	759	-3834	-3795	-3927
Y	381	3759	591	-3549	-3450	
Ti	428	4621	889	-4161	-4015	-4147
Cr	352	5231	1070	-4513	-4010	-4536
Fe	371	5282	1281	-4372	-4265	-4383
Rh	511	5461	1066	-4906		
La	394	3456	602	-3248	-3145	-3277
Ce	385	3530	613	-3302	-3200	-3332
Pr	321	3632	606	-3347	-3245	-3377
Nd	292	3700	614	-3379	-3280	-3412
Sm	173	3870	619	-3425	-3325	-3456

(*continued on next page*)

(*continued*)

Abs	Δ_{sub}^{abs}	Δ_{ion}^{abs}	Δ_{sol}^{abs}	Δ_{hyd}^{abs}	Δ_{hyd}^{ref}	Δ_{hyd}^{ref}
Eu	142	4037	711	-3468	-3360	-3476
Gd	360	3750	624	-3486	-3375	
Tb	350	3791	633	-3508	-3400	
Dy	254	3899	620	-3533	-3425	-3557
Ho	265	3923	612	-3577	-3470	-3602
Er	281	3935	616	-3599	-3495	-3627
Tm	198	4044	623	-3619	-3515	-3647
Yb	118	4195	641	-3673	-3570	-3688
Lu	388	3887	657	-3618	-3515	

Rel	Δ_{sub}^{rel}	Δ_{ion}^{rel}	Δ_{sol}^{rel}	Δ_{hyd}^{rel}	Δ_{hyd}^{ref}
z = 1					
H	0	0	0	0	0
Li	-76.7	-792	-293	575	579
Na	-126	-816	-262	681	679
K	-143	-893	-283	753	751
Rb	-150	-909	-284	775	774
Cs	-154	-936	-292	798	806
Tl	-55.9	-723	-32.4	746	
Cu	94.4	-567	50.0	522	
Ag	42.7	-581	77.1	615	611
z = 2					
Be	-120	32.7	-380	-292	-289
Mg	-294	-436	-455	275	278
Ca	-263	-889	-554	598	601
Sr	-276	-1010	-560	727	730
Ba	-261	-1156	-561	856	857
Ra	-277	-1137	-562	851	
Zn	-312	15.7	-147	149	152
Cd	-316	-125	-77.6	363	380
Hg	-375	193	164	346	350
Ge	-75.4	-324	46.3	446	
Sn	-140	-504	-27.2	617	619
Pb	-244	-458	-24.4	678	682
Ti	21.8	-655	-315	319	
V	348	-563	-227	-11.9	
Mn	-168	-398	-228	338	341
Fe	-35.9	-300	-78.9	257	251
Co	-26.3	-215	-54.4	187	192
Ni	-22.1	-134	-45.6	110	113
Pd	-66.9	55.1	177	188	
Pt	114	31.5	255	109	
Cu	-109	79.4	65.5	95.0	100
z = 3					
Al	-321	1203	-485	-1377	-1362
Ga	-376	1585	-159	-1368	
In	-401	1148	-98.0	-844	-821
Tl	-463	1503	215	-826	
Bi	-442	845	82.8	-320	
Sc	-274	321	-527	-574	-633
Y	-229	-177	-694	-288	
Ti	-182	685	-397	-900	
Cr	-258	1295	-215	-1252	-1231
Fe	-240	1346	-4.7	-1111	-1116
Rh	-99.1	1525	210	-1645	
La	-216	-481	-684	13.1	
Ce	-225	-406	-672	-41.2	
Pr	-289	-304	-679	-86.5	
Nd	-318	-236	-672	-118	
Sm	-437	-65.6	-667	-164	
Eu	-468	101	-574	-207	
Gd	-250	-186	-661	-225	
Tb	-260	-145	-652	-247	
Dy	-356	-37.1	-665	-272	
Ho	-345	-12.7	-673	-316	
Er	-329	-1.5	-669	-338	
Tm	-412	108	-662	-358	
Yb	-492	259	-644	-412	
Lu	-222	-49.0	-628	-357	

$\Delta_{hyd}G_m$: Hf^{4+} −6965, Zr^{4+} −6790, Ce^{4+} −6120, Pu^{4+} −6560, U^{4+} −6360, Th^{4+} −5815

Appendix 7. Cumulative logarithmic hydrolysis constants (pK_{hi}) and logarithmic hydroxide complexation constants (pK_{ki}) of cations [25,26]. * *pQ* (based on concentrations), ¤ based on hydrolysis of metal hydroxides

	pK_{h1}	pK_{h2}	pK_{h3}	pK_{h4}	pK_{h5}	pK_{h6}	$LogK_{k1}$	$logK_{k2}$	$logK_{k3}$	$logK_{k4}$
z = 1										
Li	13.6						0.2			
Na	14.2						-0.7			
K	14.5									
Tl	13.2						0.8			
Ag	12.0	24.0					2.3	3.6	4.8	
z = 2										
Be	5.4	13.7	23.3	37.4				3.1		
Mg*	11.4						2.6			
Ca	12.9						1.3			
Sr	13.3						0.8			
Ba	13.5						0.7			
Zn	9.0	16.9	28.4	41.2			4.4		14.4	15.5
Cd	10.1	20.4	33.3	47.4			4.3	7.7	10.3	12.0
Hg	3.4	6.2	21.1				10.3	21.7		
Sn	3.4	7.1	16.6				10.1			
Pb	7.7	17.1	28.1				6.2	10.3	13.3	
Cr	3.7	4.0								
Mn	10.6	22.2	34.8	48.3			3.4			
Fe	9.5	20.6	31.0	46.0			4.5			
Co	9.7	18.8	31.5	46.3			5.1			
Ni	9.9	19.0	30.0	44.4			4.6			
Pd*	2.3	4.8								
Cu	8.0	17.3	27.8	39.6			6.0			
z = 3										
B¤	9,2									
Al	5.0	9.3	15.0	23.0						33.3
Ga	2.6	5.9	10.3	16.6			11.1			
In	4.0	7.8	12.4	22.1			7.0			
Tl	0.6	1.6	3.3	15.0			12.9	25.4		
As*¤				9.3						
Sb¤		-1.4		11.8		2.7				
Bi	1.1	4.0	8.9	21.8			12.4			
Sc	4.3	9.7	16.1	26.0			9.1	18.4		
Y*	7.7	16.4	26	36.5						
Lu*	7.6									
Ti*¤	2.2		2.3	4.8			11.8			
V	2.3									
Cr	4.0	9.7	18.0	27.4			10.2	18.3		
Mn*	-0.7									
Fe	2.2	5.7	12.0	21.6			11.0	21.7		
Rh	3.4									
Au	-1.51	-1.0	4.0	11.8	25.1	41.1				
La*	8.5						3.9			
Ac*	10.4									
Ce*	8.3						5.0			
Pr*	8.1									
Nd*	8.0	16.9	26.5	37.1						
Sm*	7.9									
Eu*	7.8									
Gd*	8.0	16.4	25.2	34.4						
Tb*	7.9									
Dy*	8.0	16.2	24.7	33.5						
Ho*	8.0									
Er*	7.9	15.9	24.2	32.6						
Tm*	7.7									
Yb*	7.7	15.8	24.1	32.7						
z = 4										
Si¤										
Ge¤										
Ti										
Zr	-0.3	1.7	5.1	9.7	16.0		13.8	27.2	40.2	53.0
Hf	0.3	2.4	6.0	10.7	17.2					
Ce*	1.1	0.3					13.3	27.1		
Th	3.2	6.9	11.7	15.9			9.7			
Pa	-0.8	0.0	1.5							
U	0.7	2.6	5.8	10.3	16.0					
Np	1.5									
Pu	0.5	2.3	5.3	9.5	15.0					
z = 5										
Sb¤			-1.4		11.8	2.7				
Nb¤					-0.6	7.4				
Ta¤					1.0	9.6				

Appendix 8. Average acidity (proton release) constants of hydrides, hydroxides and oxohydroxides arranged according to degree of hydroxylation, oxolation and formal valence [8,26,28,47]. * corrected for CO_2 equilibrium

z = 1				z = 3			
FH	3,2			NO(OH)	3.3		
ClH	-7.0			ClO(OH)	2.0		
BrH	-8,5			IO(OH)	1.6		
IH	-9.5			z = 4			
z = 2				*$CO(OH)_2$	3.9	10.3	
OH_2	14			$GeO(OH)_2$	9.0	12.3	
SH_2	6,9	12.8		$AsO(OH)_2$	9.3		
SeH_2	3.9	10.9		$SO(OH)_2$	1.8	7.0	
TeH_2	2.6	11.0		$SeO(OH)_2$	2.6	8.3	
z = 3				$TeO(OH)_2$	2.7	8.4	
NH_3	30			$VO(OH)_2$			12.7
PH_3	27			z = 5			
z = 1				$PO(OH)_3$	2.1	7.1	12.0
Cl(OH)	7.3			$AsO(OH)_3$	2.2	6.9	11.4
Br(OH)	8.6			$ClO(OH)_3$	-7.0		
I(OH)	10.1			z = 7			
z = 2				$IO(OH)_5$	1,6	8.4	15.0
$Te(OH)_2$	2.4			z = 5			
z = 3				$NO_2(OH)$	-1.4		
$B(OH)_3$	9.2	14.0		$ClO_2(OH)$	-1.0		
$P(OH)_3$	1.9	6.7		$IO_2(OH)$	0.8		
$As(OH)_3$	9.2	12.1	13.4	z = 6			
$Sb(OH)_3$	11.0			$SO_2(OH)_2$	-3.0	1.7	
z = 4				$SeO_2(OH)_2$	-3.0	1.7	
$Si(OH)_4$	9.7	11.8	12.0	$TeO_2(OH)_2$	7.7	11.0	
$Ge(OH)_4$	8.9	12.7		$IO_2(OH)_2$	0.8		
z = 6				$CrO_2(OH)_2$	0.8	6.4	
$Te(OH)_6$	8.8			$Mo_2(OH)_2$		4.1	
				z = 7			
				$ClO_3(OH)$	-8.5		
				$IO_3(OH)$	1.6		

References

[1] Sanderson RT. Inorganic chemistry. New York, USA: Reinhold; 1967.
[2] Sanderson RT. Chemical bond energy. 2nd ed. New York, USA: Academic Press; 1976.
[3] Vijh AK. In: Diggle JW, editor. Oxides and oxide films. vol. 2. New York, USA: Marcel Dekker Inc; 1973. p. 1–94.
[4] Jensen WB. In: Mittal KL, Anderson Jr HR, editors. Acid-base interactions: zeist. The Netherlands: VSP; 1991. p. 3–23.
[5] Rosenholm JB, Peiponen K-E. Gornov E Adv Colloid Interface Sci 2008;141:48.
[6] Rosenholm JB. Adv Colloid Interface Sci 2017;247:264.
[7] Atkins P, De Paula J. Atkins physical chemistry. 7th ed. Oxford, UK: Oxford Univ. press; 2002.
[8] Lide DR, editor. CRC handbook of chemistry and physics. 87th ed. Boca Raton, Florida, USA: Taylor and Francis; 2006.
[9] Laidler KJ, Meiser JH. Phsical chemistry. 3rd ed. New York, USA: Houhton Miffin Co; 1999.
[10] Mortimer RG. Physical chemistry. Redwood City, California; USA: Benjamin Cummings Publ Co; 1993.
[11] Jolivet J-P. Metal oxide chemistry and synthesis. Chichester. UK: John Wiley & Sons; 2000.
[12] Rosenholm JB, Lindén M. In: Birdi KS, editor. Handbook of surface and colloid chemstry. 3rd ed. Boca Ration, Florida, USA: Taylor & Francis; 2008. p. 439–97.
[13] Lee L-H. In: Anderson Jr HR Mittal KL, editor. Acid-base interactions. Zeist. The Netherlands: VSP; 1991. p. 25–46.
[14] Mulliken RS. J Chem Rev 1935;3(573):586.
[15] Waddington TC, in Emeleus HJ. Sharpe AG., editors. Advances in inorganic chemistry and radiochemistry. vol. 1. New York, USA: Academic Press; 1959. p. 157–221.
[16] Ladd MPC, Lee WH. In: Reiss H, editor. Progressin solid-state chemistry. vol. 1. New York, USA: Macmillan Co; 1964. p. 37–82.
[17] Ruppel W, Rose A, Gerritsen HJ. Helv Phys Acta 1957;30:238.
[18] Kepp KP. J Phys Chem A 2019;122:7464.
[19] Duffy J. J Solid State Chem 1986;62:145.
[20] Dimitrov V, Sakka S. J Appl Phys 1996;79:1736.
[21] Israelachvili J. Intermolecular and surface forces. 2nd ed. San Diego, California, USA: Academic Press; 1994.
[22] Lyklema J. Fundamentals of surface and colloid sciencevol. IV. Amsterdam, The Netherlands: Elsevier; 2005.
[23] Rosenholm JB. Adv Colloid Interface Sci 2016;234:89.
[24] Rosenholm JB, Rahiala H, Puputti J, Stathopoulos V, Pomonis P, Beurroies I, et al. Colloids Surf A 2004;250:289.
[25] Baes Jr CF, Mesmer RE. The hydrolysis of cations. New York, USA: Wiley-Interscience; 1976.
[26] Ringbom A. Complexation in analytical chemistry. 2nd ed. New York, USA: Wiley-Interscience; 1963.
[27] James RO, Parks GA. In: Matijevic E, editor. Surface and colloid science. vol. 2. New York, USA: Plenum Press; 1982. p. 119–216.
[28] Rosenholm JB. Adv Colloid Interface Sci 2017;247:305.
[29] Granqvist B, Hedström G, Rosenholm JB. J Colloid Interface Sci 2009;333:49.
[30] De Bruyn PL, Agar GE. In: Furstenau W, editor. Froth flotation. New York, USA: Am Inst Mining Metallurgial Engineering; 1962. p. 91.
[31] Parks GA. Chem Rev 1965;65:177.
[32] Kosmulski M. Adv Colloid Interface Sci 2016;238:1.
[33] Lyklema J. Fundamentals of surface and colloid sciencevol. II. London, UK: Academic Press; 1995.
[34] Kosmulski M. Chemical properties of material surfaces. New York, USA: Marcel Dekker Inc; 2001.
[35] Yoon RH, Salman T, Donnay G. J Colloid Interface Sci 1979;70:483.
[36] Donnay JDH, Ondik HM. Crystal data determinative tables. 3rd ed. Bethesda, DC, USA: Natl Bureau Standards; 1972.
[37] Wyckoff RWG. Crystal structures. 2nd ed. New York, USA: Interscience; 1963.
[38] Marcus Y. J Cem Soc Faraday Trans 1991;87:2995.
[39] Fawcett WR. J Phys Chem B 1999;103:11181.
[40] Bockris JOM, Reddy AKM. Modern electrochemistryvol. 1. New York, USA: Plenum Press; 1970.
[41] Hunter RJ. Foundations of colloid science. 2nd ed. Oxford, UK: Oxford Univ Press; 2001.
[42] Hiemenz PC. Principles of colloid chemistry. 2nd ed. New York, USA: Marcel Dekker Inc; 1986.
[43] Dahlsten P, Próchniak P, Kosmulski M, Rosenholm JB. Colloids Surf A 2011;376:76.
[44] Rosenholm JB. Adv Colloid Interface Sci 2014;205:9.
[45] Pusey PN, Van Mengen W. Nature 1986;320:340.

[46] Grahame DC. Chem Rev 1947;41:441.
[47] Peltonen J, Järn M, Areva S, Lindén M, Rosenholm JB. Langmuir 2004;20:9428.
[48] Hägg G. Allmän och oorganisk kemi. Uppsala, Sweden: Almqvists & Wiksells; 1966.
[49] Wefers R, Misra C. Oxides and hydroxides of aluminum. ALCOA Laboratories: Aluminium Co America; 1987. ALCOATechnical Paper 19.
[50] Hem JD, Roberson CE. Chemistry of aluminium in water. Washington, DC, USA: USA DEP Interior; 1967.
[51] Pourbaix M, Franklin JA, Transl.. Atlas of electrochemical equilibria in aqueous solutions. Oxford, UK: Pergamon Press; 1963.
[52] Henry M, Jolivet J-P. Livage J J Struct Bond 1992;77:154.
[53] Livage J, Henry M, Ulrich DR Mackenzie JL, editors. Ultrastructure processing of advanced ceramics. New York, USA: John Wiley & Sons; 1988. p. 183–95.